NUMERICAL MODELING OF CHARRING ABLATIVE THERMAL PROTECTION SYSTEMS UNDER AERODYNAMIC HEATING

A THESIS SUBMITTED TO
THE GRADUATE SCHOOL OF NATURAL AND APPLIED SCIENCES
OF
MIDDLE EAST TECHNICAL UNIVERSITY

BY

VOLKAN COŞKUN

IN PARTIAL FULFILLMENT OF THE REQUIREMENTS
FOR
THE DEGREE OF DOCTOR OF PHILOSOPHY
IN
MECHANICAL ENGINEERING

FEBRUARY 2022

Approval of the thesis:

NUMERICAL MODELING OF CHARRING ABLATIVE THERMAL PROTECTION SYSTEMS UNDER AERODYNAMIC HEATING

submitted by **VOLKAN COŞKUN** in partial fulfillment of the requirements for the degree of **Doctor of Philosophy in Mechanical Engineering Department, Middle East Technical University** by,

Prof. Dr. Halil Kalıpçılar
Dean, Graduate School of **Natural and Applied Sciences** _____

Prof. Dr. M. A. Sahir Arıkan
Head of Department, **Mechanical Engineering** _____

Assoc. Prof. Dr. Cüneyt Sert
Supervisor, **Mechanical Engineering, METU** _____

Examining Committee Members:

Prof. Dr. Zafer Dursunkaya
Mechanical Engineering, METU _____

Assoc. Prof. Dr. Cüneyt Sert
Mechanical Engineering, METU _____

Prof. Dr. Abdullah Ulaş
Mechanical Engineering, METU _____

Assoc. Prof. Dr. Özgür Ekici
Mechanical Engineering, Hacettepe University _____

Assist. Prof. Dr. Sıtkı Uslu
Mechanical Engineering, TOBB ETU _____

Date: 11.02.2022

I hereby declare that all information in this document has been obtained and presented in accordance with academic rules and ethical conduct. I also declare that, as required by these rules and conduct, I have fully cited and referenced all material and results that are not original to this work.

Name, Surname: Volkan Coşkun

Signature :

ABSTRACT

NUMERICAL MODELING OF CHARRING ABLATIVE THERMAL PROTECTION SYSTEMS UNDER AERODYNAMIC HEATING

Coşkun, Volkan
Ph.D., Department of Mechanical Engineering
Supervisor: Assoc. Prof. Dr. Cüneyt Sert

February 2022, 157 pages

In this thesis study, comprehensive modeling of charring ablative materials subjected to aerodynamic heating is considered. The aim of this work is to develop a material response solver that allows predicting the response of charring ablative materials which are used as thermal protection systems in aerospace applications under different complexity levels. Detailed description of the governing equations and the novel method employed to solve them are given. The developed solver provides a versatile environment for engineering analyses and incorporates a third-party library for the evaluation of thermodynamic and transport properties of the pyrolysis gas mixture and chemical kinetics, if necessary. The two-equation model is used to model the thermal non-equilibrium between the solid and the gas phases, and the reactor network approach is adopted for modeling pyrolysis gas flow inside the porous ablative material. Usage of reactor network approach provides many advantages. Simulations with different gas compositions and reaction mechanisms can be carried out easily. In addition, it allows increasing the fidelity of the code such as future implementation of heterogeneous reactions to describe the pyrolysis decomposition. Correctness and the accuracy of the numerical implementation is ensured by conducting various veri-

fication and validation studies. Effects of chemical and thermal non-equilibrium and influence of pore structure parameters, i.e. porosity and permeability, on the response of charring ablative materials are explored.

Keywords: Charring Ablative Materials, Thermal Protection Systems, Thermal Non-equilibrium, Chemical Non-equilibrium, Porous Media

ÖZ

AERODİNAMİK ISINMA ALTINDA KÖMÜRLEŞEREK AŞINAN TERMAL KORUMA MALZEMELERİNİN SAYISAL OLARAK MODELLENMESİ

Coşkun, Volkan
Doktora, Makina Mühendisliği Bölümü
Tez Yöneticisi: Doç. Dr. Cüneyt Sert

Şubat 2022 , 157 sayfa

Bu tez kapsamında; aerodinamik ısınmaya maruz kalan kömürleşerek aşınan yalıtım malzemelerinin detaylı olarak modellenmesi ele alınmıştır. Kömürleşerek aşınan yalıtım malzemelerinin ısıl yük altındaki davranışını, farklı varsayımlar altında tahmin etmeye izin veren bir sayısal hesaplama aracı geliştirilmiştir. Geliştirilen hesaplama aracı, farklı detay seviyelerinde analizler yapılmasına izin vermektedir ve bir kimyasal kinetik hesaplama kütüphanesi ile birlikte çalışmaktadır. Kömürleşerek aşınma olgusu detaylı olarak anlatılmış ve temel korunum denklemleri verilmiştir. Gözenekli katı matris yapısı ve içerisindeki gaz bileşimi arasında oluşabilecek ısıl dengesizlik, çift sıcaklık yöntemi ile modellenmiştir. Reaktif gaz bileşiminin gözenekli katı matris içerisindeki haraketi reaktör ağ sistemi oluşturularak çözülmüştür. Bu yöntem sayesinde, farklı içeriklere sahip gaz bileşimleri farklı reaksiyon mekanzimaları ile kolayca modellenebilmektedir. Ayrıca, bu yöntem gelecekte yapılması muhtemel detay modelleme çalışmalarına da olanak vermektedir. Doğrulama çalışmaları ile geliştirilen hesaplama aracının güvenilirliği gösterilmiştir. Kimyasal ve termal dengesizlik varsayımlarının sonuçları üzerindeki etkileri incelenmiştir. Ek olarak, gözenekli yapı

parametrelerinin (gözeneklilik ve geçirimlilik) de sonuçlar üzerindeki etkileri incelenmiştir.

Anahtar Kelimeler: Kömürleşerek Aşınan Malzemeler, Termal Koruma Sistemleri, Termal Dengesizlik, Kimsayal Dengesizlik, Gözenekli Yapılar

to my nephew Ahmet Eren İstekli

ACKNOWLEDGMENTS

I would like to express my deepest gratitude to my supervisor Assoc. Prof. Dr. Cüneyt Sert for his guidance, advice, criticism, encouragements and insight throughout the research work.

I would also like to thank Prof. Dr. Zafer Dursunkaya and Assoc. Prof. Dr. Özgür Ekici for their exceptional technical insight, suggestions and constructive feedback.

TABLE OF CONTENTS

ABSTRACT v

ÖZ vii

ACKNOWLEDGMENTS x

TABLE OF CONTENTS xi

LIST OF TABLES xv

LIST OF FIGURES xviii

LIST OF ABBREVIATIONS xxiv

CHAPTERS

1 INTRODUCTION 1

1.1 Motivation 1

1.2 Ablative Materials 3

1.3 Literature Review 5

1.4 Scope of the Work and Outline 12

2 PHYSICAL DESCRIPTION OF THE THERMAL ABLATION PHENOMENA 15

2.1 Subsurface Phenomena 16

2.1.1 Material Decomposition 17

2.1.2 Subsurface Mass Balance 19

2.1.3 Subsurface Momentum Balance 20
2.1.4 Subsurface Energy Balance 22
2.1.5 Governing Equations in Integral Form 23
2.2 Surface Phenomena 24
2.2.1 Surface Mass Balance 25
2.2.2 Surface Energy Balance 27
3 NUMERICAL MODELING OF THERMAL ABLATION 31
3.1 Implementation of Governing Equations 31
3.1.1 Space Discretization 31
3.1.2 Grid Movement 33
3.1.3 Governing Equations in Moving Grid 35
3.1.4 Formulation of Governing Equations 36
3.1.4.1 Solid Continuity Equation 36
3.1.4.2 Gas Continuity Equation 38
3.1.4.3 Mixture Energy Equation 40
3.1.4.4 Boundary Conditions 41
3.1.4.5 Non-planar Geometries 43
3.1.5 Material Modeling 45
3.1.6 Solution Procedure 46
3.2 Verification Studies 47
3.2.1 Case 1: Transient Heat Conduction 48
3.2.2 Case 2: Transient Heat Conduction with Symmetry Boundary Conditions 52

3.2.3 Case 3: Steady-State Radiation . . . 53

3.2.4 Case 4: Transient Heat Conduction with Temperature Dependent Material Properties . . . 53

3.2.5 Case 5: Constant Surface Temperature with Prescribed Surface Recession . . . 57

3.2.6 Case 6: Material Decomposition . . . 60

3.2.7 Case 7: Material Decomposition with Thermo-chemical Erosion 63

4 THERMAL NON-EQUILIBRIUM AND CHEMICAL PHENOMENA . . . 67

4.1 Governing Equations . . . 68

4.1.1 Thermal Non-equilibrium . . . 68

4.1.1.1 Volumetric Heat Transfer Coefficient . . . 69

4.1.2 Chemical Phenomena . . . 71

4.1.2.1 Chemical Reactions and Chemical Time Scales . . . 71

4.1.2.2 Species Mass Conservation . . . 73

4.1.2.3 Thermodynamic and Transport Properties of Pyrolysis Gases . . . 75

4.2 Numerical Implementation . . . 78

4.3 Verification and Validation Studies . . . 82

4.3.1 Validity of Ideal Gas Approximation . . . 83

4.3.2 Steady-State Porous Flow . . . 85

4.3.3 Two-Equation Model . . . 87

4.3.4 Creation of $B^{'}$ Tables . . . 91

4.3.5 Comparison with Arc-Jet Test Data . . . 93

5 SIMULATION RESULTS . . . 97

5.1 Effects of Chemical Non-equilibrium under Local Thermal Equilibrium Assumption . . . 99

5.2 Thermal and Chemical Non-equilibrium . . . 105

5.3 Effects of Material Properties . . . 108

5.3.1 Porosity . . . 109

5.3.2 Permeability . . . 118

6 CONCLUSIONS AND FUTURE WORK . . . 125

6.1 Conclusions . . . 125

6.2 Future Work . . . 126

6.2.1 New Reaction Mechanism for Pyrolysis Gases . . . 126

6.2.2 Increasing Dimensionality . . . 127

6.2.3 Implementation of Species Diffusion . . . 127

6.2.4 Pyrolysis Gas Transport . . . 128

6.2.5 Surface Chemistry and Volume Ablation . . . 128

REFERENCES . . . 131

APPENDICES

A NEWTON'S METHOD . . . 143

B PROPERTIES OF TACOT MATERIAL . . . 145

C GRID INDEPENDENCY OF SOLUTION VARIABLES . . . 151

CURRICULUM VITAE . . . 155

LIST OF TABLES

TABLES

Table 1.1 List of simulation tools for ablative materials [9] 10

Table 2.1 Decomposition parameters for phenolic resins 18

Table 3.1 Properties of Ti-6Al-4V alloy at room temperature [68] 49

Table 3.2 Grid parameters for transient heat conduction problems 49

Table 3.3 Observed order of accuracy for transient heat conduction problems . 51

Table 3.4 Temperature dependent material properties 54

Table 3.5 Observed order of accuracy for transient heat conduction problems . 55

Table 3.6 Typical properties of PTFE [74] 58

Table 3.7 Grid parameters for moving surface problem 58

Table 3.8 L_∞ error norms for verification case 6 62

Table 3.9 L_∞ error norms for verification case 7 65

Table 4.1 Initial mole fractions of pyrolysis gases of TACOT material [77] . . 84

Table 4.2 Problem parameters for steady porous flow problem 88

Table 4.3 Properties of solid domain 89

Table 4.4 Properties of fluid domain 89

Table 4.5 L_∞ error norms for verification of two-equation model 91

Table 4.6 Parameters for the selected arc-jet test case 94

Table 4.7 Comparison of total surface recession 95

Table 5.1 Reaction mechanism for pyrolysis gases between $535\ K$ and $1925\ K$ [117] 98

Table 5.2 Enthalpy of reactions at $550\ K$ and $1600\ K$ 102

Table 5.3 Maximum temperature differences for Case 2 104

Table 5.4 Test matrix for porosity 109

Table 5.5 Test matrix for permeability 109

Table 5.6 Maximum temperature differences from the baseline solution for frozen flow 110

Table 5.7 Maximum temperature differences from the baseline solution in finite-rate chemistry model 115

Table 5.8 Maximum temperature differences from the baseline solution for frozen flow 119

Table 5.9 Maximum temperature differences from the baseline solution in finite-rate chemistry model 119

Table B.1 Decomposition parameters 145

Table B.2 Heats of formation and initial resin volume fraction 145

Table B.3 Pore structure parameters and emissivities 146

Table B.4 Thermo-physical properties of virgin 146

Table B.5 Thermo-physical properties of char 147

Table B.6 Properties of pyrolysis gases in chemical equilibrium at one atmosphere 148

Table B.7 Properties of frozen pyrolysis gases at one atmosphere ($MW = 17.89\ kg/kmol$) 149

Table C.1 Grid parameters 151

LIST OF FIGURES

FIGURES

Figure 1.1 Ablative materials as TPSs 2

Figure 1.2 Types of ablative materials 4

Figure 2.1 One-dimensional control volume for pyrolysis gas mass balance 20

Figure 2.2 Determination of filter (Darcy or superficial) velocity [46] 21

Figure 2.3 One-dimensional control volume for energy balance 22

Figure 2.4 Control volume for the derivation of interface conditions 26

Figure 2.5 Surface mass balance for a species 27

Figure 2.6 Surface energy balance 28

Figure 3.1 Variable arrangements in FVM [55] 32

Figure 3.2 Control volume for node j 32

Figure 3.3 Contracting grid scheme 34

Figure 3.4 Schematic of Landau transformation for one-dimensional planar geometries 34

Figure 3.5 Control volume for solution of gas phase continuity equation . . 39

Figure 3.6 Control volume for solution of mixture energy equation 40

Figure 3.7 Landau parameters for axisymmetric geometries 44

Figure 3.8 Solution procedure 47

Figure 3.9 Grid convergence of transient heat conduction solutions for $t = 5\ s$ and $t = 30\ s$ 50

Figure 3.10 Comparison of transient heat conduction solutions for $t = 5\ s$ and $t = 30\ s$ 51

Figure 3.11 Comparison of symmetric transient heat conduction solution for $t = 5\ s$ and $t = 30\ s$ 52

Figure 3.12 Grid convergence of transient heat conduction solution with temperature dependent material properties for $t = 5\ s$ and $t = 30\ s$ 55

Figure 3.13 Comparison of transient heat conduction solution with temperature dependent material properties for $t = 5\ s$ and $t = 30\ s$ 56

Figure 3.14 Convergence degradation due to inconsistent interpolation 57

Figure 3.15 Grid convergence of moving surface solution 59

Figure 3.16 Comparison of moving surface solution with analytical result . . 59

Figure 3.17 Schematic description of verification case 6 61

Figure 3.18 Comparison of temperatures at pre-determined locations for verification case 6 61

Figure 3.19 Comparison of pyrolysis gas blowing rate and char/pyrolysis fronts for verification case 6 62

Figure 3.20 Abrupt change in pyrolysis gas blowing rate in verification case 6 62

Figure 3.21 Schematic description of verification case 7 63

Figure 3.22 Comparison of temperatures at pre-determined locations for verification case 7 64

Figure 3.23 Comparison of pyrolysis gas blowing rate and char/pyrolysis fronts for verification case 7 64

Figure 3.24 Abrupt change in pyrolysis gas blowing rate in verification case 7 65

Figure 4.1 Detailed and unit cell representation of open cell foams [100, 101] 71

Figure 4.2 Time scales in a chemically reacting flow [102] 72

Figure 4.3 Reactor network representation of a 1D domain 79

Figure 4.4 Solution procedure 82

Figure 4.5 Time progress of the solution 82

Figure 4.6 Reduced property variation of pyrolysis gas mixture 85

Figure 4.7 Reduced property variation of individual species 86

Figure 4.8 Generalized compressibility chart [103] 87

Figure 4.9 Comparison result for steady porous flow verification study . . . 88

Figure 4.10 Boundary conditions for two-equation model verification study . 89

Figure 4.11 Comparison results for solid temperatures 90

Figure 4.12 Comparison results for fluid temperatures 90

Figure 4.13 Comparison results for temperature differences between the phases 90

Figure 4.14 Comparison results for wall enthalpy, h_w 92

Figure 4.15 Comparison results for non-dimensional char mass flux, B'_{ch} . . 93

Figure 4.16 Comparison of temperatures on the surface and at three depths . 95

Figure 5.1 Temperature solutions obtained using equilibrium (EQ), frozen and finite-rate (FR) chemistry models for Case 1 100

Figure 5.2 Variation of internal energies of the pyrolysis gas mixture for frozen and chemical equilibrium conditions 100

Figure 5.3 Equilibrium mole fraction variations of pyrolysis gas species as a function of temperature 101

Figure 5.4 Pyrolysis and char fronts for Case 1 103

Figure 5.5 Temperature solutions obtained using equilibrium (EQ), frozen and finite-rate (FR) chemistry models for Case 2 103

Figure 5.6 Pyrolysis and char fronts for Case 2 104

Figure 5.7 Species injected to the boundary layer 105

Figure 5.8 Temperature differences between the pyrolysis gas mixture and solid phase at different depths for Case 1 106

Figure 5.9 Temperature differences between the pyrolysis gas mixtures at different depths for Case 1 107

Figure 5.10 Temperature differences between the pyrolysis gas mixture and solid phase at different depths for Case 2 108

Figure 5.11 Temperature differences between the pyrolysis gas mixtures at different depths for Case 2 108

Figure 5.12 Effects of porosity on solid and frozen pyrolysis gas mixture temperatures 111

Figure 5.13 Temperature differences between the frozen pyrolysis gas mixture and solid phase at different depths for varying porosity values . . . 112

Figure 5.14 Volumetric heat transfer coefficient between the frozen pyrolysis gas mixture and solid at different depths for varying porosity values . . 112

Figure 5.15 Effects of porosity on blowing rates and pyrolysis and char fronts for frozen flow 113

Figure 5.16 Effects of porosity on solid and reacting pyrolysis gas mixture temperatures 114

Figure 5.17 Effects of porosity on temperature differences between the solid and reacting pyrolysis gas mixture 115

Figure 5.18 Volumetric heat transfer coefficient between the pyrolysis gas mixture and solid at different depths for varying porosity values in finite-rate solutions 116

Figure 5.19 Effects of porosity on blowing rates and pyrolysis and char fronts in finite-rate chemistry model 116

Figure 5.20 Temperature differences between the solids at different depths . . 117

Figure 5.21 Temperature differences between the pyrolysis gas mixtures at different depths 117

Figure 5.22 Effects of porosity on major species injected to the boundary layer 118

Figure 5.23 Temperature differences between the frozen pyrolysis gas mixture and solid phase at different depths for varying permeability values . 120

Figure 5.24 Temperature differences between the reacting pyrolysis gas mixture and solid phase at different depths for varying permeability values . 121

Figure 5.25 Volumetric heat transfer coefficient between the frozen pyrolysis gas mixture and solid at different depths for varying permeability values 121

Figure 5.26 Volumetric heat transfer coefficient between the reacting pyrolysis gas mixture and solid at different depths for varying permeability values 122

Figure 5.27 Temperature differences between the solids at different depths . . 123

Figure 5.28 Temperature differences between the pyrolysis gas mixtures at different depths 123

Figure 5.29 Effects of permeability on major species injected to the boundary layer 124

Figure C.1 Effects of cell size on solid and pyrolysis gas mixture temperatures 152

Figure C.2 Effects of cell size on temperature differences between the pyrolysis gas mixture and solid material 153

Figure C.3 Effects of cell size on volumetric heat transfer coefficient 153

Figure C.4 Effects of cell size on evolution of pyrolysis and char fronts and pyrolysis gas blowing rates 154

Figure C.5 Effects of cell size on abrupt change in pyrolysis gas blowing rates 154

LIST OF ABBREVIATIONS

Acronyms

0D	Zero-dimensional
1D	One-dimensional
2D	Two-dimensional
3D	Three-dimensional
CHAR	CHarring Ablator Response
CMA	Charring Material thermal response and Ablation program
FIAT	Fully Implicit Ablation and Thermal response program
FVM	Finite Volume Method
NASA	National Aeronautics and Space Administration
NIST	National Institute of Standards and Technology
PATO	Porous-material Analysis Toolbox based on OpenFOAM
PICA	Phenolic-Impregnated Carbon Ablator
PTFE	PolyTetraFluoreEthylene (Teflon)
TACOT	Theoretical Ablative Composite for Open Testing
TGA	Thermo Gravimetric Analysis
TITAN	Two-dimensional Implicit Thermal response and AblatioN
TPSs	Thermal Protection Systems

Latin Symbols

A, B, C, ...	Chemical species involved in a reaction
B	Non-dimensional blowing rate
Bi	Biot number
c_p	Specific heat at constant pressure, $J/(kg \cdot K)$
c_v	Specific heat at constant volume, $J/(kg \cdot K)$

C_h	Stanton number for heat transfer
C_m	Stanton number for mass transfer
d_f	Equivalent fiber (strut) diameter, m
d_m	Mean pore diameter, m
D	Diffusion coefficient, m^2/s
Da	Damköhler number
e	Internal energy, J/kg
E_a	Activation energy, $kcal/mol$
Fo	Fourier number
g	Free enthalpy of Gibbs, J/kg
h	Absolute enthalpy, J/kg
h^o	Heat of formation, J/kg
h^s	Sensible enthalpy, J/kg
Δh_R	Enthalpy (heat) of reaction, J/kg
h_V	Volumetric heat transfer coefficient, $W/(m^3 \cdot K)$
k	Thermal conductivity, $W/(m \cdot K)$, or reaction rate coefficient
K_v	Valve coefficient, $m \cdot s$
L	Thickness, m
L_o	Initial thickness, m
L_2	Error norm
L_∞	Infinite error norm
m	Mass, kg
$\dot{m}$	Mass flow rate, kg/s
MW	Molecular weight, $kg/kmol$
$\mathbf{n}$	Outward normal of a surface
N_R	Number of reactions
N_S	Number of species

Nu_V	Volumetric Nusselt number
p	Pressure, Pa
Pr	Prandtl number
$\dot{q}$	Heat transfer rate, W
r	Radius, m, or grid refinement factor or reaction rate, $kmol/(m^3 \cdot s)$
r_c	Recovery factor
R_o	Initial outer radius, m
R_u	Universal gas constant, $J/(kmol \cdot K)$
s	Surface recession, m, or entropy, $J/(kg \cdot K)$
$\dot{s}$	Surface recession rate, m/s
S	Surface area, m^2
t	Time, s
T	Temperature, K
u	Velocity, m/s
U_k	Diffusion velocity, m/s
x	Distance from the current surface position, m
X	Species mole fraction or a generic material property
v	Stoichiometric coefficient
V	Volume, m^3
y	Mass fraction of solid phases
Y	Species mass fraction
z	Distance from the initial surface position, m
Z	Pre-exponential factor, s^{-1}, or compressibility factor

Greek Symbols

α	Thermal diffusivity, m^2/s
β_k	Temperature slope, $1/K$

Γ	Resin volume fraction
ϵ	Porosity
η	Landau coordinate
θ	Transformed temperature, K
ι	Extent-of-reaction
κ	Permeability, m^2
λ	Flow parameter or characteristic value
μ	Dynamic viscosity, $Pa \cdot s$
ν	Kinematic viscosity, m^2/s
ξ	Dimensionless relative density
ρ	Density, kg/m^3
σ	Stefan-Boltzmann constant, $5.670\,51 \times 10^{-8}\ W/(m^2 \cdot K^4)$
τ	Characteristic time, s
Φ	Dimensionless factor used in Wilke formula
ψ	Order-of-reaction
$\dot{\omega}$	Mass production rate due to homogeneous reactions, kg/s
ε	Emissivity
ϑ	Temperature exponent
ς	Observed order of accuracy

Subscripts

0	Initial
∞	Ambient
A, B, C	Components of composite ablative
c	Critical point values
ch	Char
$cond$	Conduction
cs	Control surface

cw	Cold wall
D	Darcian
e	Edge of boundary layer
eff	Effective
f	Fluid
gen	Generated
i, j	Indices
k	Grid level
pg	Pyrolysis gases
r	Recovery value or reduced properties
ref	Reference
s	Solid
ss	Steady-state
st	Stored
$stag$	Stagnation
tch	Thermo-chemical
w	Wall
v	Virgin

Superscripts

0	Standard state of one atmosphere
$'$	Reactant side of a reaction or a modified parameter
$''$	Per unit area, m^{-2}, or product side of a reaction
$'''$	Per unit volume, m^{-3}
f	Forward
n	Current time step
r	Reverse
v	Current iteration level

CHAPTER 1

INTRODUCTION

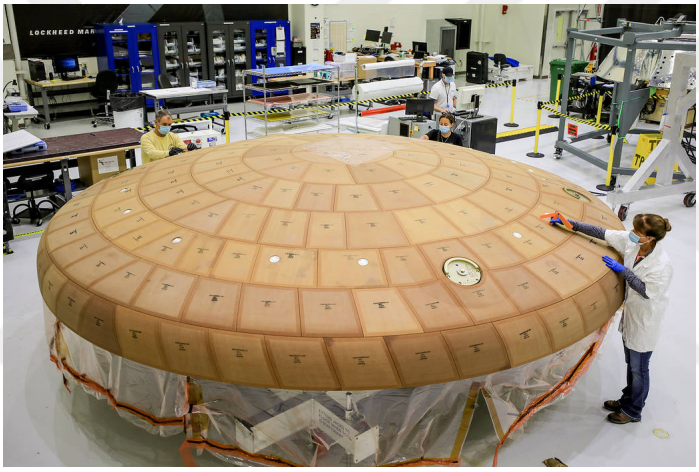
1.1 Motivation

Ablative materials have a crucial place in the entire aerospace and defense industries as thermal protection systems (TPSs) material. These sacrificial materials are used to produce the heat shield which maintains the thermal protection of components susceptible to high temperature - such as forebody structure and aerodynamic surfaces of spacecrafts and warheads of missiles - from severe aerodynamic heating encountered during high-speed flight. Ablative materials are also widely used to provide insulation to propulsion devices such as solid rocket motors. An ablative liner is implemented between the rocket motor case and the solid fuel grain. Graphite is generally placed at the throat of a nozzle due to its high temperature strength. Other ablatives, such as carbon-phenolic, are also utilized to protect the wall of the nozzle. Typical usage of ablative materials is illustrated in Figure 1.1.

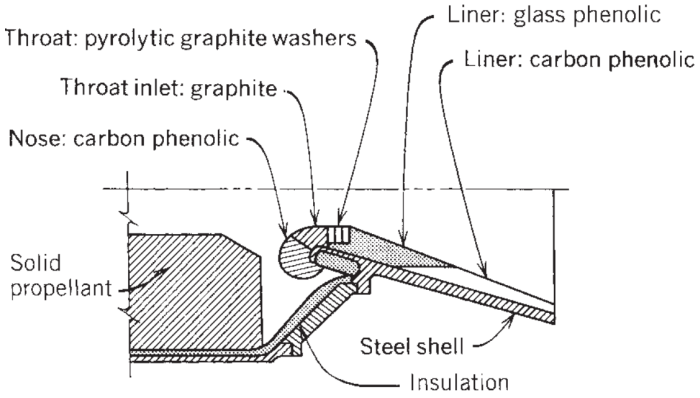
TPSs generally represent an elevated mass for the spacecrafts or missiles. So, it is always desirable to keep the mass of TPSs at a minimum if it is not avoidable to employ them in order to ensure the safety of the flight. Improvements in the physical and numerical models, increased knowledge about the behavior of the TPSs, and decreased uncertainty margins could all contribute to a significant reduction in the mass fraction of the TPSs. As far as ablative materials are concerned, the ability to accurately predict the internal response of the material along with the ablation rate and corresponding shape change is of primary importance in the design and sizing of the heat shields.

Ablative response of a material cannot be reduced to solely a material property. In-

stead, it is a consequence of material-medium interaction, aero-thermochemistry of the environment and geometry of the body. Since it is a very complex, specialized and multidisciplinary topic, general purpose free or commercial solvers are not capable of modeling the ablation phenomena. Thus, those who work on ablation problems such as government sponsored agencies or private companies have been developing their in-house codes to estimate the behavior of the ablative materials. The codes are in general kept secret and subject to export control, only some depreciated versions are publicly available. In addition, most of them include certain assumptions and are optimized for the ablative material under consideration. Therefore, a reliable and flexible numerical tool is a vital need for the handling of the various coupled ablation



(a) Ablative heat shield of Orion spacecraft [1]



(b) Typical rocket nozzle design [2]

Figure 1.1: Ablative materials as TPSs

problems during the design and analysis of ablative TPSs and carrying out material trade studies.

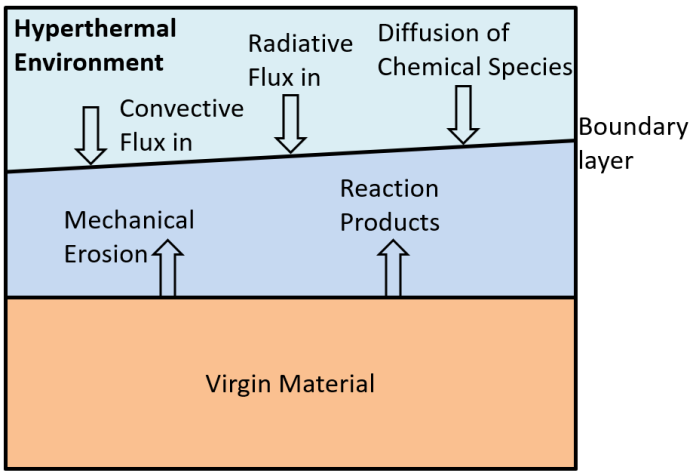
1.2 Ablative Materials

Application of ablative materials as TPSs is based on the thermal degradation of a sacrificial solid material absorbing heat and thus thermally protecting the structure underneath. Sublimation of a material can be considered as the simplest ablation mechanism. More complex mechanisms incorporate thermal destruction of the solid material where a heat-absorbing material decomposition, i.e. *pyrolysis*, occurs below the surface. The main advantage of an ablative material is its superiority in terms of absorbing considerable amounts of heat while being self-restraint and requiring no active components. The major drawback is that surface geometry may notably change due to heterogeneous chemical reactions, phase change and mechanically erosion, i.e. *spallation*, by shear forces [3]. In addition, ablative TPSs are conventionally not reusable.

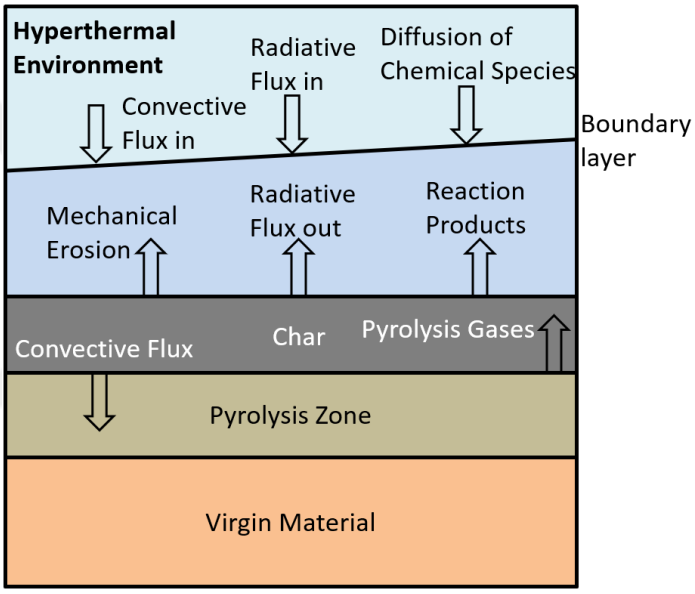
Ablative TPSs may be classified on the basis of thermal destruction mechanism into three main categories [4]:

- Chemically homogeneous materials which lose mass at the surface due to heterogeneous chemical reactions and/or sublimation (e.g. graphite and teflon)
- Reinforced composite materials which thermally break down in-depth and release high-temperature gas mixture (e.g. carbon-phenolic and silica-phenolic)
- Inorganic glassy materials consumed due to vaporization, heterogeneous chemical reactions, and mechanical removal (e.g. quartz and silica)

The first two classes are frequently employed in spacecraft and missiles and are referred as *non-charring* ablatives, and *charring* ablatives, respectively. The latter is used only in specific applications where optical and dielectric properties are needed at high temperatures [5]. Fundamental physico-chemical interactions for non-charring and charring ablatives are illustrated in Figure 1.2.



(a) Non-charring



(b) Charring

Figure 1.2: Types of ablative materials

Non-charring ablatives lose mass only on the exposed surface by surface ablation and/or spallation. Surface ablation may result from sublimation and/or heterogeneous chemical reactions. The evolving gases intrude into the boundary layer and decrease the incoming convective heat flux at the surface by thickening the boundary layer and altering the velocity profile [6]. The most well-known non-charring ablative is polytetrafluoroethylene (PTFE), i.e. teflon, which totally sublimes between 750 K and 780 K and leaves no solid residue. Other prominent non-charring ablatives are

carbon-carbon (C-C) and graphite. Oxidation that starts around 1600 K and sublimation at temperatures as high as 4000 K are the main mass removal processes at the exposed surface of graphite [7]. In contrast to non-charring ablatives, charring ablatives are made up of filler matrix, such as phenolic resins, and reinforcing materials, such as silica and carbon. The resin matrix starts to decompose and release gaseous species as the temperature increases. The pyrolysis process is in general endothermic and leaves a porous carbonaceous residue known as *char*. The part of the material which does not undergo any degradation and keeps its original composition is denoted as *virgin*. The char layer contributes to thermal protection by providing further insulation owing to its much lower thermal conductivity compared to the virgin part and high-temperature outer surface for re-radiation. The char may lose mass due to heterogeneous chemical reactions, phase change and spallation. As the pyrolysis gas mixture passes through the porous material by diffusion and advection into the boundary layer, homogeneous chemical reactions may take place in the mixture. Furthermore, pyrolysis gases may react with the char layer and boundary layer gases.

In general, non-charring ablatives resist higher shear stresses than charring ablatives, and they are heavier. Therefore, if their use is necessary, they are applied to the regions that are exposed to the highest structural loads and where a uniform and clean removal of the ablative material is required [8], such as rocket nozzle throat. Charring ablatives are typically applied to regions that are not subject to high shear stresses such as rocket nozzle linings. Charring materials are most commonly used in atmospheric entry applications.

1.3 Literature Review

There is an extensive literature on the modeling of ablative materials dating back to 1960s. Due to immense amount of studies, here it is not intended to examine all the published work on modeling of ablation. Instead, prominent related studies and review of the existing ablation solvers are presented. The general history of ablative materials and modeling approaches have been reviewed in [9–12].

Pioneering study on modeling of ablative materials may be attributed to the work of

Moyer and Rindal [13] during the 1960s. Moyer and Rindal published a comprehensive report about the response of charring ablatives in high temperature flow and developed a one-dimensional material response code called CMA (Charring Material Ablation). CMA is based on several major simplifying assumptions: 1) pyrolysis gas mixture is in thermal and chemical equilibrium with the char and passes immediately out of the material through the char, 2) ablation only occurs at the surface, 3) ablating surface is in chemical equilibrium with the boundary layer gases. In short, it only models the transient heat conduction and pyrolysis of the solid and does not consider the pyrolysis gas flow inside the material. However, it gives reasonably accurate results proved in experiments with minimal computational expenses and has been used as the industry standard code for decades. CMA uses a finite-difference spatial discretization scheme for the conservation equations and first-order implicit time integrator. In order to account for the moving boundary, i.e. the receding surface, a translating grid scheme in which each node translates with the same velocity as the receding surface node except the opposite boundary node was implemented. The opposite boundary node is removed from the solution domain when a critical thickness has been reached.

A very noteworthy study is that of April's dissertation work [14] published in 1969. The non-equilibrium flow of pyrolysis gas species through the char layer of an ablative material was first modeled in this study by employing reaction kinetics. Under local thermal equilibrium assumption between the solid and pyrolysis gases, April described the transport phenomena as steady one-dimensional. In addition to reacting non-equilibrium flow, frozen and equilibrium flow of gas mixture was modeled in order to identify the gas composition inside the material and injected in to the boundary layer. The corresponding effects of chemical model on the energy equation was studied, and it was suggested that frozen and equilibrium solutions bracketed the non-equilibrium solution. A reaction mechanism based on experimental data was developed for the non-equilibrium pyrolysis gas flow. This mechanism is still the only one used by the ablation community.

Another notable contribution to the modeling of ablation was made by Clark [15, 16]. His experimental work [15], in which mixtures of methane and helium were passed through the resistant heated porous carbon slabs, proposed that there exist temperature

differences (i.e. thermal non-equilibrium) between the gases and the char and gas temperatures lag the solid temperatures near the entrance surface. Later on, Clark [16] formulated the governing equations for the estimation of the transient response of charring ablative materials considering the general case of thermal non-equilibrium and kinetically controlled chemical reactions and mass transfer between the char layer and pyrolysis gases. In this work, the pyrolysis zone was assumed to be infinitely thin. This assumption leads to modeling the ablative material as consisting of two constant density sections: char and virgin. Thus, it lacks the ability to estimate the solid density profile through the pyrolysis process.

Blackwell and Hogan [17] introduced a finite control volume procedure with a fully implicit time integrator for one-dimensional non-charring ablatives, in which the effect of moving boundary was addressed using the Landau transformation [18]. In this scheme, while the computational domain is shrinking due to surface recession, the relative size and total number of elements remain fixed in the transformed domain, and each node moves at a fraction of the surface recession rate. The advantage of removing the node-dropping scheme comes with the cost of change in the energy content of elements due to element volume reduction.

Amar [19, 20] went a step further and successfully implemented the Landau transformation scheme to charring ablative materials. Pyrolysis gas flow inside the porous ablative material was modeled using Darcy's law under local thermal equilibrium assumption. In addition, pyrolysis gases were assumed to be in chemical equilibrium. First-order implicit time integration with second-order spatial discretization scheme was employed. Fully coupled governing equations were then solved using the block Gauss-Seidel method with Newton sub-iteration for the energy and gas phase continuity equations.

Joshi [21] extended the work of Amar by considering the chemical interactions, i.e. chemical non-equilibrium, between the ablating surface and boundary layer gases through coupling his one-dimensional material response code with the reactive flow solver EILMER3 developed at the University of Queensland. The fluid-structure coupling eliminates the need of pre-compiled surface thermo-chemical data required to calculate the surface recession rate as a function of surface temperature and injection

rate of pyrolysis gases.

Since the work of Clark, there have been no eminent studies that consider the homogeneous chemical reactions inside the ablative materials until 2000s. Ayasoufi et al. [22] developed a material response solver that takes into account the homogeneous chemical reactions in the flow of pyrolysis gases and thermal non-equilibrium between the char and pyrolysis gases. The translating grid scheme of CMA was adopted to handle surface recession. The solid and gas phase conservation equations were treated explicit with respect to temperature with upwind differencing method. The developed solver was verified using available analytical and numerical results available in the literature. However, effects of thermal and chemical non-equilibrium on the response of charring ablative materials have not been presented and discussed in the paper.

Scoggins [23] developed a one-dimensional material response solver that considers both thermal and chemical non-equilibrium inside the char layer for carbon-phenolic. Similar to [14] and [16], the ablative material was assumed to consist of two constant density regions and so the pyrolysis zone was regarded to be infinitely thin. The code requires the composition of the gas mixture produced at the pyrolysis interface as input in order to solve the species conservation equations inside the char layer. A reaction mechanism was developed through the kinetic rate data from the National Institute of Standards and Technology (NIST) Chemical Kinetics Database [24] to model the evolution of chemical species in the pyrolysis gas mixture. Scoggins compared the char layer temperature and gas-solid temperature difference at a specified time for the same run conditions obtained for frozen pyrolysis gases and one using 19 species mechanism. The results indicated that the reactions are notably endothermic and act to reduce the pyrolysis gas temperature. Furthermore, Scoggins conducted a parametric study by changing the volumetric heat transfer coefficient between the solid char and frozen pyrolysis gas mixture orders of magnitude. As expected, higher values for volumetric heat transfer coefficient yielded lower temperature differences between the phases.

Chen and Milos [25] presented the results of parametric studies for the phenolic-impregnated carbon ablator (PICA) considering finite-rate homogeneous reactions taking place in the pyrolysis gases. Reaching mechanism given in [14] was used and

local thermal equilibrium between the phases was assumed. The pyrolysis process was assumed to be under chemical equilibrium. Thus, mass fractions of chemical species formed during decomposition were pre-determined at the beginning of the analysis. The boundary conditions used for the parametric studies were associated with the Orion Lunar return mission. Simulation results indicated that the presence of chemical non-equilibrium in the pyrolysis gas flow does not meaningfully alter the in-depth thermal response estimated using the chemical equilibrium model.

Lachaud et al. [26] compared the thermal response of a low-density carbon-phenolic composite under two different chemistry models: equilibrium chemistry and finite-rate chemistry. An increase in the predicted temperatures was observed when chemical non-equilibrium was assumed, i.e. equilibrium chemistry assumption yielded lower temperatures.

Most recently, Li et al. [27] carried out parametric studies by varying the volumetric heat transfer coefficient between the porous solid and pyrolysis gas mixture in order to analyze the influences of local thermal non-equilibrium on the thermal response of charring ablative thermal protection materials. The pyrolysis gas mixture was considered to be frozen. The simulation results suggested that the volumetric heat transfer coefficient is correlated positively to the degree of decomposition and pressure inside the material, and correlated negatively to the solid-gas temperature difference.

Lachaud et al. [11] provided a list of ablative material simulation tools developed by government sponsored agencies and private companies for the simulation and optimization of charring and non-charring ablative TPSs in practical applications. The list has been updated by Natali et al. [9] and shown in Table 1.1. FIAT (Fully Implicit Ablation and Thermal response) and PATO (Porous-material Analysis Toolbox based on OpenFOAM) codes can be obtained freely among the simulation tools by qualified individuals/organizations under a Non-Disclosure and Software Usage Agreement with NASA Ames Research Center. AMARLLIS is an integral part of Siemens LMS Thermal Analysis Software and commercially available. Distribution of other simulation tools is highly restricted.

FIAT code has been developed by Milos and Chen [28] at NASA Ames Research Center. The theory behind the CMA and FIAT is the same, but FIAT uses a fully

Table 1.1: List of simulation tools for ablative materials [9]

Name	Contact	Owner/Country	Users	Application
Amaryllis	T. van Eekelen	Samtech, Belguim	EADS Astrium, ESA	Design
CAMAC	W.S. Lin	CSIST, Taiwan	Taiwan Ins. of Sci. Tech.	Unknown
CAT	N.N. Mansour	NASA ARC, USA	NASA ARC	Analysis
CHALEU	B. Blackwell	SNL, USA	SNL	Design
CHAP	P. Keller	Boeing, USA	Boeing	Design
CMA	R. Beck	Aerotherm, USA	NASA, SNL	Design
CMA/SCMA	C. Park	Tokyo Univ., Japan	JAXA	Design
CMA/KCMA	P. Reygnier	ISA, France	ISA/ESA	Analysis
COYOTTE2	W. Kuntz	SNL, USA	SNL	Design
FABL	J. Merrifield	Fluid Gray. Eng. Ltd., UK	ISA/ESA/FG E	Analysis
FIAT	Y.K. Chen	NASA ARC, USA	NASA, SpaceX	Design
FIAT3D	Y.K. Chen	NASA ARC, USA	NASA ARC	Analysis
HERO	M.E. Ewing	ATK, USA	ATK	Analysis
ITARC	M.E. Ewing	ATK, USA	ATK	Design
libAblation	R.R. Upadhyay	Univ. Of Tex. Aust., USA	UTA	Analysis
MIG	S. Roy	Univ. Of. Flo., USA	Univ. of Florida	Analysis
MOPAR	Martin	Univ. Of Mich., USA	Univ. Of Michigan	Analysis
NEQAP	J.B. Scoggins	N. Carol. St. Univ., USA	NCSU	Analysis
NIDA	G.C. Cheng	Univ. Alab. Birm., USA	UAB	Analysis
PATO	J. Lachaud	NASA ARC, USA	Univ. Calif. Santa Cruz	Analysis
PRESENT	J. Dec	NASA LaRC, USA	NASA LaRC	Analysis
STAB	Remark	NASA JSC, USA	Fluid Gr. Eng.	Design
TITAN	F.S. Milos	NASA ARC, USA	NASA	Analysis
CHAR	n.a.	NASA JSC, USA	NASA	n.a.
TMU	A.R. Bahramian	T. Modares Univ., Iran	TMU	Analysis
US3D	G. Candler	Univ. Of Minn., USA	UM	Analysis
SCMA	n.a.	JAXA/Nagoya University, Japan	JAXA	n.a.
SCMA2	n.a.	JAXA/Nagoya University, Japan	JAXA	n.a.

n.a. – not available.

implicit finite difference formulation which improves numerical stability and convergence compared to CMA. Currently, FIAT can be regarded as the industry standard code and is mainly used for the simulation of one-dimensional multi-layer stack of ablative materials and for parametric studies due to its computational effectiveness. Two-dimensional (TITAN, Two-dimensional Implicit Thermal response and AblatioN) and three-dimensional versions of the FIAT code (FIAT-3D) have also been developed by Chen and Milos [29]. These codes are based on the same governing equations used by the FIAT. However, they enhance the simulation capability by allowing modeling of orthotropic material properties and the analysis of the curved regions with additional computational cost.

Amar et al. [30] developed a three-dimensional material response code named CHAR (CHarring Ablator Response) for charring ablatives at NASA Johnson Space Center. The code utilizes several third-party libraries such as *libMesh*, *Cantera* and *Eigen* that perform meshing, chemistry related calculations, data management and matrix calculations. Indeed, CHAR, itself, can be thought of as an ablation physics wrapper around other libraries. The CHAR relies on various assumptions that include: 1) pyrolysis gases do not react with the solid material, 2) gas diffusion is not considered, 3) local thermal equilibrium is assumed, 4) pyrolysis gas mixture is in chemical equi-

librium, 5) pyrolysis gas velocity inside the material is not high such that Darcy's law represents momentum equations sufficiently. The code is mainly used for engineering design purposes.

Lachaud and Mansour [31] have been developing a modular ablation toolbox PATO as a portable library of OpenFOAM, an open source CFD software. PATO distinguishes itself from the other simulation tools as it allows modeling the ablation phenomena at microscopic level, e.g. modeling fiber reactivity, in addition to the conventional macroscopic level. Developers expect that modeling at microscopic level can help perceive the relevant physical and chemical phenomena behind ablation clearly and develop more appropriate macroscopic models. PATO is also capable of modeling homogeneous and heterogeneous chemical reactions inside the ablative material under local thermal equilibrium assumption. It uses *MUTATION++*, a chemical library developed at the von Karman Institute, to compute all chemistry related data and thermodynamic and transport properties pyrolysis gases.

Aykan and Dursunkaya [32, 33] studied the numerical analysis of ablation process on 2D external surfaces and developed a numerical tool for the estimation of thermal response of charring ablative materials. Heat transfer through the virgin material, the char and the gas was solved and the endothermic decomposition of the solid was taken into account. Local thermal equilibrium between the pyrolysis gases and solid material was assumed and chemical reactions among the pyrolysis gases were not considered. In addition, pressure in the solution domain was assumed to be constant, i.e. density of the pyrolysis gases is only a function of temperature. Boundary conditions were independent of the ablation process, i.e. there exists no coupled solution algorithm that relates the heat flow and the ablative material.

Şimşek and Uslu [34, 35] developed a 1D material response solver that also estimates the aerodynamic heating rate using pre-determined flight trajectory. The solver takes into account the heat transfer through conduction and thermal decomposition of the solid virgin material. However, similar to CMA and FIAT codes, the gas flow inside the ablative material was not considered, i.e. generated gases were immediately injected into the boundary layer. Instead of thermo-chemical ablation, surface recession was calculated using simplified heat of ablation model.

Alanyalıoğlu [36] developed two numerical tools with different degrees of fidelity in order to estimate the response of charring ablative materials in rocket nozzle applications. The first one is a 1D material response solver which takes into account thermal decomposition and gas flow inside ablative materials. It was assumed that materials lose mass only by melting mechanism and surface recedes at a constant known temperature. This assumption leads to explicit treatment of the surface energy balance equation and significantly reduces computational time. However, it restricts usability of the solver substantially as most of the ablative materials lose mass by chemical reactions and surface temperature does not remain constant during recession. The second tool is 2D FLUENT implementation of the first tool which allows performing conjugate analyses of ablative materials through gas-surface interactions.

1.4 Scope of the Work and Outline

Although substantial research has been performed on the modeling of ablative materials over the past sixty years, there is no general agreement about the effects of thermal and chemical non-equilibrium on the thermal response of charring ablative materials. While some studies indicate that thermal and chemical non-equilibrium shall be considered for better estimates, others claim that their effects are unsubstantial in practice. Previous studies mostly assume the pyrolysis zone as infinitely thin and examine the interactions only inside the char layer or focus only on the chemical non-equilibrium under local thermal equilibrium assumption. Simulations that consider thermal non-equilibrium between the phases have been performed using predetermined volumetric heat transfer coefficients, and effects of increasing the volumetric heat transfer coefficient were reported. Simultaneous effects of thermal and chemical non-equilibrium on thermal behavior of charring ablative materials have not been thoroughly investigated. Additionally, research codes with chemical non-equilibrium capability are mostly designed for a single reaction mechanism, and hence analysis of different reaction mechanisms with various species is not feasible.

In order to estimate the surface recession rate and density and temperature variations through the thickness of the ablative TPSs accurately, a high-fidelity simulation tool that represents the real physics and chemistry of the ablation process is required.

However, as the fidelity of the model increases, computational cost increases exponentially and convergence issues may create prohibitive difficulties. Therefore, a compromise between model fidelity and computational cost is unavoidable.

The major objective of this work is to develop a versatile numerical framework that enables modeling of charring ablative TPSs subjected to hyper-thermal environment under different complexity levels, i.e. under thermal and/or chemical (non-)equilibrium assumptions. In other words, while material selection trade studies are being carried out, the framework allows using fast, low-fidelity but adequately accurate models. However, when more accurate results are desired, the framework will allow using high-fidelity models, e.g. finite-rate homogeneous reactions. The thesis, furthermore, seeks to investigate the influences of thermal and/or chemical (non-)equilibrium on the response of charring ablative materials. To achieve this purpose, several simulations under different assumptions with varying material properties have been performed. Modeling and investigation of the following ablation processes are not in the scope of this work: 1) non-linear relationship between the porous flow resistance and pyrolysis gas velocity, i.e. non-Darcian behavior, 2) heterogeneous chemical reactions between the pyrolysis gases and solid material, i.e. *coking*, 3) species mass diffusion, and 4) heterogeneous chemical reactions between the boundary layer gases and ablation surface.

Extensive previous studies and vastness of the research area keep the contribution of this work being limited to a small aspect of ablation modeling. However, the contribution of this work can be listed as:

- Development of a versatile numerical framework that enables simulation of thermal behavior of ablative materials under different fidelity levels.
- Exploration of thermal and chemical non-equilibrium phenomena.
- Investigation of effects of material parameters on the response of charring ablative materials.

The thesis is composed of six themed chapters, including this introductory chapter. Chapter 2 gives a detailed description of the thermal ablation phenomena along with the governing equations. Chapter 3 deals with the numerical implementation of the

governing equations and the solution procedure. This chapter also includes the code and solution verification studies. Chapter 4 extends the previous chapters by addressing the thermal and chemical non-equilibrium phenomena. This chapter also covers additional verification and validation studies. Chapter 5 demonstrates the results of the numerical simulations and explores the effects of various modeling assumptions and material parameters on the response of ablative materials. The final chapter, i.e. Chapter 6, recapitulates the key findings drawn from the simulation results and identifies the areas for further research.

CHAPTER 2

PHYSICAL DESCRIPTION OF THE THERMAL ABLATION PHENOMENA

The ablation process of a charring ablative material is rather complex and incorporates a substantial number of physical and chemical phenomena that are, in general, mutually interacting. Some possible physical and chemical couplings can be listed as:

- Exposed surface of the material may melt, sublime, or react with the boundary layer gases. In addition, mechanical erosion may occur.
- During decomposition of the solid, i.e. pyrolysis process, porosity of the material increases, internal gas flow takes place.
- Produced pyrolysis gas species may react with each other, the char and boundary layer gases.
- Surface recession and associated shape change can alter the mass, momentum, and energy transfers through the material.

Despite including numerous physical and chemical events, the ablation process can be simply though to be governed by interaction of the ablating surface with the boundary layer gases and the characteristic behavior and properties of the material underneath the ablating surface. Then, modeling of thermal ablation basically comprises modeling of ([37]):

- Subsurface, i.e. in-depth, phenomena affecting the ablation process such as energy absorption, heat conduction and advection, thermal decomposition, flow

of pyrolysis gases, radiative transport and chemical reactions occurring through the thickness of the material, and

- Surface phenomena affecting the characteristics of the boundary layer such as the interaction of the boundary layer gases with the receding solid surface and pyrolysis gases by means of heterogeneous chemical reactions and transpiration effects of the blowing gases.

Several researchers [38, 39] have claimed that species from the boundary layer gases, in particular oxygen, may diffuse into highly porous ablative materials at low pressures and react in-depth with char resulting in mass loss. Thus, it is put forth that ablation is, indeed, a surface/volume phenomenon and the competition between surface and volume ablations relies on the flow conditions. In this work, the volume ablation concept is not considered, and it is assumed that ablation takes place only on the surface. Furthermore, in this chapter the ablation process is described assuming local thermal and chemical equilibrium. Thermal and chemical non-equilibrium is addressed in Chapter 4.

2.1 Subsurface Phenomena

In this section, governing equations for the in-depth thermal response of charring ablative materials is presented. The *in-depth* term is used to bracket the physical and/or chemical phenomena occurring beneath the ablating surface such as material decomposition, generation and flow of pyrolysis gases, heat conduction through the material and energy absorption. The governing equations can be grouped as:

- Material Decomposition, i.e. Pyrolysis Kinetics
- Subsurface Mass Balance
- Subsurface Momentum Balance
- Subsurface Energy Balance

2.1.1 Material Decomposition

As the temperature of the solid increases, it undergoes thermal decomposition and as a result pyrolysis gases are generated. The pyrolysis process can be simply described by the following relation [40]:

$$virgin \rightarrow char + gas \tag{2.1}$$

As thermal decomposition progresses, the solid bulk density, ρ_s, decreases from its primary virgin value, ρ_v, to the ultimate charred value, ρ_{ch}. The degree of material decomposition is quantified by defining the overall extent-of-reaction, ι, as:

$$\iota = \frac{\rho_v - \rho_s}{\rho_v - \rho_{ch}} \tag{2.2}$$

The extent-of-reaction increases from its initial value 0 to its final value 1 as the solid decomposes from virgin to char. The bulk density of the solid during pyrolysis can then be expressed in terms of the extent-of-reaction as:

$$\rho_s = (1 - \iota)\rho_v + \iota\rho_{ch} \tag{2.3}$$

Goldstein [41] demonstrated that for most phenolic resin-based composites the pyrolysis process can be described using a three-step kinetic equation: A two-step kinetic equation for resin decomposition and a single-step kinetic equation for the fiber decomposition. The solid bulk density, ρ_s, can be defined in the following way in order to model the proposed three-stage decomposition mechanism.

$$\rho_s = \Gamma(\rho_A + \rho_B) + (1 - \Gamma)\rho_C \tag{2.4}$$

where Γ is the initial resin volume fraction, the subscripts *A* and *B* stand for the constituents of the resin, and the subscript *C* represents the reinforcing fiber component. Eq. 2.4 can be expressed in terms of units as:

$$\underbrace{\frac{\text{solid mass}}{\text{total volume}}}_{\rho_s} = \underbrace{\frac{\text{initial resin volume}}{\text{total volume}}}_{\Gamma} \left(\underbrace{\frac{\text{component A mass}}{\text{initial resin volume}}}_{\rho_A} + \underbrace{\frac{\text{component B mass}}{\text{initial resin volume}}}_{\rho_B} \right) + \underbrace{\frac{\text{initial fiber volume}}{\text{total volume}}}_{1-\Gamma} \underbrace{\frac{\text{fiber mass}}{\text{initial fiber volume}}}_{\rho_C} \tag{2.5}$$

Total volume of the material remains constant unless thermal expansion of the material is taken into account, therefore, Γ does not change. It is also worth noting that modeling of solid as a mixture of three components is a modeling approach that comes from the thermal decomposition data extracted from Thermal Gravimetric Analysis (TGA). The decomposition rate of the solid can be expressed in terms of the decomposition rates of the components by taking the temporal derivative of Eq. 2.4.

$$\frac{\partial \rho_s}{\partial t} = \Gamma \left(\frac{\partial \rho_A}{\partial t} + \frac{\partial \rho_B}{\partial t} \right) + (1 - \Gamma) \frac{\partial \rho_C}{\partial t} \tag{2.6}$$

Decomposition rate for each component can be expressed with an Arrhenius type reaction model as:

$$\frac{\partial \rho_i}{\partial t} = -Z_i \rho_{v,i} \left(\frac{\rho_i - \rho_{ch,i}}{\rho_{v,i}} \right)^{\psi_i} e^{-E_{a,i}/(R_u T)}, \quad i = A, B, C \tag{2.7}$$

where Z is the pre-exponential factor, E_a is the activation energy, ψ is the order of the reaction, R_u is the universal gas constant, and T stands for temperature. The parameters in Eq. 2.7 can be determined empirically via TGA. For phenolic resins, values found in the literature are listed in Table 2.1. In most applications, decomposition of the reinforcing fiber component is not taken into account because the fiber is made of either silica or carbon and these materials can withstand very high temperatures.

Table 2.1: Decomposition parameters for phenolic resins

Source	Component	Z_i, s^{-1}	$\frac{E_{a,i}}{R_u}, K$	ψ_i
Ahn et al. [42]	A	677	3544	2
	B	1.64×10^9	19 680	2
Henderson et al. [43]	A	4.7×10^{16}	24 536	1
	B	4.96×10^{14}	25 137	1

Decomposition rate of the solid can also be expressed in terms of evolution of extent-of-reactions of each reaction, ι_i, assuming pyrolysis process is a combination of multiple reactions. In this approach, temporal derivative of the extent-of-reactions are described in Arrhenius form. Although two approaches are mathematically equivalent, the latter is claimed to be more convenient in the derivation of the governing

equations [44]. However, in this work, the conventional multi-component approach is adopted to describe the pyrolysis process.

2.1.2 Subsurface Mass Balance

The mixture density of the solid and pyrolysis gases can be described as:

$$\rho = \rho_s + \epsilon\rho_{pg} \tag{2.8}$$

where ϵ is the porosity of the material, i.e. the ratio of the pore/gas volume to the overall mixture volume, and the subscripts pg and s stand for the pyrolysis gases and solid, respectively. At this point it should be noted that whereas the gas density is a true density, the solid density is a bulk density, i.e. the ratio of the solid mass to the overall volume. As the pyrolysis process goes through, porosity of the material increases since the solid phase is transformed into gases and void spaces are left behind. In other words, solid is consumed, and pyrolysis gases are generated consequently.

A one dimensional control volume for the gas phase mass balance within the porous material is shown in Figure 2.1. The volumetric gas generation term, $\dot{m}'''_{gen}$, is associated with the pyrolysis process and is exactly equal to the solid density change. This gives the gas generation in a control volume, $\dot{m}_{gen}$, as:

$$\dot{m}_{gen} = \dot{m}'''_{gen} S\mathrm{d}z = -\frac{\partial \rho_s}{\partial t} S\mathrm{d}z \tag{2.9}$$

where S is the surface area and $\mathrm{d}z$ is the infinitesimal thickness of the control volume.

The pyrolysis gases enter the control volume from the positive side of z, i.e. $z + \mathrm{d}z$, and leave from the negative side of z. The net mass flow entering into the control volume, $\dot{m}_{net}$, can be written as:

$$\dot{m}_{net} = \dot{m}_{pg_{z+\mathrm{d}z}} - \dot{m}_{pg_z} = \dot{m}''_{pg_{z+\mathrm{d}z}} S - \dot{m}''_{pg_z} S = \frac{\partial}{\partial z}(\dot{m}''_{pg} S)\mathrm{d}z \tag{2.10}$$

The mass storage rate of pyrolysis gases, $\dot{m}_{st}$, in the solid pores is:

$$\dot{m}_{st} = \frac{\partial}{\partial t}(\epsilon\rho_{pg}) S\mathrm{d}z \tag{2.11}$$

The conservation of mass for the gaseous phase enforces that the mass storage rate in the control volume must be balanced with sum of the net gas in-flow and gas generation. Then, the combination of Eqs. 2.9, 2.10 and 2.11 gives the conservation of mass equation for the pyrolysis gases as:

$$\frac{\partial}{\partial t}(\epsilon\rho_{pg}) = \frac{1}{S}\frac{\partial}{\partial z}(\dot{m}''_{pg}S) - \frac{\partial\rho_s}{\partial t} \tag{2.12}$$

Pyrolysis gases are assumed to obey the perfect gas law, and then the gas phase density can be expressed as a function of pressure, p, and temperature as:

$$\rho_{pg} = \frac{p}{T}\frac{MW}{R_u} \tag{2.13}$$

where MW is the molecular weight of the pyrolysis gas mixture.

Governing equations given for the description of the pyrolysis process in section 2.1.1 define, indeed, the mass conservation of the solid phase. It may be convenient to reiterate that time change of the solid density is equal to the rate at which pyrolysis gases are generated.

$$\frac{\partial\rho_s}{\partial t} = -\dot{m}'''_{gen} \tag{2.14}$$

2.1.3 Subsurface Momentum Balance

In a porous medium, instead of standard momentum conservation equation, i.e. Navier-Stokes, velocity of a fluid is calculated using Darcy's law. In 1856, Henry Darcy introduced his empirical relation [45] that expresses the average mass flow rate of fluid

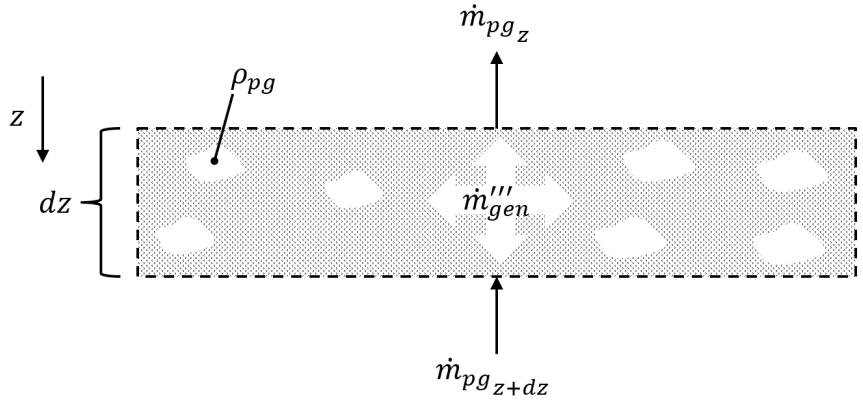


Figure 2.1: One-dimensional control volume for pyrolysis gas mass balance

passing through a porous medium in terms of pressure gradient over a given distance as a result of his experimental work on water flow through uniform-sized particles of sands. The fluid flow is illustrated in Figure 2.2. The average velocity of the fluid was determined by dividing the mass flow rate by the product of density of the fluid and the cross-sectional area. The average fluid velocity, which is in general called as *filter* (or Darcy or superficial) velocity, u_D, is written as:

$$u_D = -\frac{\kappa}{\mu}\frac{\partial p}{\partial z} \tag{2.15}$$

where the proportionality constant, κ, is known as permeability of the medium, and μ is the viscosity of the fluid.

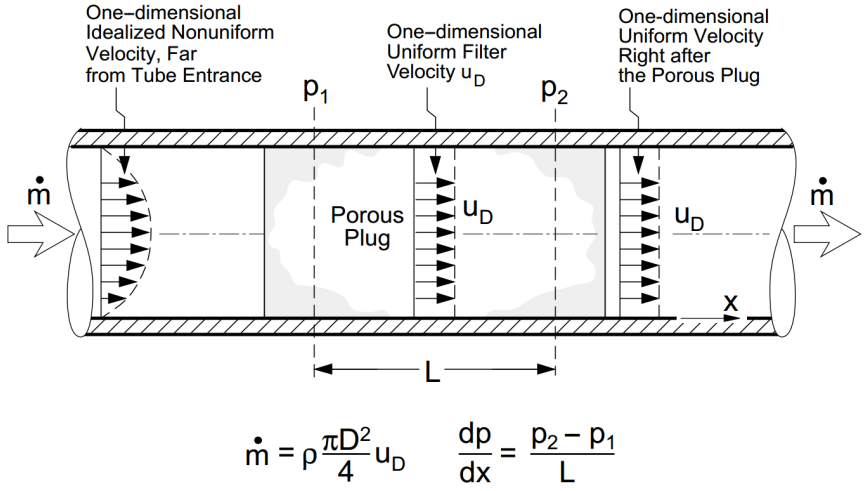


Figure 2.2: Determination of filter (Darcy or superficial) velocity [46]

The filter velocity is not the actual velocity which the fluid flowing in the pores of the medium. The true (actual) velocity of the fluid passing through the pores can be evaluated by dividing the filter velocity by the porosity of the medium. In case of pyrolysis gas flow inside the ablative material, the true velocity of the pyrolysis gases, u_{pg}, can be written as:

$$u_{pg} = -\frac{\kappa}{\epsilon\mu_{pg}}\frac{\partial p}{\partial z} \tag{2.16}$$

The mass flow rate of the pyrolysis gases, then, can be written in terms of pressure gradient as:

$$\dot{m}_{pg} = \epsilon\rho_{pg}u_{pg}S = -\rho_{pg}\frac{\kappa}{\mu_{pg}}\frac{\partial p}{\partial z}S \tag{2.17}$$

2.1.4 Subsurface Energy Balance

A one-dimensional control volume for energy balance within the ablative material is depicted in Figure 2.3. Within the ablative material, both the solid and gas phases store energy and then the rate of change of the energy content of the solid and gas mixture can be written as:

$$\frac{\partial}{\partial t}(\rho e)S\mathrm{d}z = \frac{\partial}{\partial t}(\rho_s e_s + \epsilon\rho_{pg} e_{pg})S\mathrm{d}z \tag{2.18}$$

where e denotes the internal energy.

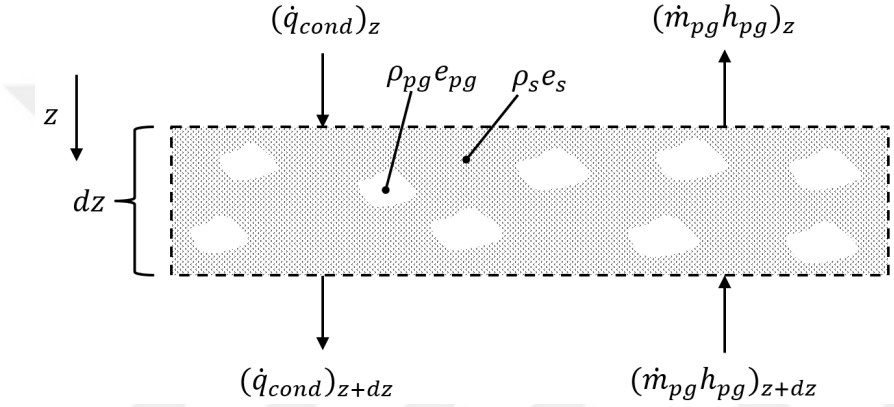


Figure 2.3: One-dimensional control volume for energy balance

The conservation of energy principle imposes that the change in the energy content of the control volume must be balanced with the energy entering and leaving the control volume. Energy entering and leaving the control volume has two sources: 1) heat conduction, $\dot{q}_{cond}$, and 2) flow of pyrolysis gases, $\dot{m}_{pg}h_{pg}$. Here, it should be noted that the sum of the kinetic energy and potential energy of the pyrolysis gases is assumed to be negligible compared to the sensible energy of the gases. The energy conservation equation for the solid and gas mixture under local thermal equilibrium assumption can be written as:

$$\begin{aligned}\frac{\partial}{\partial t}(\rho e)S\mathrm{d}z &= [(\dot{q}_{cond})_z - (\dot{q}_{cond})_{z+\mathrm{d}z}] + [(\dot{m}_{pg}h_{pg})_{z+\mathrm{d}z} - (\dot{m}_{pg}h_{pg})_z] \\ &= -\frac{\partial \dot{q}_{cond}}{\partial z}\mathrm{d}z + \frac{\partial}{\partial z}(\dot{m}_{pg}h_{pg})\mathrm{d}z\end{aligned} \tag{2.19}$$

where h is the enthalpy.

Using Fourier's law and dividing both sides of Eq. 2.19 by $A\mathrm{d}z$, the differential form of the subsurface energy conservation equation can be written as:

$$\frac{\partial}{\partial t}(\rho_s e_s + \epsilon \rho_{pg} e_{pg}) = \frac{\partial}{\partial z}\left(k_{\mathit{eff}} \frac{\partial T}{\partial z}\right) + \frac{\partial}{\partial z}(\dot{m}''_{pg} h_{pg}) \tag{2.20}$$

where k_{eff} is the effective thermal conductivity of the solid and gas mixture and $\dot{m}''_{pg}$ is the mass flux of the pyrolysis gases. Effective thermal conductivity of a porous medium depends in a complex fashion on the structure of the medium [47] and conductivities of the solid and fluid phases. It can be determined experimentally [48, 49] or analytically [50, 51] through simplifications such that one may assume that heat conduction in the phases takes place either in parallel or in series. Eq. 2.21 gives widely used expressions for evaluation of the effective thermal conductivity. Parallel and series orientation formulas fix upper and lower bounds to the combination of different phases, respectively. In this work, heat conduction in the phases is assumed to be in parallel based on the following reasons. First, in order to maintain its mechanical strength, the solid phase has to be continuous. Therefore, series arrangement of the solid and gas phases would be impractical. Secondly, the parallel orientation formula can be derived through volume averaging of phase properties and is consistent with the two-equation model that is used to model thermal non-equilibrium between the phases.

$$\begin{aligned} k_{\mathit{eff}} &= \epsilon k_{pg} + (1-\epsilon) k_s, \quad \text{(parallel orientation)} \\ \frac{1}{k_{\mathit{eff}}} &= \frac{\epsilon}{k_{pg}} + \frac{1-\epsilon}{k_s}, \quad \text{(series orientation)} \\ k_{\mathit{eff}} &= k_{pg}^{\epsilon} k_s^{1-\epsilon}, \quad \text{(weighted geometric mean)} \end{aligned} \tag{2.21}$$

2.1.5 Governing Equations in Integral Form

In the preceding subsections the governing equations are presented in differential form for clarity. However, it is more convenient to express the governing equations in integral form since the finite volume method is adopted to discretize them. In the following equations, the bold type represents vectorial quantities.

The mixture continuity equation in integral form is:

$$\underbrace{\frac{\mathrm{d}}{\mathrm{d}t}\iiint \rho \mathrm{d}V}_{\text{mass storage}} + \underbrace{\iint \epsilon \rho_{pg} \mathbf{u_{pg}} \cdot \mathbf{n} \mathrm{d}S}_{\text{gas flow}} = 0 \tag{2.22}$$

where V denotes the volume and $\mathbf{n}$ is the outward normal of the surface. The mixture continuity equation is, indeed, sum of the solid and gas phase continuity equations given in Eq. 2.23 and Eq. 2.24, respectively.

$$\frac{\mathrm{d}}{\mathrm{d}t}\iiint \rho_s \mathrm{d}V = -\iiint \dot{m}'''_{gen}\mathrm{d}V \tag{2.23}$$

$$\frac{\mathrm{d}}{\mathrm{d}t}\iiint \epsilon\rho_{pg}\mathrm{d}V + \iint \epsilon\rho_{pg}\mathbf{u_{pg}}\cdot\mathbf{n}\mathrm{d}S = \iiint \dot{m}'''_{gen}\mathrm{d}V \tag{2.24}$$

The mixture energy equation in integral form is:

$$\underbrace{\frac{\mathrm{d}}{\mathrm{d}t}\iiint \rho e \mathrm{d}V}_{\text{energy storage}} + \underbrace{\iint \dot{\mathbf{q}}''_{\mathbf{cond}}\cdot\mathbf{n}\mathrm{d}S}_{\text{conduction}} + \underbrace{\iint \epsilon\rho_{pg}h_{pg}\mathbf{u_{pg}}\cdot\mathbf{n}\mathrm{d}S}_{\text{gas flow}} = 0 \tag{2.25}$$

which is sum of the solid and gas phase energy equations given in Eq. 2.26 and Eq. 2.27, respectively.

$$\frac{\mathrm{d}}{\mathrm{d}t}\iiint \rho_s e_s \mathrm{d}V + \iint \dot{\mathbf{q}}''_{\mathbf{cond_s}}\cdot\mathbf{n}\mathrm{d}S = 0 \tag{2.26}$$

$$\frac{\mathrm{d}}{\mathrm{d}t}\iiint \epsilon\rho_{pg}e_{pg}\mathrm{d}V + \iint \dot{\mathbf{q}}''_{\mathbf{cond_{pg}}}\cdot\mathbf{n}\mathrm{d}S + \iint \epsilon\rho_{pg}h_{pg}\mathbf{u_{pg}}\cdot\mathbf{n}\mathrm{d}S = 0 \tag{2.27}$$

2.2 Surface Phenomena

The governing equations describing the subsurface phenomena have to be solved with appropriate boundary conditions. Implementation of boundary conditions which do not include the interaction of the boundary layer gases with pyrolysis gases and the ablating surface, e.g. prescribed temperature or heat flux with and without given surface recession, is quite straightforward. Therefore, they are not addressed in this work. Instead, the adopted surface thermo-chemical ablation model is presented.

The thermo-chemical ablation model requires the solution of the mass and energy balances at the ablating surface along with the subsurface governing equations. In other words, it couples the in-depth response of the charring ablative material and the boundary layer. The surface recession rate is, thus, a part of the solution.

2.2.1 Surface Mass Balance

In reactive flow problems the boundary conditions across an interface are derived by writing the conservation equations in integral form and then passing to the limit in which the volume of integration approaches a surface [52]. Then, to obtain the surface mass balance equation, the species conservation equation is considered. For a single gaseous species i, the species conservation equation in a movable control volume can be written as:

$$\frac{\mathrm{d}}{\mathrm{d}t}\iiint \rho Y_i \mathrm{d}V + \iint [\rho Y_i(\mathbf{u} - \mathbf{u_s} + \mathbf{U_{k,i}})] \cdot \mathbf{n}\mathrm{d}S = \iiint \dot{m}_i^{'''}\mathrm{d}V \tag{2.28}$$

where Y is the species mass fraction, $\mathbf{u}$ is the local mixture velocity, $\mathbf{u_s}$ is the velocity of the control volume, $\mathbf{U_k}$ is the local diffusion velocity and $\dot{m}_i^{'''}$ is the mass production rate. The diffusion velocity of a species i can be approximated using Fick's law of diffusion as:

$$\mathbf{U_{k,i}} = -D_{im}\nabla(\ln Y_i) \tag{2.29}$$

where D_{im} is the multi-component diffusion coefficient.

Figure 2.4 illustrates a thin control volume at the interface between a porous ablative medium and its environment. The upper and lower surfaces of the control volume is denoted as $+$ and $-$. The corresponding outward normals are $\mathbf{n}_+$ and $\mathbf{n}_-$, respectively. Assuming no mass accumulation in the thin control volume and considering that:

$$\lim_{V\to 0}\iiint \dot{m}_i^{'''}\mathrm{d}V = \iint \dot{m}_i^{''}\mathrm{d}S \tag{2.30}$$

where $\dot{m}_i^{''}$ is mass production rate per unit surface area, the species conservation equation can be written by taking the limit of the thickness of the control volume to zero as:

$$\begin{aligned}\iint [&\rho_+ Y_{i+}(\mathbf{u}_+ - \mathbf{u_{s+}} - D_{im+}\nabla(\ln Y_{i+})) \\ &-\rho_- Y_{i-}(\mathbf{u}_- - \mathbf{u_{s-}} - D_{im-}\nabla(\ln Y_{i-}))] \cdot \mathbf{n}_+ \mathrm{d}S = \iint \dot{m}_i^{''}\mathrm{d}S\end{aligned} \tag{2.31}$$

Eq. 2.31 can be written for an arbitrary control volume as:

$$\begin{aligned}&[\rho_+ Y_{i+}(\mathbf{u}_+ - \mathbf{u_{s+}} - D_{im+}\nabla(\ln Y_{i+})) \\ &-\rho_- Y_{i-}(\mathbf{u}_- - \mathbf{u_{s-}} - D_{im-}\nabla(\ln Y_{i-}))] \cdot \mathbf{n}_+ = \dot{m}_i^{''}\end{aligned} \tag{2.32}$$

As shown in Figure 2.4, the $+$ sign represents the gases outside the ablative material, and the $-$ sign represents the porous charring ablative material. Noting that the velocity of the solid char is zero and thus $\mathbf{u}_-$ is the velocity of the pyrolysis gases just beneath the ablating surface and assuming that gas velocity is much larger than the velocity of the control volume, the terms of Eq. 2.32 can be split as:

$$\begin{aligned}
\rho_+ Y_{i+}(\mathbf{u}_+ - \mathbf{u}_{\mathbf{s}+}) \cdot \mathbf{n}_+ &= (\rho u Y_i)_w \\
\rho_+ Y_{i+}(D_{im+}\nabla(\ln Y_{i+})) \cdot \mathbf{n}_+ &= \rho D_{im} \left.\frac{\partial Y_i}{\partial z}\right|_w \\
\rho_- Y_{i-}(\mathbf{u}_- - \mathbf{u}_{\mathbf{s}-}) \cdot \mathbf{n}_+ &= \dot{m}''_{pg} Y_{i,pg} \\
\rho_- Y_{i-}(D_{im-}\nabla(\ln Y_{i-})) \cdot \mathbf{n}_+ &= 0 \\
\dot{m}''_i &= \dot{m}''_{ch} Y_{i,ch}
\end{aligned} \tag{2.33}$$

where the subscript w refers to the properties at the wall, i.e. ablation surface, and the subscript ch denotes the char. It should be restated that subsurface diffusion is neglected in this work. Thus, the forth term of Eq. 2.32 is set to zero. The surface mass balance for a gaseous species i is illustrated in Figure 2.5 and expressed as:

$$\rho D_{im} \left.\frac{\partial Y_i}{\partial z}\right|_w + \dot{m}''_{pg} Y_{i,pg} + \dot{m}''_{ch} Y_{i,ch} = (\rho u Y_i)_w \tag{2.34}$$

The first term in Eq. 2.34 can be approximated in terms of mass transfer Stanton number, C_m, as [53]:

$$\rho D_{im} \frac{\partial Y_i}{\partial z} = \rho_e u_e C_m (Y_{i,e} - Y_{i,w}) \tag{2.35}$$

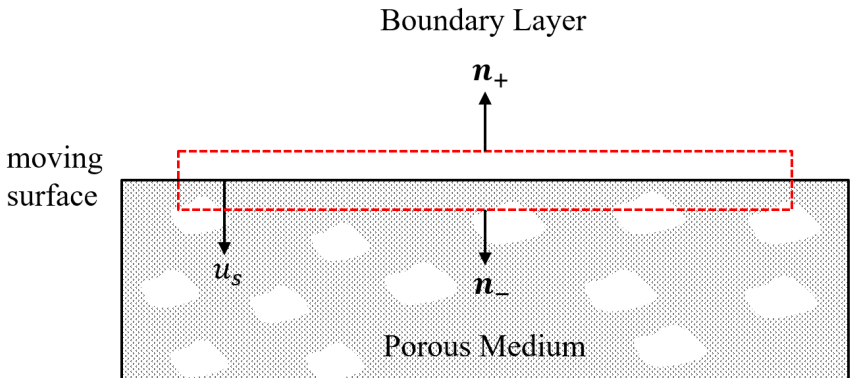


Figure 2.4: Control volume for the derivation of interface conditions

where the subscript e denotes the properties at the edge of the boundary layer.

Summing Eq. 2.34 over all species gives the global mass balance at the ablating surface as:

$$\dot{m}''_{pg} + \dot{m}''_{ch} = \dot{m}''_{blow} = (\rho u)_w \tag{2.36}$$

It is worth noting that the convected gaseous mass flux out of the ablative material, $\dot{m}''_{blow}$, reduces the aerodynamic heating rate. This phenomenon is known as *blowing effect*. In addition, it is convenient to introduce the following non-dimensional mass fluxes for the char, B_{ch}, and pyrolysis gases, B_{pg}, as:

$$B_{ch} = \frac{\dot{m}''_{ch}}{\rho_e u_e C_m} \tag{2.37}$$

$$B_{pg} = \frac{\dot{m}''_{pg}}{\rho_e u_e C_m} \tag{2.38}$$

Then, the total non-dimensional mass flux, i.e. the *blowing parameter*, B, can be defined as:

$$B = B_{ch} + B_{pg} = \frac{\dot{m}''_{ch} + \dot{m}''_{pg}}{\rho_e u_e C_m} = \frac{\dot{m}''_{blow}}{\rho_e u_e C_m} \tag{2.39}$$

2.2.2 Surface Energy Balance

The surface energy balance equation can also be obtained by writing the energy conservation equation in integral form and then taking the limit of the thickness of the

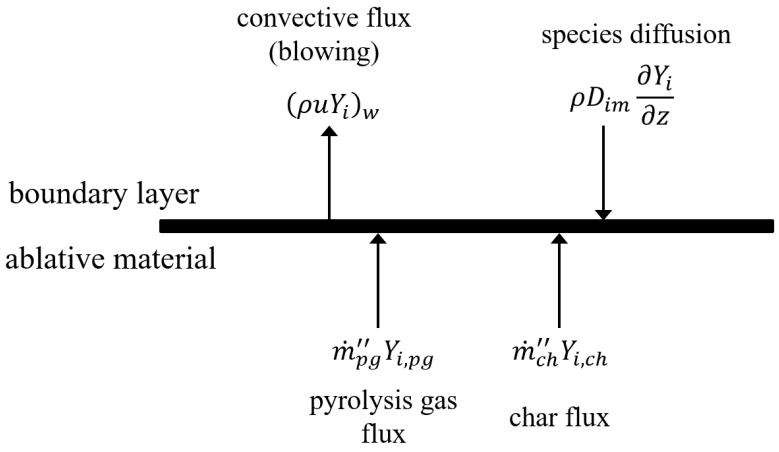


Figure 2.5: Surface mass balance for a species

control volume to zero as done for the surface mass balance. However, derivation is omitted and only the global energy balance at the surface is given for brevity. Figure 2.6 depicts the surface energy balance at the ablating surface of a charring ablative material. The surface energy balance can be written as:

$$k \left.\frac{\partial T}{\partial z}\right|_w + \sum_{i=1}^{N_s} \rho h_i D_{im} \left.\frac{\partial Y_i}{\partial z}\right|_w + \dot{q}''_{rad-in} + \dot{m}''_{pg} h_{pg} + \dot{m}''_{ch} h_{ch} = \rho u h_w + \dot{q}''_{rad-out} + \dot{q}''_{cond} \tag{2.40}$$

where N_s is the number of species. The terms on the left-hand side are the energy fluxes entering the control volume due to conduction from the hot boundary gases, species diffusion, radiation and the solid char and pyrolysis gas mass flow rate, respectively. The terms on the right-hand side are the energy fluxes leaving the control volume due to blowing, re-radiation, and conduction into the material.

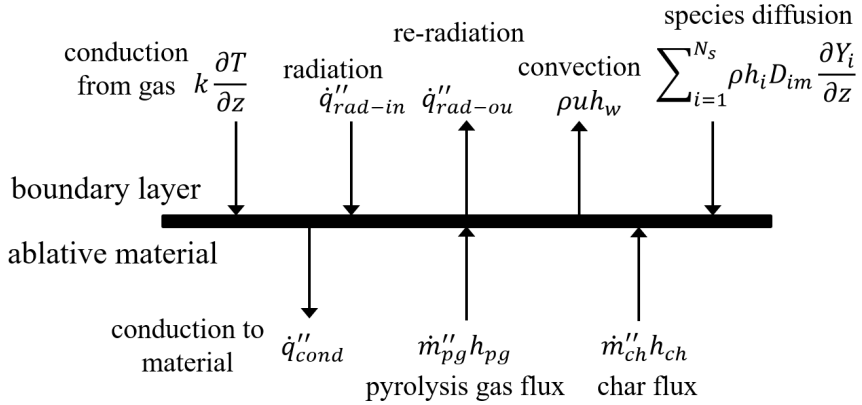


Figure 2.6: Surface energy balance

Combination of the first two terms in Eq 2.40 is referred to thermo-chemical convection, $\dot{q}_{tch}{}''$. By assuming equal diffusion coefficients for all species and equality of heat transfer Stanton number, C_h, and mass transfer Stanton number, i.e. $C_h/C_m = 1$, the thermo-chemical convection can be expressed as [53]:

$$\dot{q}''_{tch} = \rho_e u_e C'_h (h_r - h_w) \tag{2.41}$$

where C'_h is the modified heat transfer Stanton number that considers the blowing effect and h_r is the recovery enthalpy. The recovery enthalpy is expressed as:

$$h_r = h_e + 0.5 r_c u_e^2 \tag{2.42}$$

where r_c is the so-called recovery factor having the approximate values of 0.85 and 0.89 for laminar and turbulent air flow, respectively. The modified heat transfer Stanton number can be estimated using the blowing parameter, B, as [54]:

$$\frac{C_h^{'}}{C_h} = \frac{2B}{e^{2\lambda B} - 1} \tag{2.43}$$

where λ is a parameter having the values of 0.5 and 0.4 for laminar and turbulent flow, respectively.

Substituting Eq. 2.41 into Eq. 2.40 gives the surface energy balance equation as:

$$\rho_e u_e C_h^{'}[(h_r - h_w) - B^{'} h_w + B_{ch}^{'} h_{ch} + B_{pg}^{'} h_{pg}] + \dot{q}_{rad-in}^{''} - \dot{q}_{rad-out}^{''} - \dot{q}_{cond}^{''} = 0 \tag{2.44}$$

where $B_{ch}^{'}$, $B_{pg}^{'}$ and $B^{'}$ are the modified non-dimensional mass fluxes. The modified non-dimensional mass fluxes are obtained by replacing C_m with $C_h^{'}$ in Eqs. 2.37, 2.38 and 2.39. The solution of Eq. 2.44 along with in-depth material response equations gives the temperature distribution over the ablative material and surface recession rate at the ablating surface.

CHAPTER 3

NUMERICAL MODELING OF THERMAL ABLATION

In this chapter, numerical implementation of the governing equations described in Chapter 2 and results of the verification studies are presented. It should be noted that thermal and chemical non-equilibrium is not considered in this chapter. In other words, local temperatures of the solid and pyrolysis gases are assumed to be equal, and pyrolysis gas mixture is assumed to be in chemical equilibrium. The chemical equilibrium assumption allows treating the pyrolysis gases as a single entity whose thermodynamic and transport properties can be tabulated as a function of temperature and pressure in advance, once the species in the mixture and elemental composition are specified.

3.1 Implementation of Governing Equations

3.1.1 Space Discretization

The vertex-centered finite volume method (FVM) is adopted to discretize the physical domain. As shown in Figure 3.1 in this arrangement the solution variables are defined at the vertices with elements formed around the vertex by using the dual-mesh concept in contrast to the cell-centered arrangement in which the variables are stored at the centroids of elements. For one-dimensional domain each node j is associated with a control volume. Control volume boundaries are always located at the mid-points of the neighboring nodes, but the nodes are not located at control volume centers when $\Delta z_j \neq \Delta z_{j-1}$, as shown in Figure 3.2.

While the cell-centered arrangement is generally preferred in computation heat trans-

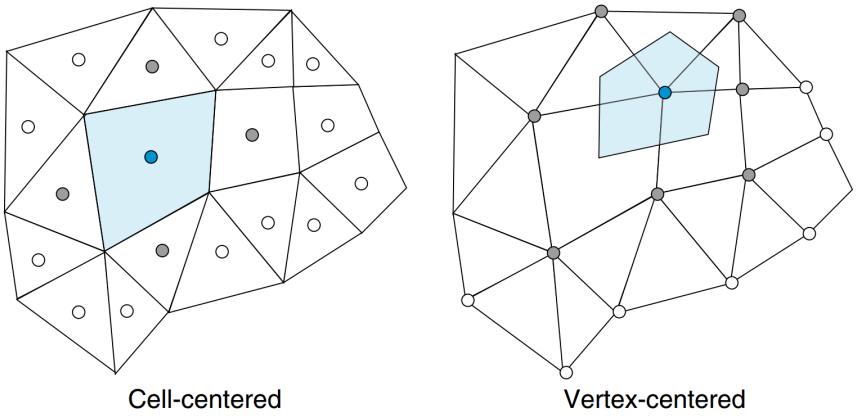


Figure 3.1: Variable arrangements in FVM [55]

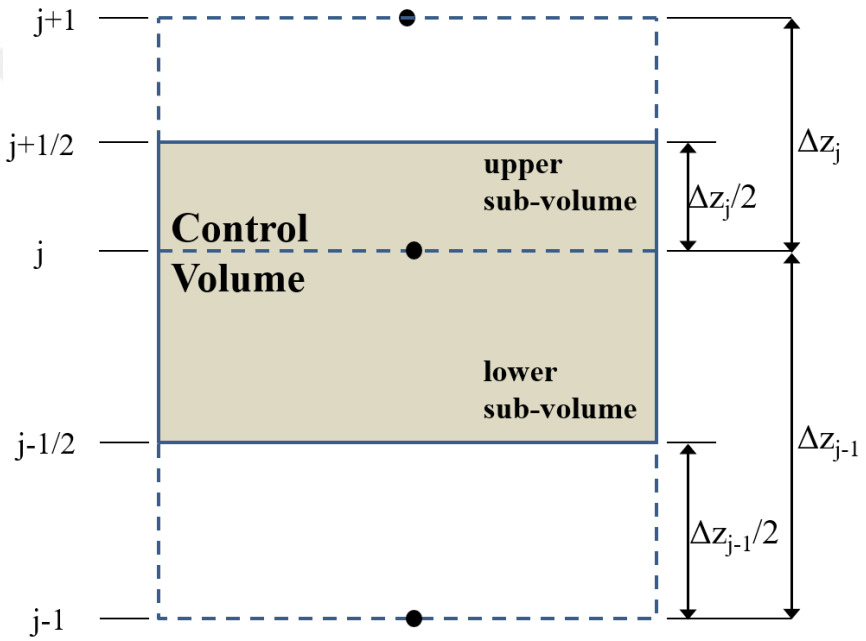


Figure 3.2: Control volume for node j

fer applications and is recommended in textbooks [56, 57], the choice of the vertex-centered scheme provides two main advantages. First, since the control volume faces are always equidistant from the adjacent nodes and the interpolation factor is 0.5, in case of non-uniform grids the interpolation at the faces is much easier. The use of non-uniform grids seems to be appealing in ablation problems because high gradients are expected close to the ablating surface. Secondly, placing of nodes on the boundaries simplifies the tracking of the grid nodes during surface recession. In addition, it is stated that the vertex-centered scheme gives better performance in terms

of consistency and efficiency than the cell-centered scheme over a distorted grid [55].

3.1.2 Grid Movement

The ablation problem naturally includes the recession of the surface. As a result, a special treatment is required to handle the boundary movement of the grid. There exist several approaches for the solution of moving boundary problems in the literature. These methods can be grouped under two headings [58]: 1) front-tracking schemes, and 2) front-fixing schemes. In the former, the position of the moving surface is computed and tracked as the surface moves, and the solution domain is regularly updated such that either a completely new grid is created or the mesh is modified in the neighborhood of the moving boundary. The solution variables are then mapped from the old grid points to the new grid points. In the latter, by choosing appropriate new space coordinates the moving surface is fixed in the transformed solution domain. Thus, at each time step updating the grid is avoided. However, an additional convective term is added to the governing equations to account for the effects of moving boundary.

In the solution of ablation problems, both front-tracking [13, 23, 28, 29, 44, 59, 60] and front-fixing [17, 19–21, 61] methods have been implemented successfully by various researchers. Front-tracking methods are more generalized as they can be implemented in multi-domain problems with non-structural meshes unlike front-fixing methods. Another drawback of the implementation of front-fixing methods in ablation problems is reported as that instantaneous mechanical spallation cannot be modeled because the additional convective term in the energy equation becomes infinite [44]. However, in this work, contracting grid scheme, a front-fixing method, proposed by Blackwell and Hogan [17] is adopted. Since mechanical spallation is not taken into account and one-dimensional problems are considered in this work, instead of updating the grid at each time step discretization of additional convective terms in the governing equations is assessed to be more practical.

The contraction grid scheme transforms the spatial coordinate by the method of Landau [18] such that the thickness of the ablative material is always unity in the new coordinate system. Thus, relative size and total number of the control volumes are constant during solution. The contracting grid scheme is delineated in Figure 3.3.

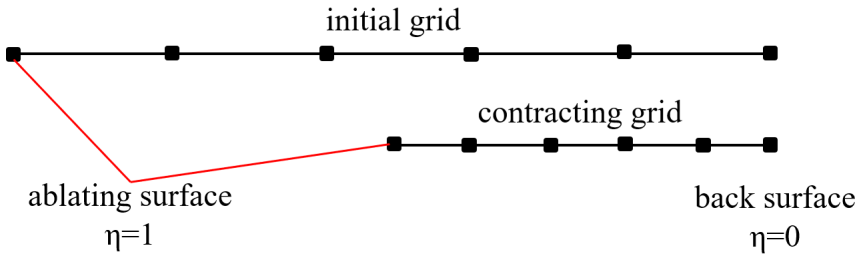


Figure 3.3: Contracting grid scheme

In one-dimensional ablation problems, the Landau transformation is mathematically expressed as:

$$\eta = \frac{L_o - z}{L_o - s(t)} = \frac{L(t) - x}{L(t)} \tag{3.1}$$

where η is the Landau coordinate, L_o is the initial thickness of the ablative material, $L(t)$ is the thickness at time t, $s(t)$ is the total surface recession at time t, x is the distance from the ablating surface, and z is the distance from the initial position of the ablating surface. These parameters are shown in Figure 3.4.

It should be noted that the Landau coordinate, η, of a node is fixed throughout the solution and the coordinates at the boundaries are:

$$\begin{aligned} &\eta = 1, x = 0, z = s(t) \quad \text{(at the ablating surface)} \\ &\eta = 0, x = L(t), z = L_o \quad \text{(at the back surface)} \end{aligned} \tag{3.2}$$

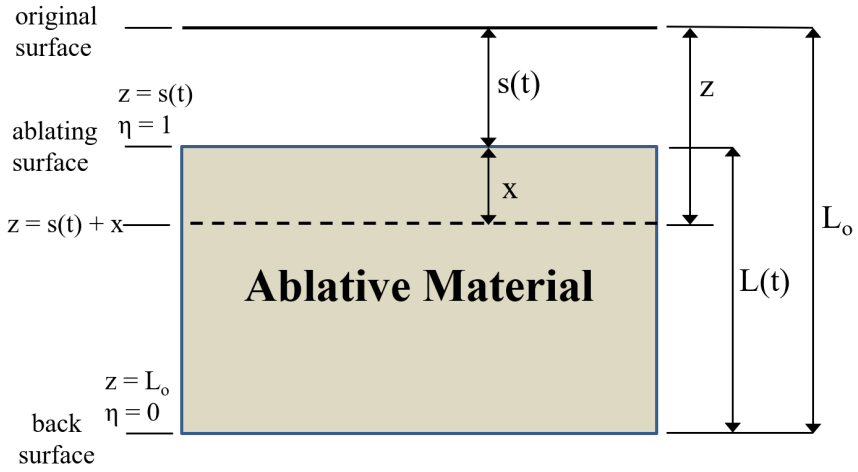


Figure 3.4: Schematic of Landau transformation for one-dimensional planar geometries

3.1.3 Governing Equations in Moving Grid

As stated in the previous subsection, the implementation of the contracting grid scheme requires addition of a convective term into the governing equations to account for the effects of surface recession. Thus, it is convenient to express the final form of the governing equations that are solved.

The mixture continuity equation in integral form becomes:

$$\underbrace{\frac{\mathrm{d}}{\mathrm{d}t}\iiint \rho \mathrm{d}V}_{\text{mass storage}} + \underbrace{\iint \epsilon\rho_{pg}\mathbf{u_{pg}}\cdot\mathbf{n}\mathrm{d}S}_{\text{gas flow}} - \underbrace{\iint \rho\mathbf{u_{cs}}\cdot\mathbf{n}\mathrm{d}S}_{\text{grid convection}} = 0 \tag{3.3}$$

where $\mathbf{u_{cs}}$ is the velocity of the control surface. The solid and gas phase continuity equations can be written separately as:

$$\frac{\mathrm{d}}{\mathrm{d}t}\iiint \rho_s \mathrm{d}V - \iint \rho_s\mathbf{u_{cs}}\cdot\mathbf{n}\mathrm{d}S = -\iiint \dot{m}'''_{gen}\mathrm{d}V \tag{3.4}$$

$$\frac{\mathrm{d}}{\mathrm{d}t}\iiint \epsilon\rho_{pg} \mathrm{d}V + \iint \epsilon\rho_{pg}\mathbf{u_{pg}}\cdot\mathbf{n}\mathrm{d}S - \iint \epsilon\rho_{pg}\mathbf{u_{cs}}\cdot\mathbf{n}\mathrm{d}S = \iiint \dot{m}'''_{gen}\mathrm{d}V \tag{3.5}$$

The mixture energy equation in integral form becomes:

$$\begin{aligned}\underbrace{\frac{\mathrm{d}}{\mathrm{d}t}\iiint \rho e \mathrm{d}V}_{\text{energy storage}} + \underbrace{\iint \dot{\mathbf{q}}''_{\mathbf{cond}}\cdot\mathbf{n}\mathrm{d}S}_{\text{conduction}} + \underbrace{\iint \epsilon\rho_{pg}h_{pg}\mathbf{u_{pg}}\cdot\mathbf{n}\mathrm{d}S}_{\text{gas flow}} \\ - \underbrace{\iint \rho h\mathbf{u_{cs}}\cdot\mathbf{n}\mathrm{d}S}_{\text{grid convection}} = 0\end{aligned} \tag{3.6}$$

which is sum of the solid and gas phase energy equations given in Eq. 3.7 and Eq. 3.8, respectively.

$$\frac{\mathrm{d}}{\mathrm{d}t}\iiint \rho_s e_s \mathrm{d}V + \iint \dot{\mathbf{q}}''_{\mathbf{cond_s}}\cdot\mathbf{n}\mathrm{d}S - \iint \rho_s h_s\mathbf{u_{cs}}\cdot\mathbf{n}\mathrm{d}S = 0 \tag{3.7}$$

$$\begin{aligned}\frac{\mathrm{d}}{\mathrm{d}t}\iiint \epsilon\rho_{pg}e_{pg} \mathrm{d}V + \iint \dot{\mathbf{q}}''_{\mathbf{cond_{pg}}}\cdot\mathbf{n}\mathrm{d}S + \iint \epsilon\rho_{pg}h_{pg}\mathbf{u_{pg}}\cdot\mathbf{n}\mathrm{d}S \\ - \iint \epsilon\rho_{pg}h_{pg}\mathbf{u_{cs}}\cdot\mathbf{n}\mathrm{d}S = 0\end{aligned} \tag{3.8}$$

The velocity of a control surface can be obtained as a function of surface recession rate, $\dot{s}$, by differentiating Eq. 3.1 with respect to time. Time derivative of Eq. 3.1 results in:

$$\frac{\mathrm{d}}{\mathrm{d}t}(L_o - z) = \frac{\mathrm{d}}{\mathrm{d}t}(\eta(L_o - s)) \implies \dot{z} = \eta\dot{s} \tag{3.9}$$

where $\dot{z}$ is velocity of grid node. Since control volume boundaries are always at the mid-points of the nodes in vertex-centered scheme, velocity of a control volume between the nodes j and $j+1$ can be written as:

$$(u_{cs})_{j+1/2} = 0.5(\dot{z}_j + \dot{z}_{j+1}) = 0.5\dot{s}(\eta_j + \eta_{j+1}) \tag{3.10}$$

3.1.4 Formulation of Governing Equations

Mixture energy equation and gas phase continuity equations require an iterative solution due to non-linearity. Newton's linearization method presented in Appendix A is employed for the iterative solution of the nonlinear equations. As opposed, the solid continuity equation is solved through direct integration of the pyrolysis kinetics equations as described below.

3.1.4.1 Solid Continuity Equation

The solid phase continuity equation describes the thermal decomposition of the charring ablative material, i.e. the pyrolysis process, and is given in Eq. 3.4. The grid convection term in Eq. 3.4 makes the solution of the solid phase continuity equation quite complex [62]. Thus, an alternative approach [13,20] is adopted. In this approach, first a fixed material element is considered in the domain, and then the moving grid effect is incorporated to the solution. Details of the procedure are explained as follows.

The solid phase continuity equation without the convective term is:

$$\frac{\mathrm{d}}{\mathrm{d}t}\iiint \rho_s \mathrm{d}V = -\iiint \dot{m}'''_{gen}\mathrm{d}V \tag{3.11}$$

Substituting Eq. 2.4 into Eq. 3.11 and assuming that the component mass source terms

can be weighted like the component densities yields:

$$\begin{aligned} &\frac{\mathrm{d}}{\mathrm{d}t}\iiint [\Gamma(\rho_A+\rho_B)+(1-\Gamma)\rho_C]\mathrm{d}V \\ &=\iiint [\Gamma(\dot{m}_A'''+\dot{m}_B''')+(1-\Gamma)\dot{m}_C''']\mathrm{d}V \end{aligned} \tag{3.12}$$

Eq. 3.12 can be split into single component continuity equations if the decomposition of the components is assumed to be independent of each other as:

$$\frac{\mathrm{d}}{\mathrm{d}t}\iiint \rho_i \mathrm{d}V = \iiint \dot{m}_i''' \mathrm{d}V, \quad i=A,B,C \tag{3.13}$$

By knowing that the pyrolysis process is modeled in Arrhenius form, Eq. 3.13 can be written as:

$$\frac{\mathrm{d}\rho_i}{\mathrm{d}t} = \dot{m}_i''' = -Z_i\rho_{v,i}\left(\frac{\rho_i-\rho_{ch,i}}{\rho_{v,i}}\right)^{\psi_i} e^{-E_{a,i}/(R_uT)}, \quad i=A,B,C \tag{3.14}$$

Since $\rho_{ch,i}$ and $\rho_{v,i}$ are constant, Eq. 3.14 can be expressed as:

$$\frac{\mathrm{d}\xi_i}{\mathrm{d}t} = \dot{m}_i''' = -Z_i\rho_{v,i}\xi_i^{\psi_i} e^{-E_{a,i}/(R_uT)}, \quad i=A,B,C \tag{3.15}$$

where the dimensionless relative density, ξ, is:

$$\xi_i = \frac{\rho_i-\rho_{ch,i}}{\rho_{v,i}}, \quad i=A,B,C \tag{3.16}$$

Thus, for each grid point in the solution domain three ordinary differential equations are obtained. These ordinary differential equations can be integrated directly on a point-by-point basis assuming a linear temperature change over a time step of Δt. Thus, density history at a given location can be established using the temperature history at that location. Integration of Eq. 3.16 implicitly from time t^n to time t^{n+1} at the grid point z_j yields:

$$\xi_i(z_j,t^{n+1}) = \left\{[\xi_i(z_j,t^n)]^{1-\psi_i} + \frac{Z_i(\psi_i-1)\Delta t}{T(z_j,t^{n+1})-T(z_j,t^n)}\int_{T(z_j,t^n)}^{T(z_j,t^{n+1})} e^{-\frac{E_{a,i}}{RT}}\mathrm{d}T\right\}^{-\frac{1}{\psi_i-1}},$$
$$i=A,B,C \quad \text{for} \quad \psi\neq 1 \tag{3.17}$$

and

$$\ln[\xi_i(z_j,t^{n+1})] = \ln[\xi_i(z_j,t^n)] - \frac{Z_i\Delta t}{T(z_j,t^{n+1})-T(z_j,t^n)}\int_{T(z_j,t^n)}^{T(z_j,t^{n+1})} e^{-\frac{E_{a,i}}{RT}}\mathrm{d}T,$$
$$i=A,B,C \quad \text{for} \quad \psi=1 \tag{3.18}$$

where $\Delta t = t^{n+1} - t^n$. The integral term in Eqs. 3.17 and 3.18 is evaluated using Simpson's 1/3 rule.

The component densities can be determined using Eq. 3.16 once dimensionless relative densities are evaluated using Eq. 3.17 or Eq. 3.18. The solid density can then be calculated in terms of component densities using Eq. 2.4. In order to incorporate the influences of grid translation, at each time step the solution from the previous grid points is mapped on to the new grid points. In this sense, this approach is actually not a front-fixing method but a front-tracking scheme.

3.1.4.2 Gas Continuity Equation

The gas mass conservation equation given in Eq. 3.5 defines the flow of the pyrolysis gas mixture through the porous ablative material. Figure 3.5 demonstrates the gas mass balance terms in semi-discrete form for a one-dimensional control volume. The mass balance can be expressed as:

$$\frac{\mathrm{d}}{\mathrm{d}t}\int_{\bar{z}_{j-1}}^{z_j} \epsilon\rho_{pg} S \mathrm{d}z + \frac{\mathrm{d}}{\mathrm{d}t}\int_{z_j}^{\bar{z}_j} \epsilon\rho_{pg} S \mathrm{d}z - \int_{\bar{z}_{j-1}}^{z_j} \dot{m}'''_{gen} S \mathrm{d}z - \int_{z_j}^{\bar{z}_j} \dot{m}'''_{gen} S \mathrm{d}z$$
$$+(\epsilon\rho_{pg}u_{pg}S)_{j+1/2} - (\epsilon\rho_{pg}u_{pg}S)_{j-1/2} - (\epsilon\rho_{pg}u_{cs}S)_{j+1/2} + (\epsilon\rho_{pg}u_{cs}S)_{j-1/2} = 0 \tag{3.19}$$

where $\bar{z}_j = 0.5(z_{j+1} + z_j)$.

The convective terms, both grid convection and gas convection, are discretized using first-order upwind scheme. The gas source term is calculated from the change of the solid density as:

$$\dot{m}'''_{gen} = \frac{\rho_s^n - \rho_s^{n+1}}{\Delta t} \tag{3.20}$$

The gas phase continuity equation requires an iterative solution since the pyrolysis gas velocity, u_{pg}, is a solution variable along with the gas density. Nodal values of solid and gas temperatures as well as solid density are kept constant during iterative solution. Each term in Eq. 3.19 is linearized using Newton's method. The first-order implicit Euler method is used for time integration. The resulting linear system is of

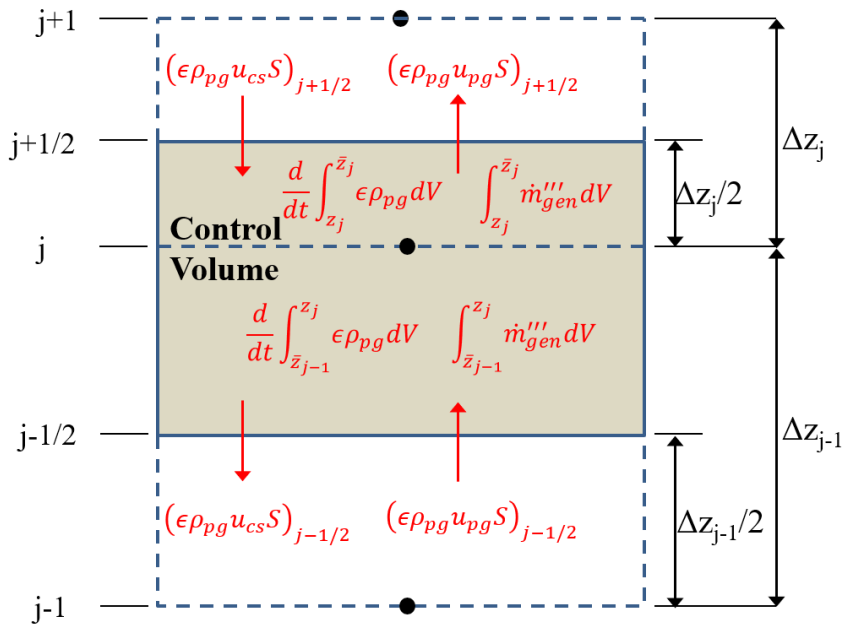


Figure 3.5: Control volume for solution of gas phase continuity equation

the form:

$$\begin{bmatrix} b_1 & c_1 & & & & & \\ a_2 & b_2 & c_2 & & & & \\ & a_3 & b_3 & c_3 & & & \\ & & . & . & . & & \\ & & & . & . & . & \\ & & & & . & . & . \\ & & & & & a_{n-1} & b_{n-1} & c_{n-1} \\ & & & & & & a_n & b_n \end{bmatrix} \begin{bmatrix} \Delta(\rho_{pg})_1 \\ \Delta(\rho_{pg})_2 \\ \Delta(\rho_{pg})_3 \\ . \\ . \\ . \\ \Delta(\rho_{pg})_{n-1} \\ \Delta(\rho_{pg})_n \end{bmatrix} = \begin{bmatrix} f_1 \\ f_2 \\ f_3 \\ . \\ . \\ . \\ f_{n-1} \\ f_n \end{bmatrix} \tag{3.21}$$

where the subscript n denotes the number of nodes.

The sensitivity matrix of the gas phase continuity equation is always tri-diagonal and solved using Thomas algorithm [63]. The pyrolysis gas density field is updated after each iteration, v, as:

$$\rho_{\mathbf{pg}}{}^{v+1} = \rho_{\mathbf{pg}}{}^{v} + \boldsymbol{\Delta}\rho_{\mathbf{pg}} \tag{3.22}$$

This iteration is performed until the maximum pyrolysis gas density update, $max(\boldsymbol{\Delta}\rho_{\mathbf{pg}})$, falls below a threshold value of $10^{-5}\,\mathrm{kg/m^3}$.

3.1.4.3 Mixture Energy Equation

The mixture energy equation given in Eq. 3.6 defines the energy flow through the porous ablative material by means of diffusion and advection. Figure 3.6 demonstrates the energy balance terms in semi-discrete form for a one-dimensional control volume. The energy balance for a control volume can be expressed as:

$$\frac{\mathrm{d}}{\mathrm{d}t}\int_{\bar{z}_{j-1}}^{z_j}\rho e S\mathrm{d}z+\frac{\mathrm{d}}{\mathrm{d}t}\int_{z_j}^{\bar{z}_j}\rho e S\mathrm{d}z+(\dot{q}''_{cond}S)_{j+1/2}-(\dot{q}''_{cond}S)_{j-1/2}$$
$$+(\epsilon\rho_{pg}h_{pg}u_{pg}S)_{j+1/2}-(\epsilon\rho_{pg}h_{pg}u_{pg}S)_{j-1/2}-(\rho hu_{cs}S)_{j+1/2}+(\rho hu_{cs}S)_{j-1/2}=0 \tag{3.23}$$

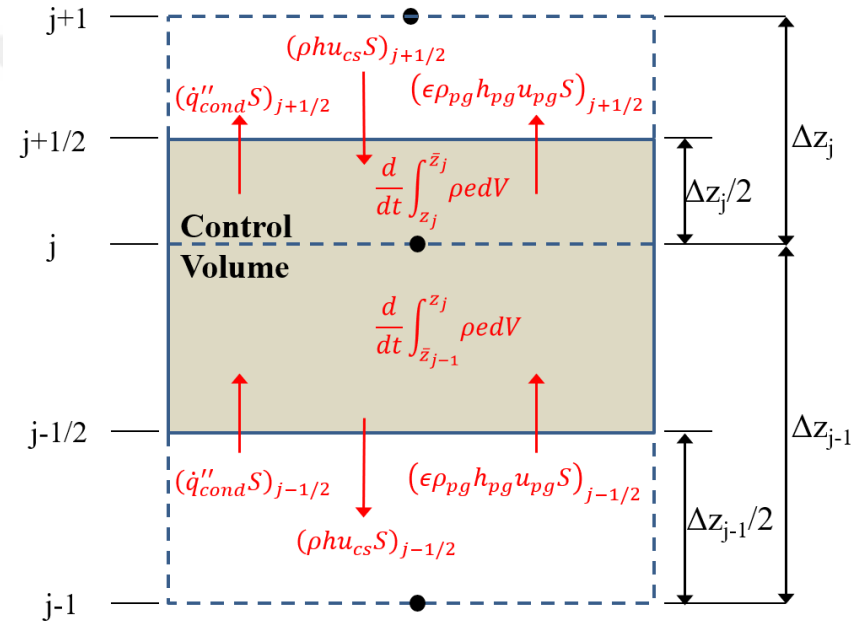


Figure 3.6: Control volume for solution of mixture energy equation

The convective terms, both grid convection and gas convection, are discretized using first-order upwind scheme. The diffusive terms are discretized using central differencing scheme. Nodal temperatures and surface recession rate are the solution variables whereas solid density, gas density, and gas velocity are kept constant. The backward Euler method is employed for the time integration in a similar fashion to the solution of the gas phase continuity equation. Solution of the mixture energy equation requires an iterative technique due to temperature dependent material properties and the coupling between the surface conditions and internal temperature field. Newton's

method is applied to linearize the terms of the mixture energy equation. The resulting linear system is of the form:

$$\begin{bmatrix} e_0 & c_0 & & & & & & & \\ e_1 & b_1 & c_1 & & & & & & \\ e_2 & a_2 & b_2 & c_2 & & & & & \\ e_3 & & a_3 & b_3 & c_3 & & & & \\ . & & & . & . & . & & & \\ . & & & & . & . & . & & \\ . & & & & & . & . & . & \\ e_{n-1} & & & & & & a_{n-1} & b_{n-1} & c_{n-1} \\ e_n & & & & & & & a_n & b_n \end{bmatrix} \begin{bmatrix} \Delta\dot{s} \\ \Delta T_1 \\ \Delta T_2 \\ \Delta T_3 \\ . \\ . \\ . \\ \Delta T_{n-1} \\ \Delta T_n \end{bmatrix} = \begin{bmatrix} f_0 \\ f_1 \\ f_2 \\ f_3 \\ . \\ . \\ . \\ f_{n-1} \\ f_n \end{bmatrix} \tag{3.24}$$

The linear system given in Eq. 3.24 is solved in two steps. First, the sensitivity matrix is modified to a lower triangular structure using Gauss elimination method. Then, the modified linear system is solved using back-substitution method. The sensitivity matrix of the mixture energy equation becomes tri-diagonal only if the surface recession is not taken into account. In this case, the Thomas algorithm is employed to solve the linear system.

The temperature field and the surface recession rate are updated after each iteration, v, as:

$$\mathbf{T}^{v+1} = \mathbf{T}^{v} + \mathbf{\Delta T} \tag{3.25}$$

$$\dot{\mathbf{s}}^{v+1} = \dot{\mathbf{s}}^{v} + \mathbf{\Delta \dot{s}} \tag{3.26}$$

This iteration is performed until the maximum temperature update, $max(\mathbf{\Delta T})$, falls below a threshold value of $10^{-10}\,\mathrm{K}$.

3.1.4.4 Boundary Conditions

As described in Chapter 2, in thermo-chemical ablation model the surface energy balance yields:

$$\dot{q}^{''}_{cond} = \rho_e u_e C^{'}_h[(h_r - h_w) - B^{'} h_w + B^{'}_{ch} h_{ch} + B^{'}_{pg} h_{pg}] + \dot{q}^{''}_{rad-in} - \dot{q}^{''}_{rad-out} \tag{3.27}$$

The closure of the mixture energy equation is achieved with Eq. 3.27. However, the only explicitly specified variable in Eq. 3.27 is h_r. All other variables except radiation terms are functions of surface temperature, pressure and solid and gas mass fluxes which are solution variables, too. The radiation terms are functions of surface temperature only. Therefore, consistent values of h_w, $B_{ch}^{'}$, $B_{pg}^{'}$ and $B^{'}$ in Eq. 3.27 are obtained through the iterative solution of the mixture energy equation. In other words, the heat flux at the surface and the conduction into the material are brought into agreement through an iterative method used to solve the mixture energy equation.

One important point to emphasize is that the total pyrolysis gas injection into the boundary layer is a combination of both gas flow and surface recession as:

$$\dot{m}_{pg}|_{x=0} = \iint \epsilon \rho_{pg} \mathbf{u_{pg}} \cdot \mathbf{n} \mathrm{d}S + \iint \epsilon \rho_{pg} \dot{s} \mathrm{d}S \tag{3.28}$$

The surface recession rate, also, determines the solid mass flux in to the boundary layer as:

$$\dot{s} = \frac{\dot{m}_{ch}^{''}}{\rho_s} = \frac{B_{ch}^{'} \rho_e u_e C_h^{'}}{\rho_{ch}} \tag{3.29}$$

Therefore, the non-dimensional pyrolysis mass flux, $B_{pg}^{'}$, is not independent of non-dimensional char mass flux, $B_{ch}^{'}$. This dependency further complicates the iterative solution process. Using a chemical equilibrium solver, h_w, $B_{ch}^{'}$, and $B_{pg}^{'}$ can be computed and tabulated in advance as a function of surface temperature and pressure. This subject is elaborated in Chapter 4. For the time being, it is sufficient to state that during iterative solution of the mixture energy equation, consistent values are obtained during iterative solution through interpolation from tabulated data.

Apart from the thermo-chemical ablation boundary condition, various time-dependent boundary conditions for the mixture energy equation are implemented. For the front (ablating) surface these are:

- Specified temperature
- Specified heat flux
- Convection with and without thermal radiation

Two time dependent boundary conditions are implemented for the back (stationary) surface:

- Specified temperature
- Convection

In order to solve the gas phase continuity equation, time dependent pressure at the front surface must also be specified. The back surface is assumed to be impermeable.

3.1.4.5 Non-planar Geometries

There exist a few differences in the numerical implementation between the planar and non-planar, i.e. axisymmetric cylindrical and spherical, geometries. First, the Landau transformation has to be modified for axisymmetric geometries. Figure 3.7 shows the spatial coordinate and Landau coordinate for axisymmetric geometries. The Landau coordinate is expressed as:

$$\eta = \frac{L_o - z}{L_o - s(t)} = \frac{r - R_o + L_o}{L(t)} \quad \text{as } z = R_o - r \tag{3.30}$$

where R_o is the initial outer radius. Thus, in addition to initial length, L_o, the initial outer radius is required to calculate the Landau coordinate for axisymmetric geometries.

The surface area, S, in the terms can be omitted and the thickness of a control volume, i.e. element, can be taken as the volume of the element for planar geometries. These simplifications become invalid in axisymmetric geometries since the area and also the volume of an element are functions of position: $S = S(r)$ and $V = V(r)$. The area variation can be expressed as:

$$S(r) = 2m\pi r^m \tag{3.31}$$

where m is equal to 1 and 2 for cylindrical and spherical geometries, respectively. The volume of an element is:

$$V_j(r) = \frac{2m\pi}{m+1}(r_{j+1/2}^{m+1} - r_{j-1/2}^{m+1}) \tag{3.32}$$

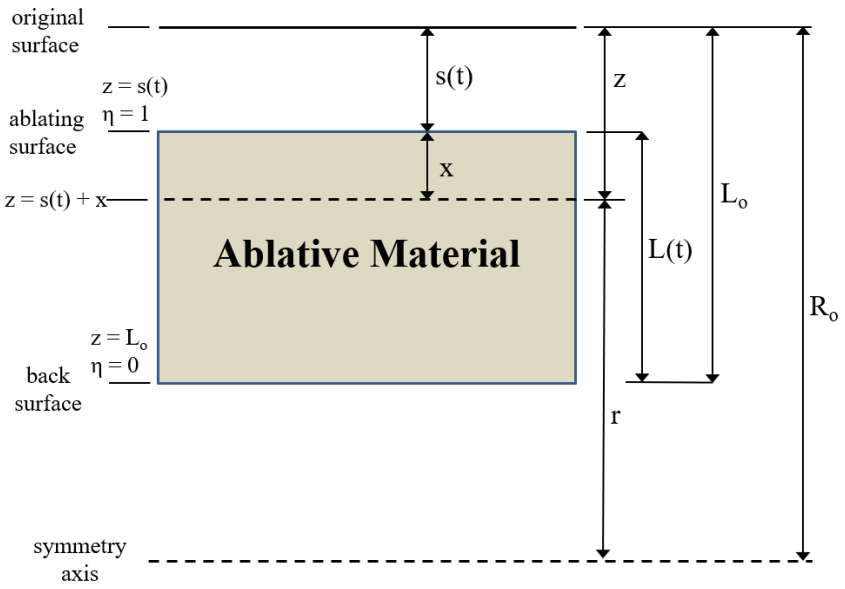


Figure 3.7: Landau parameters for axisymmetric geometries

The variation of area and element volume with position introduces new terms into the surface recession rate sensitivities. It would be cumbersome to compare all differences in the sensitivity matrix, so only an illustrative example is given.

The heat conduction at a control volume boundary is discretized as:

$$\dot{q} = (\dot{q}''_{cond} S)_{j+1/2} = \left[-kS \frac{\partial T}{\partial z} \right]_{j+1/2} = -\frac{\bar{k}\bar{S}}{\Delta z_j}(T_{j+1} - T_j) \tag{3.33}$$

where for any variable of X, $\bar{X} = 0.5(X_{j+1} + X_j)$.

For planar geometries, the surface area is constant and independent of location, i.e. of surface recession rate consequently. Then, the surface recession rate sensitivity of heat conduction term for planar geometries is:

$$\frac{\partial \dot{q}_{planar}}{\partial \dot{s}} = -\bar{k}(T_{j+1} - T_j) \frac{\partial}{\partial \dot{s}} \left(\frac{1}{\Delta z_j} \right) = \bar{k}(T_{j+1} - T_j) \frac{\Delta t(\eta_{j+1} - \eta_j)}{\Delta z_j^2} \tag{3.34}$$

For cylindrical and spherical geometries, the surface area is a function of position. As a result, the surface recession rate, $\dot{s}$, has an effect on the area change at any location. Then, the sensitivities with respect to the surface recession rate for cylindrical and

spherical geometries become, respectively, as:

$$\frac{\partial \dot{q}_{cylindrical}}{\partial \dot{s}} = 2\pi \frac{\bar{k}}{\Delta z_j}(T_{j+1} - T_j)\Delta t \left[\frac{R_o - \bar{z_j}}{\Delta z_j}(\eta_{j+1} - \eta_j) + \bar{\eta_j}\right] \tag{3.35}$$

$$\frac{\partial \dot{q}_{spherical}}{\partial \dot{s}} = 4\pi \frac{\bar{k}}{\Delta z_j}(T_{j+1} - T_j)\Delta t(R_o - \bar{z_j}) \left[\frac{R_o - \bar{z_j}}{\Delta z_j}(\eta_{j+1} - \eta_j) + 2\bar{\eta_j}\right] \tag{3.36}$$

3.1.5 Material Modeling

Let X_s be a generic property of the intermediate solid phase, i.e. neither virgin nor fully charred, and X_v and X_{ch} are the values of that property known for the virgin and the fully charred states. Then, at any point the value of X is calculated as:

$$X_s = y_v X_v + y_{ch} X_{ch} \tag{3.37}$$

where y_v and y_{ch} are virgin and char mass fractions, respectively. y_v and y_{ch} are expressed in terms of extent-of-reaction as:

$$y_v = \frac{\rho_v}{\rho_v - \rho_{ch}}\left(1 - \frac{\rho_{ch}}{\rho_s}\right) = \frac{\rho_v}{\rho_s}(1 - \alpha) \tag{3.38}$$

$$y_{ch} = 1 - y_v = \frac{\rho_{ch}}{\rho_s}\alpha \tag{3.39}$$

However, the permeability of the solid material is excluded because it may change several orders of magnitude between the virgin and fully charred states. In addition, it is reported that the permeability changes logarithmically with respect to extent-of-reaction [64]. Then, the permeability of the intermediate solid is calculated as:

$$log_{10}(\kappa) = (1 - \alpha)log_{10}(\kappa_v) + \alpha log_{10}(\kappa_{ch}) \tag{3.40}$$

The mixture properties are evaluated from the solid and pyrolysis gas properties as a weighted-mass average:

$$X = y_{pg} X_{pg} + (1 - y_{pg}) X_s \tag{3.41}$$

where y_{pg} is the mass fraction of the pyrolysis gases given as:

$$y_{pg} = \frac{\epsilon \rho_{pg}}{\rho} \tag{3.42}$$

Thermodynamic and transport properties of the pyrolysis gas mixture are required for the determination of the mixture properties and for the solution of the governing equations. Evaluation of these properties is addressed in Chapter 4. For the time being, it is assumed that pyrolysis gas mixture properties are tabulated in advance as a function of temperature and pressure. Indeed, it is the usual procedure as long as pyrolysis gases are assumed to be frozen, i.e. having fixed composition, or in chemical equilibrium. Then, during the solution the required values are obtained through linear interpolation from the tabulated data.

3.1.6 Solution Procedure

The mixture energy equation, solid phase continuity equation and gas phase continuity equation are solved one after the other in a loosely-coupled iterative process for each time step. Estimation of gas velocity through Darcy's law eliminates the solution of an independent momentum equation since in conjunction with the perfect gas law the gas velocity becomes an inherent part of the gas phase continuity equation. The solution approach can then be laid down as follows:

- Surface recession rate and nodal temperatures are computed from the mixture energy equation iteratively and the grid is updated at every iteration by using contracting grid scheme. Solid density, gas density, as well as gas velocity are kept constant.

- Nodal solid densities are computed from the solution of solid phase continuity and pyrolysis kinetic equations. The updated temperatures and grid are used.

- Nodal gas densities are computed solving the gas phase continuity equation. Darcy's law is used to determine the pyrolysis gas velocity. The updated temperatures, solid densities and the grid are used.

This sequential (segregated) solution scheme is illustrated in Figure 3.8. The dependent variables for each conservation equation are shown in rectangle boxes.

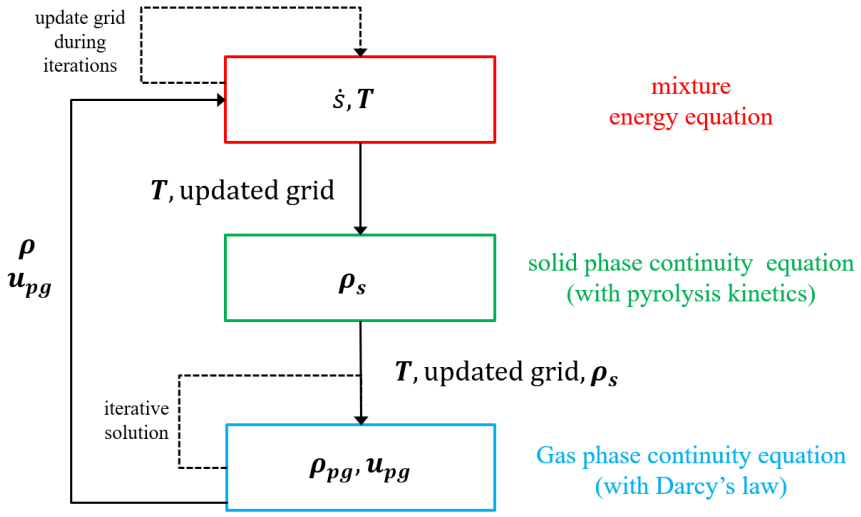


Figure 3.8: Solution procedure

3.2 Verification Studies

This section is devoted to the quantification of the accuracy of the numerical implementation of the governing equations through code verification studies. Code verification studies assure that the solution algorithms are free of errors and inconsistencies. Two approaches are adopted: Method of exact solutions and code-to-code comparison. The method of exact solutions includes the comparison of a numerical solution to an analytical solution of a nontrivial problem with well-posed initial and boundary conditions. The main drawback of this method is that in general no analytical solution is available for complex, multi-physics problems and then the comparison can only be performed for much simpler problems [65]. Thus, the code-to-code comparison method, in which the code output is compared to the solution obtained from other established codes that solve similar problems, is also used for verification studies. In practice, if the difference between the solutions of two codes is smaller than 20%, then the code can be considered serviceable [66].

Systematic grid refinement is the most important activity of verification processes in the context of evaluation of error. Therefore, grid refinement studies are performed in order to observe the convergence of the solutions towards a known solution when an analytical solution is available. In code-to-code comparison studies, instead of

comparing *grid-free* solutions, solutions on a specific grid are compared. That is not only because it is useful and computationally economical [67], but the results of the established codes are mostly taken from the literature obtained using a specific grid.

In grid refinement studies, solutions are obtained on three different uniform grid resolutions named as *fine*, *medium*, and *coarse*. Grids are constructed using a constant grid refinement factor, r, of 2. For each grid level, k, the global discretization error is evaluated employing L_2 norm of error as follows:

$$L_{2,k} = \left(\frac{\sum_{i=1}^{n} |f_{k,i} - f_{exact,i}|^2}{n} \right)^{1/2} \tag{3.43}$$

where n is the number of grid points and f_{exact} comes from the analytical solution. The observed order of accuracy, ς, is then calculated in terms of L_2 as:

$$\varsigma_k = \frac{\ln\left(\frac{L_{2,k+1}}{L_{2,k}}\right)}{\ln(r)} \tag{3.44}$$

In code-to-code comparison, the infinite norm, L_∞, is used for the quantification of error as:

$$L_\infty = max|f_i - f_{exact,i}| \tag{3.45}$$

where f_{exact} comes from the solution of the *benchmark* code. It should be noted that in the context of L_∞ error norm, the index i does not necessarily represent values at grid points. It can stand for the solution values obtained at specified time intervals.

3.2.1 Case 1: Transient Heat Conduction

Transient heat conduction solutions are obtained for two boundary condition pairs. Constant material properties of a typical Titanium alloy, i.e. Ti-6Al-4V, at room temperature are used (Table 3.1). Initial temperature of the material, T_0, and the domain length, L, are set to $300\ K$ and $0.01\ m$, respectively. In the first subcase, convective boundary condition is applied to one surface. The heat transfer coefficient and corresponding temperature, T_∞, are set to $1000\ W/(m^2 \cdot K)$ and $1500\ K$, respectively. In the second subcase, constant heat flux, $\dot{q}''$, of $500\,000\ W/m^2$ is applied to one surface. In both subcases the other surface is assumed to be adiabatic. All simulations

are carried out for $30\ s$ with a constant time step of $0.01\ s$. Grid parameters are given in Table 3.2.

Table 3.1: Properties of Ti-6Al-4V alloy at room temperature [68]

Property	Value
Density, ρ, kg/m^3	4500.0
Specific heat, c_v, $J/(kg \cdot K)$	550.0
Thermal conductivity, k, $W/(m \cdot K)$	7.5

Table 3.2: Grid parameters for transient heat conduction problems

Grid	Number of cells	Cell size, m
fine	40	0.000 25
medium	20	0.0005
coarse	10	0.001

The analytical solutions of these transient heat conduction problems are given in [69, 70]. The analytical solution of the first subcase is expressed as:

$$\frac{T(z,t)-T_\infty}{T_0-T_\infty} = 2\sum_{i=1}^{\infty}\left(\frac{\sin(\lambda_i L)}{\lambda_i L+\sin(\lambda_i L)\cos(\lambda_i L)}\right)e^{-\alpha\lambda_i^2 t}\cos(\lambda_i z) \tag{3.46}$$

where α is the thermal diffusivity and the characteristic values for all $\lambda_i L > 0$ can be found by solving the following transcendental equation:

$$\lambda_i L\sin(\lambda_i L) = Bi\cos(\lambda_i L) \tag{3.47}$$

where $Bi = hL/k$ is the Biot number.

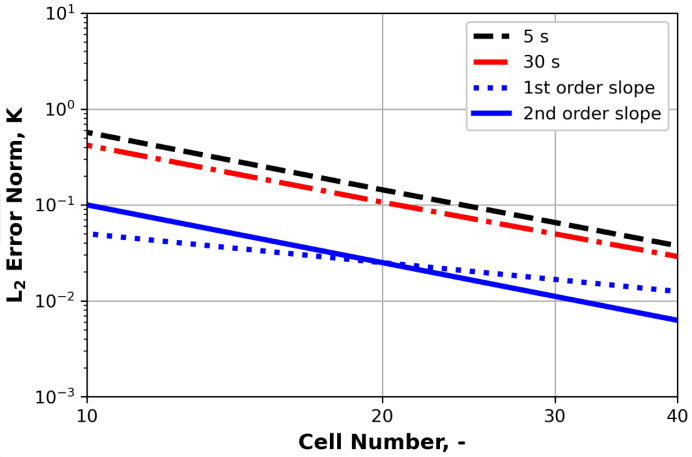
For the second subcase, the analytical solution is given as:

$$\frac{T(z,t)-T_0}{\dot{q}''L/k} = \frac{\alpha t}{L^2} + 0.5\left(\frac{z}{L}\right)^2 - \frac{1}{6} - 2\sum_{i=1}^{\infty}\frac{(-1)^i}{(\lambda_i L)^2}e^{-\alpha\lambda_i^2 t}\cos(\lambda_i z) \tag{3.48}$$

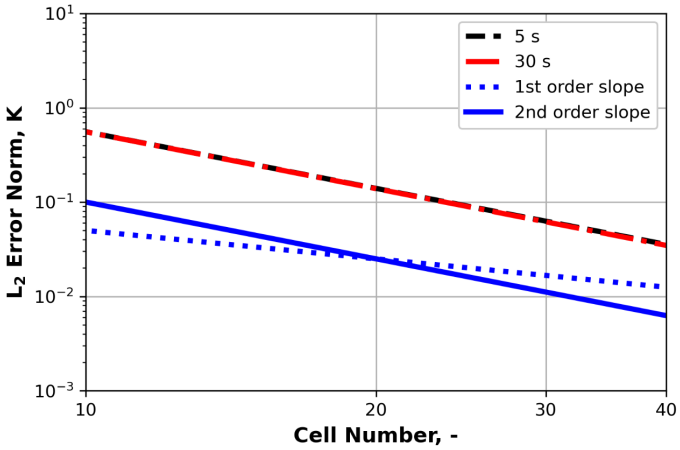
where the characteristic values for all $\lambda_i L > 0$ can be obtained from the following expression:

$$\lambda_i L = \pi i, \quad i = 0, 1, 2, \ldots \tag{3.49}$$

Figure 3.9 shows the evolution of L_2 norm of error as number of grid point changes. Table 3.5 gives the calculated *observed order of accuracy* values. Results demonstrate that solutions for $t = 5\ s$ and $t = 30\ s$ exhibit second-order convergence. Comparison of the code results obtained using *fine* grid with analytical solution is given in Figure 3.10.



(a) Subcase 1

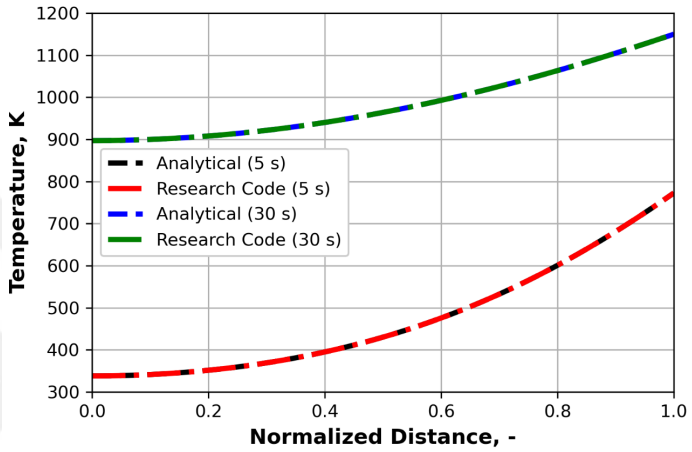


(b) Subcase 2

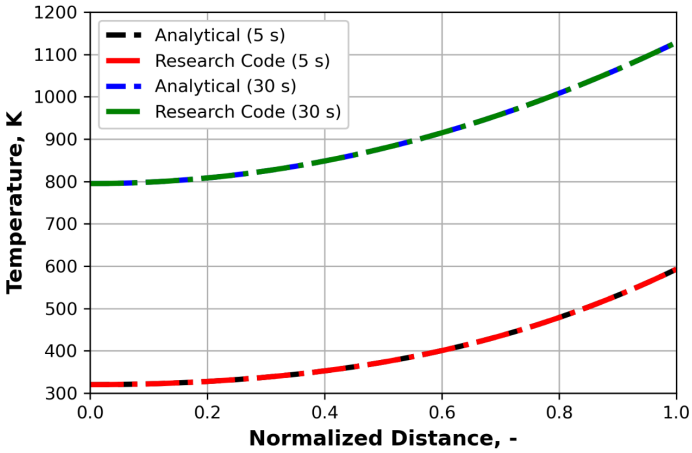
Figure 3.9: Grid convergence of transient heat conduction solutions for $t = 5\ s$ and $t = 30\ s$

Table 3.3: Observed order of accuracy for transient heat conduction problems

Case	t	ς_1	ς_2
Subcase 1	$5\ s$	1.991	1.938
	$30\ s$	1.973	1.883
Subcase 2	$5\ s$	1.996	1.974
	$30\ s$	2.002	1.998



(a) Subcase 1



(b) Subcase 2

Figure 3.10: Comparison of transient heat conduction solutions for $t = 5\ s$ and $t = 30\ s$

3.2.2 Case 2: Transient Heat Conduction with Symmetry Boundary Conditions

In this case, a constant temperature, T_w, boundary condition of $800\ K$ is applied to both surfaces of a $0.02\ m$ slab whose initial temperature is $300\ K$ for $30\ s$. The aim of this symmetry test is to inspect whether the code generates symmetric solution, therefore, no grid convergence study is performed. The solution is obtained using uniform 80 cells with a constant time step of $0.01\ s$. Constant material properties given in Table 3.1 is used. The analytical solution of this problem over a reduced (half) domain, $0 \leq z \leq 0.01$, is given as [70]:

$$\frac{T(z,t) - T_w}{T_0 - T_w} = 2\sum_{i=0}^{\infty} \frac{(-1)^i}{\lambda_i L} e^{-\alpha\lambda_i^2 t} \cos(\lambda_i z) \tag{3.50}$$

where the characteristic values, λ_i, are given for all $\lambda_i L > 0$ as:

$$\lambda_i L = 0.5\pi(2i+1), \quad i = 0, 1, 2, \ldots \tag{3.51}$$

Figure 3.11 presents the code result along with the analytical solution. It is apparent that the research code generates symmetric solution. L_2 error norms at $t = 5\ s$ and $t = 30\ s$ are $0.0085\ K$ and $0.0030\ K$, respectively.

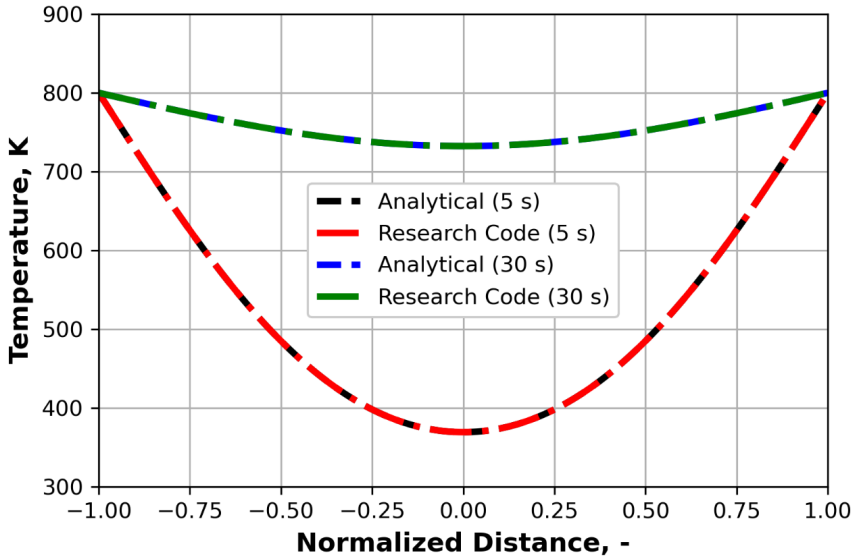


Figure 3.11: Comparison of symmetric transient heat conduction solution for $t = 5\ s$ and $t = 30\ s$

3.2.3 Case 3: Steady-State Radiation

The purpose of this test is to check the proper implementation of surface radiation boundary condition. Radiative boundary condition is applied to one surface of a $0.01\ m$ long domain. Emissivity of the surface, ε, is assumed to be 0.8. The corresponding ambient temperature, T_∞, is $1500\ K$. The other surface of the domain is kept at constant temperature, T_{back}, of $300\ K$. At steady-state, the heat flux conducted into the material has to be equal to the heat flux radiated. This condition can be mathematically expressed as:

$$\varepsilon\sigma(T_\infty^4 - T_w^4) = \frac{k}{L}(T_w - T_{back}) \tag{3.52}$$

where σ is the Stefan-Boltzmann constant ($\sigma = 5.670\,51 \times 10^{-8}\ W/(m^2 \cdot K^4)$)

Iterative solution of Eq. 3.52 with $k = 7.5\ W/(m \cdot K)$ gives the surface temperature as:

$$T_w = 598.45\ K \tag{3.53}$$

The grid converge study is not necessary for this problem since temperature variation through the domain is expected to be linear and therefore solution is independent of element size. The research code yields exactly the same result using arbitrarily selected 20 cells.

3.2.4 Case 4: Transient Heat Conduction with Temperature Dependent Material Properties

This test case is performed to investigate the capability of the research code to handle problems with variable material properties. The test case with constant heat flux boundary condition described in section 3.2.1 is considered. However, in this case the thermal conductivity of the material is assumed to be a linear function of temperature as shown in Table 3.4. If one assumes that thermal diffusivity is constant, an analytical solution can be derived using *Kirchhoff* transformation. Thus, the specific heat is also changed accordingly. Density of the material is set to $5000.0\ kg/m^3$.

Kirchhoff transformation introduces a new temperature, θ, related to the original tem-

Table 3.4: Temperature dependent material properties

Temperature, K	$k, W/(m \cdot K)$	$c_v, J/(kg \cdot K)$
250	5.0	500.0
1250	25.0	2500.0

perature, T, of the problem as [69]:

$$\theta = \frac{1}{k_{ref}} \int_{T_{ref}}^{T} k(T) \mathrm{d}T \tag{3.54}$$

where the subscript ref denotes the convenient reference values. The newly introduced temperature variable removes the non-linearity of the problem and the analytical solution becomes in the same form of the solution obtained assuming constant properties as:

$$\frac{\theta(z,t) - \theta_0}{\dot{q}'' L / k_{ref}} = \frac{\alpha t}{L^2} + 0.5 \left(\frac{z}{L}\right)^2 - \frac{1}{6} - 2 \sum_{i=1}^{\infty} \frac{(-1)^i}{(\lambda_i L)^2} e^{-\alpha \lambda_i^2 t} \cos(\lambda_i z) \tag{3.55}$$

where the characteristic values for all $\lambda_i L > 0$ can be obtained from the following expression:

$$\lambda_i L = \pi i, \quad i = 0, 1, 2, \ldots \tag{3.56}$$

One drawback of this method is that the inverse transformation to the original temperature requires solution of an implicit relationship unless dependence of the thermal conductivity on temperature is exponential [71]. Temperature dependency of thermal conductivity can be expressed mathematically as:

$$k(T) = k_{ref}[1 + \beta_k (T - T_{ref})] \tag{3.57}$$

where β_k is the constant slope. Substitution of Eq. 3.57 into Eq. 3.54 yields:

$$\theta = (T - T_{ref}) + 0.5 \beta_k (T - T_{ref})^2 \tag{3.58}$$

and the inverse transformation can then be obtained by solving the following quadratic equation:

$$(T - T_{ref})^2 + \frac{2}{\beta_k}(T - T_{ref}) - \frac{2}{\beta_k}\theta = 0 \tag{3.59}$$

Figure 3.12 shows the evolution of L_2 norm of error as number of grid point changes (see Table 3.2). Table 3.5 gives the calculated *observed order of accuracy* values. Results demonstrate that solutions for $t = 5\ s$ and $t = 30\ s$ exhibit second-order convergence. Comparison of the code results obtained using *fine* grid with analytical solution is given in Figure 3.13.

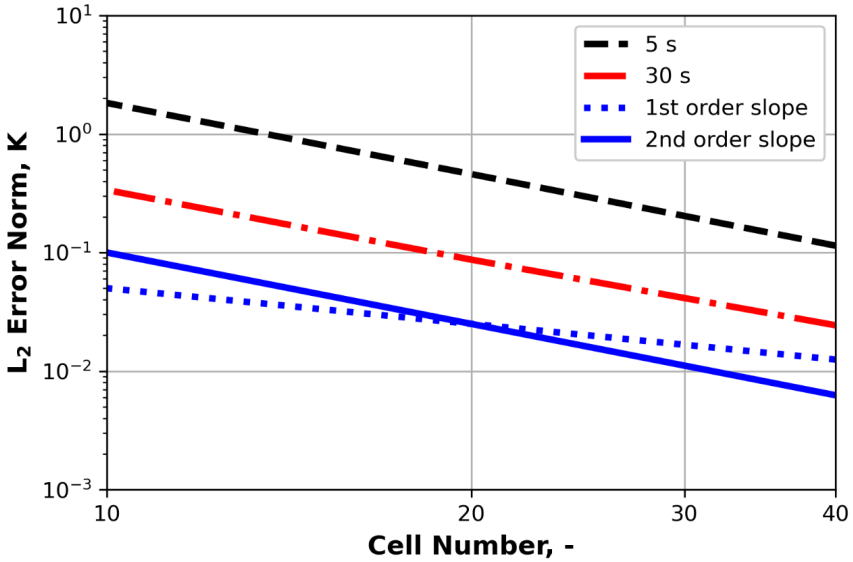


Figure 3.12: Grid convergence of transient heat conduction solution with temperature dependent material properties for $t = 5\ s$ and $t = 30\ s$

Table 3.5: Observed order of accuracy for transient heat conduction problems

t	ς_1	ς_2
$5\ s$	2.007	1.950
$30\ s$	1.993	1.840

It may be worth noting that linear dependence of specific heat at constant volume, c_v, on temperature results in quadratic variation of internal energy, e, with temperature. Variation of specific heat with temperature given in Table 3.4 can be mathematically expressed as:

$$c_v(T) = 2T, \quad 250\ K \leq T \leq 1250\ K \tag{3.60}$$

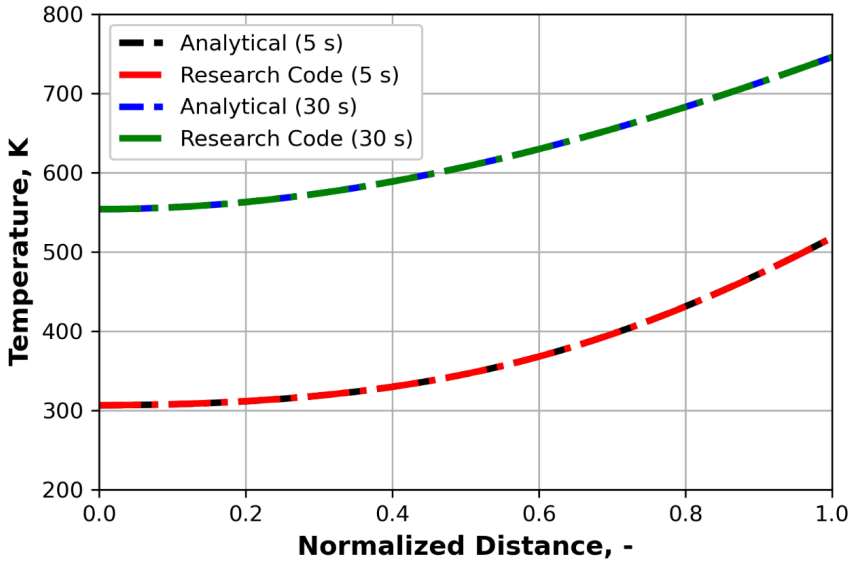


Figure 3.13: Comparison of transient heat conduction solution with temperature dependent material properties for $t = 5\ s$ and $t = 30\ s$

The variation of internal energy can then be formulated as:

$$e(T) = e_{ref} + \int_{T_{ref}}^{T} c_v(T)\mathrm{d}T = \int_{0}^{T} 2T\mathrm{d}T = T^2, \quad 250\,K \leq T \leq 1250\,K \tag{3.61}$$

where the reference values are taken as zero.

The quadratic dependency of internal energy on temperature may degrade the solution and also the grid convergence rate if inconsistent interpolation is applied to obtain the value of the internal energy. For instance, one can compute the internal energy at $750\ K$ as $750\,000\ J/kg$ through linear interpolation between the boundary values instead of the correct value of $e(T = 750) = 562\,500\ J/kg$. Figure 3.14 illustrates the grid convergence degradation due to inconsistent calculation of the internal energy. It is clear that L_2 error norm becomes flat and thus the observed order of accuracy goes to zero as the number of grid point increases.

One remedy for this problem may be to employ parabolic interpolation instead of linear interpolation. Alternatively, linear interpolation with high resolution data points can be used. In this case, the latter is adopted.

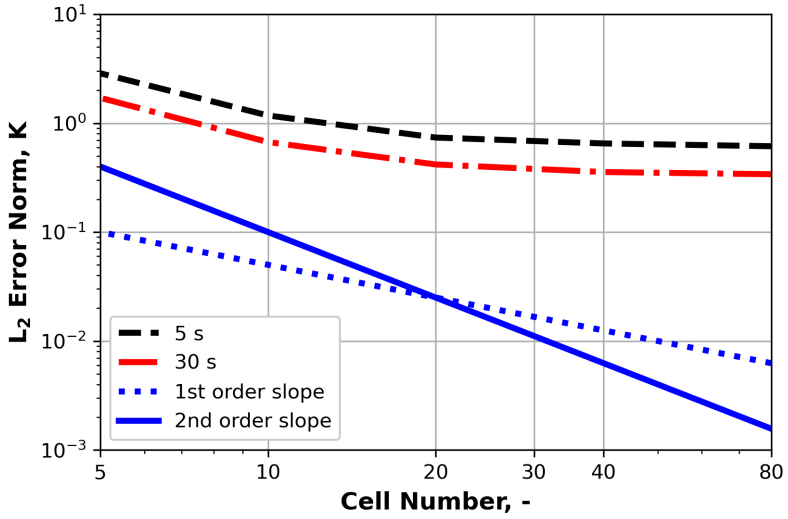


Figure 3.14: Convergence degradation due to inconsistent interpolation

3.2.5 Case 5: Constant Surface Temperature with Prescribed Surface Recession

This test case represents the simplest form of surface ablation problems: sublimation or melting with immediate removal of the melt. A constant surface temperature, T_w, along with constant surface recession rate, $\dot{s}$, is applied to one surface of a sufficiently long domain that ensures semi-infinite behavior. As time progresses, the temperature profile ahead of the moving surface approaches a fixed shape [72], i.e. a quasi-steady profile. There is no expression that estimates the time to reach this quasi-steady profile, t_{ss}. However, a basic dimensional analysis reveals that t_{ss} depends on $\alpha/\dot{s}^2$ ratio. As the surface recession rate increases, t_{ss} decreases and as the thermal diffusivity increases, t_{ss} also increases. For $t > t_{ss}$, the problem can be regarded in steady state condition such that the receding surface is stationary at $z = 0$ and the material moves toward it with speed $\dot{s}$ [73]. The governing equation for this moving medium then becomes:

$$\alpha \frac{\mathrm{d}^2 T}{\mathrm{d}z^2} - \dot{s} \frac{\mathrm{d}T}{\mathrm{d}z} = 0 \tag{3.62}$$

Solution of Eq. 3.62 yields (for $T(z = 0) = T_w$ and $\mathrm{d}T/\mathrm{d}z(z \to \infty) = 0$):

$$T = T_0 + (T_w - T_0) e^{-\dot{s}z/\alpha} \tag{3.63}$$

Constant material properties of polytetrafluoroethylene (PTFE), i.e. teflon, at room temperature given in Table 3.6 are used and uniform initial temperature of $300\ K$ is assumed. Phase transition temperature of Teflon [74] is set as constant surface temperature, i.e. $T_w = 780\ K$. The surface recession rate is assumed to be $\dot{s} = 0.0005\ m$. The initial length of the domain is set to $0.2\ m$ which assures that Fourier number, $Fo = \alpha t/L^2$, is less than $1/12$ for a duration of $340\ s$, i.e. the domain can be assumed to be semi-infinite for a duration of $340\ s$.

Table 3.6: Typical properties of PTFE [74]

Property	Value
Density, ρ, kg/m^3	2200.0
Specific heat, c_v, $J/(kg \cdot K)$	1000.0
Thermal conductivity, k, $W/(m \cdot K)$	0.25

It is expected that very high temperature gradient occurs close to the moving surface. Therefore, it is more appropriate to discretize the domain nun-uniformly. Grid parameters given in Table 3.7 are used to capture the abrupt temperature change in the proximity of the moving surface.

Table 3.7: Grid parameters for moving surface problem

Grid	Number of cells	Cell growth rate
fine	160	1.05
medium	80	1.10
coarse	40	1.20

Figure 3.15 shows the evolution of L_2 norm of error as number of grid point changes. The calculated *observed order of accuracy* values are 1.543 and 1.526, respectively. Results demonstrate that the solution does not exhibit second-order convergence. Indeed, this outcome is anticipated since most of the error contribution comes from the

region where there is no temperature variation. In addition, any kind of moving surface or re-meshing algorithms give rise to noisy or degraded order of accuracy [75]. Comparison of the code results obtained using *fine* grid with analytical solution is given in Figure 3.16.

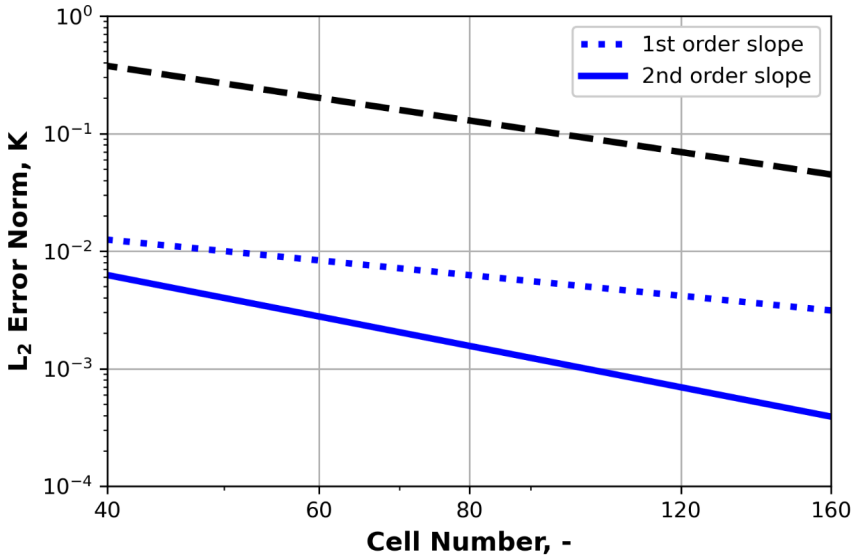


Figure 3.15: Grid convergence of moving surface solution

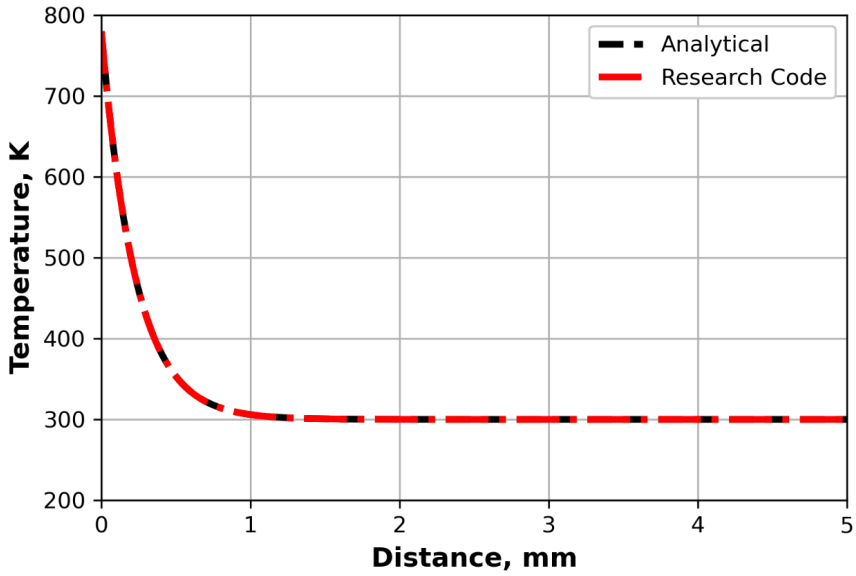


Figure 3.16: Comparison of moving surface solution with analytical result

3.2.6 Case 6: Material Decomposition

This test case is a part of the ablation modeling workshops provided for the purpose of code-to-code comparison [76]. A sample of $0.05\ m$ fictitious Theoretical Ablative Composite for Open Testing (TACOT) material [77], initially at $298\ K$, is heated on one side to $1644\ K$ in $0.1\ s$ which is held constant for $60\ s$ at atmospheric pressure. The other surface is assumed to be adiabatic. Material decomposition, i.e. pyrolysis, takes place during the simulation, however, no surface recession is allowed. Material properties of TACOT material is given in Appendix B.

Unlike the previous verification cases, in this case the domain is assumed to be cylindrical. The initial outer radius of the domain is set to the initial thickness of the sample, i.e. $R_o = L_o = 0.05\ m$. The verification case is illustrated in Figure 3.17. Solution is obtained using 100 elements of equal thickness with constant time step of $0.01\ s$. Temperature variations at pre-determined locations, pyrolysis gas blowing rate, $\dot{m}''_{pg}$, and location of the char and pyrolysis fronts are the solution variables used for comparison. The char and pyrolysis fronts are defined as the depths where 2% and 98% of the material is in its original virgin state, i.e. 98% and 2% charred, respectively. These fronts are denoted as $virgin(2\%)$ and $virgin(98\%)$, respectively. The results are compared with those obtained from the NASA's FIAT code.

Figure 3.18 compares the temperature variations at pre-determined locations with the results of the *benchmark* code. Figure 3.19 presents the results of the research code along with the results of the *benchmark* code for pyrolysis gas blowing rate and char and pyrolysis fronts. Both figures indicate that very good agreement is achieved between the two codes.

Table 3.8 gives the L_∞ error norm of the solution variables, i.e. maximum error throughout the simulation time. The single striking point is that maximum error in pyrolysis gas blowing rate, $\dot{m}''_{pg}$, is 37.8% whereas the error norms of other solution variables are in the range of $1 - 2\%$. There is an abrupt change in the pyrolysis gas blowing rate at the beginning of the analysis due to intense heating. Figure 3.20 shows the variation of $\dot{m}''_{pg}$ in close proximity to time when the maximum error occurs. It can be seen that although the results are very similar in behavior, there exists a small time

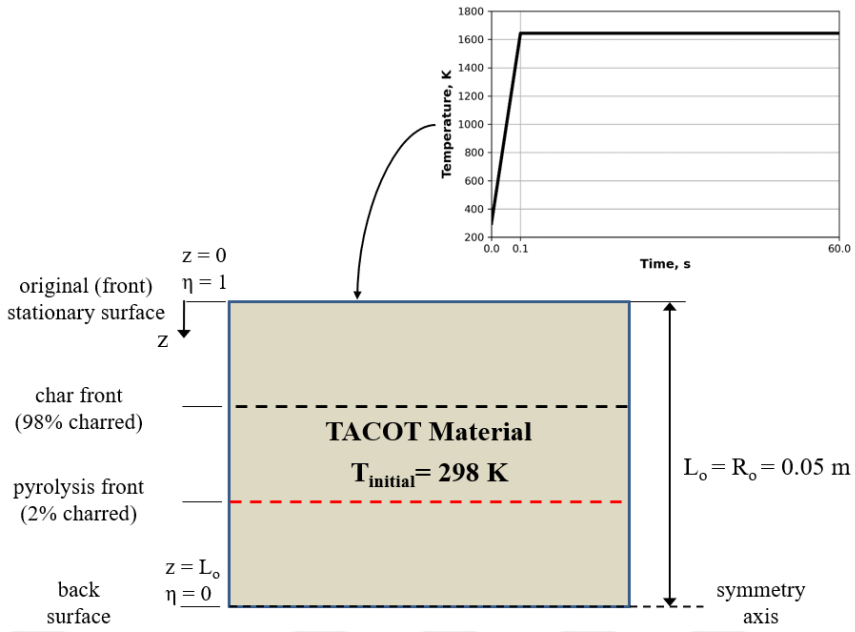


Figure 3.17: Schematic description of verification case 6

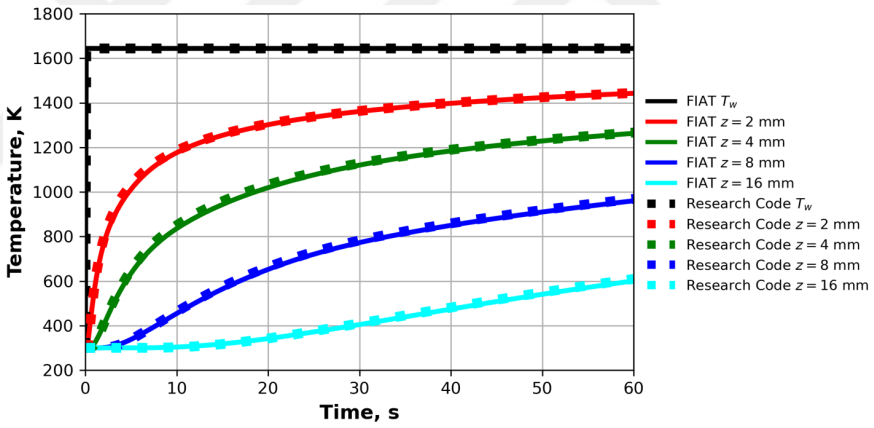


Figure 3.18: Comparison of temperatures at pre-determined locations for verification case 6

offset of $\approx 0.005\ s$. This may stem from the fact that the *benchmark* code assumes that the generated pyrolysis gases are injected into the boundary layer instantaneously, i.e. they do not flow inside the material. Apart from the time between $0.04 - 0.5\ s$, the error varies in the range of $1 - 5\%$. In this view, it is deduced that the maximum error in $\dot{m}''_{pg}$ is not indicative of any deficiencies in the research code and the research code yields proper results.

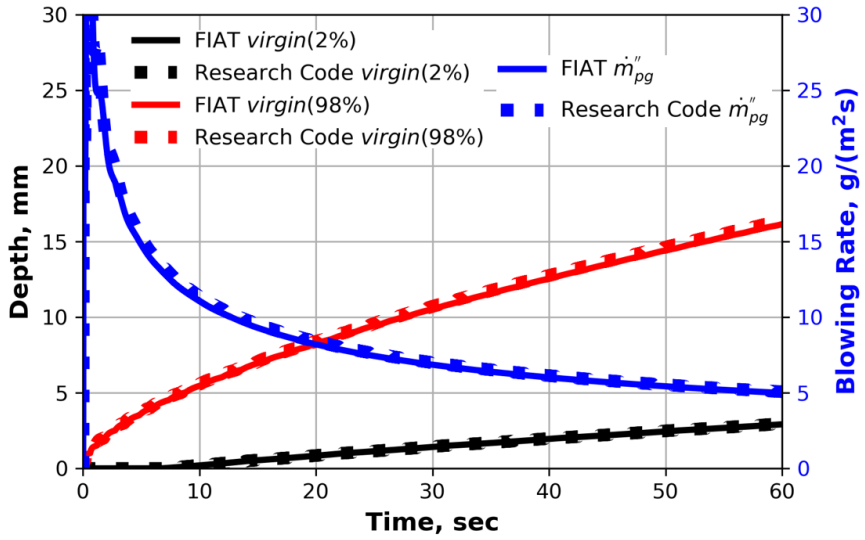


Figure 3.19: Comparison of pyrolysis gas blowing rate and char/pyrolysis fronts for verification case 6

Table 3.8: L_∞ error norms for verification case 6

Error Norm	T_{2mm}	T_{4mm}	T_{8mm}	T_{16mm}	$\dot{m}''_{pg}$	$virgin(2\%)$	$virgin(98\%)$
L_∞, %	2.55	2.05	1.66	1.46	37.8	1.61	1.63

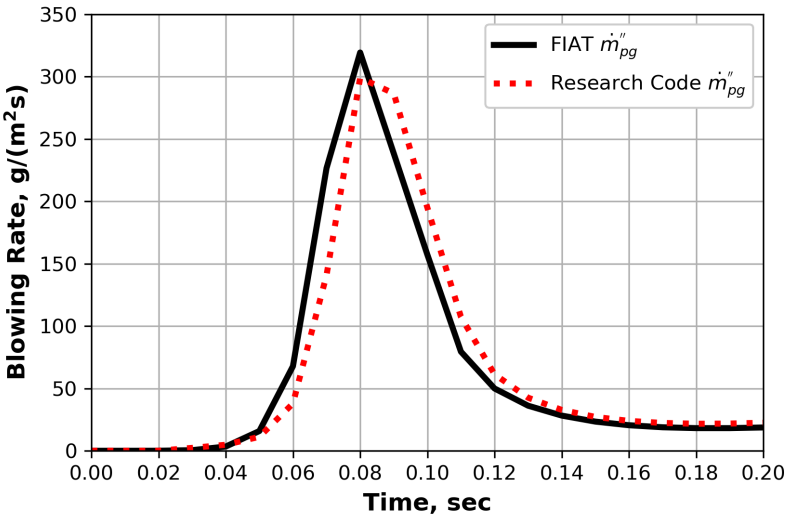


Figure 3.20: Abrupt change in pyrolysis gas blowing rate in verification case 6

3.2.7 Case 7: Material Decomposition with Thermo-chemical Erosion

This test case is also a part of the ablation modeling workshops provided for the purpose of code-to-code comparison [78]. The test case is described as follows. A sample of $0.05\ m$ fictitious TACOT material, initially at $300\ K$, is heated on one side by thermo-chemical convection at atmospheric pressure. The heat transfer coefficient is increased from zero to $0.3\ kg/(m^2 \cdot s)$ at $0.1\ s$, and then held constant for $60\ s$. The corresponding recovery enthalpy is $1.5 \times 10^6\ J/kg$. Adiabatic boundary condition is set on the other (back) surface.

In this case, the domain is assumed to be spherical. The initial outer radius of the domain is set to the initial thickness of the sample, i.e. $R_o = L_o = 0.05\ m$. The verification case is illustrated in Figure 3.21. Solution is obtained using 100 elements of equal thickness with constant time step of $0.01\ s$. Temperature variations at pre-determined locations, pyrolysis gas blowing rate, $\dot{m}''_{pg}$, total surface recession, s, and location of the pyrolysis front, $virgin(98\%)$, are the variables used for comparison. The results are compared with those obtained from the NASA's FIAT code.

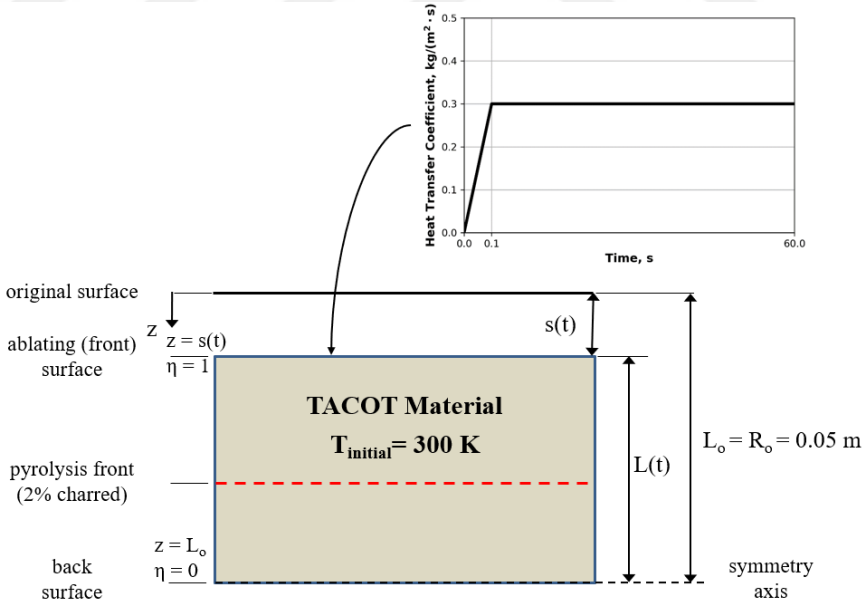


Figure 3.21: Schematic description of verification case 7

Figure 3.22 compares the temperature variations at pre-determined locations with the results of the *benchmark* code. Figure 3.23 presents the results of the research

code along with the results of the *benchmark* code for pyrolysis gas blowing rate, surface recession and pyrolysis fronts. Both figures suggest that the results are in close agreement.

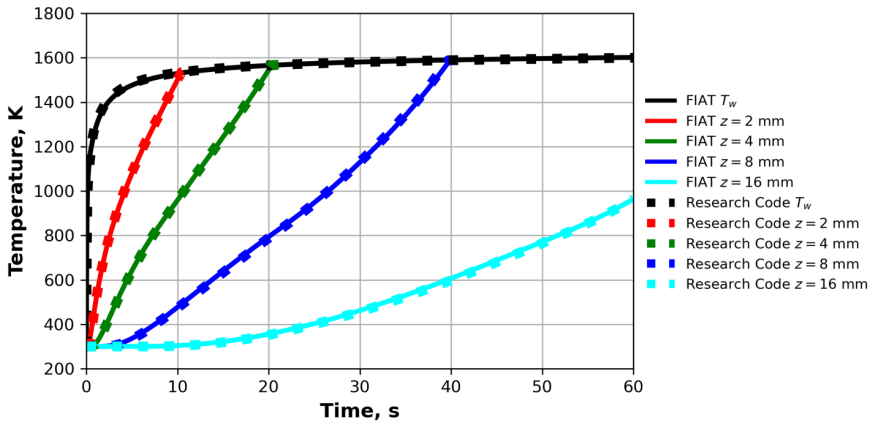


Figure 3.22: Comparison of temperatures at pre-determined locations for verification case 7

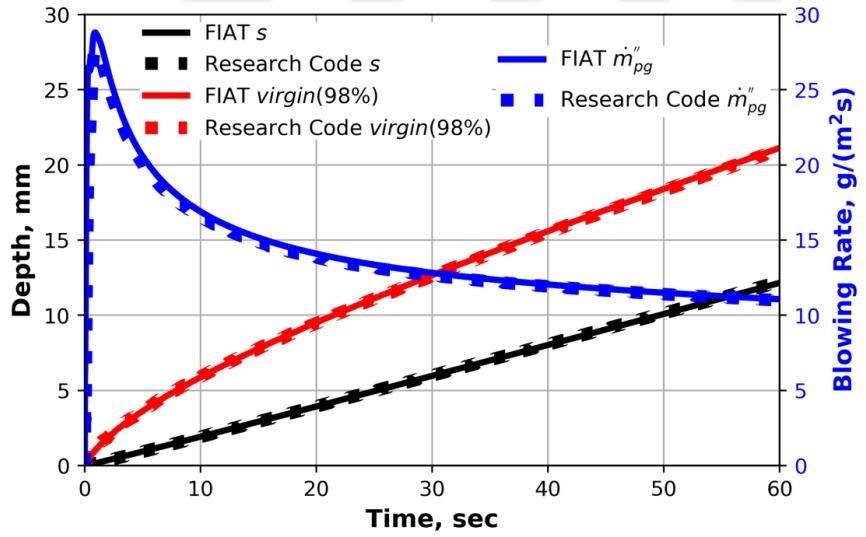


Figure 3.23: Comparison of pyrolysis gas blowing rate and char/pyrolysis fronts for verification case 7

Table 3.9 gives the L_∞ error norm of the solution variables, i.e. maximum error throughout the simulation time. Similar to verification case 6 the maximum error in pyrolysis gas blowing rate, $\dot{m}''_{pg}$, 43.9% is considerable higher compared to errors in other variables. An abrupt change in the pyrolysis gas blowing rate at the beginning

of the analysis due to intense heating is also observed in this case. Figure 3.24 shows the variation of $\dot{m}''_{pg}$ in the close proximity to time when the maximum error occurs. The results are very similar in behavior, however, the *benchmark* code estimates the blowing rate to be higher. This behavior may also be the outcome of the *benchmark* code's aforementioned assumption. Apart from the time between $0.1 - 1.0\ s$, the results are in close agreement. In this view, it can be inferred that the maximum error in $\dot{m}''_{pg}$ is not evident of any deficiencies in the research code and the research code gives acceptable results.

Table 3.9: L_∞ error norms for verification case 7

Error Norm	T_w	T_{2mm}	T_{4mm}	T_{8mm}	T_{16mm}	$\dot{m}''_{pg}$	s	$virgin(98\%)$
L_∞, %	2.05	0.72	0.30	0.64	1.29	43.9	0.58	0.62

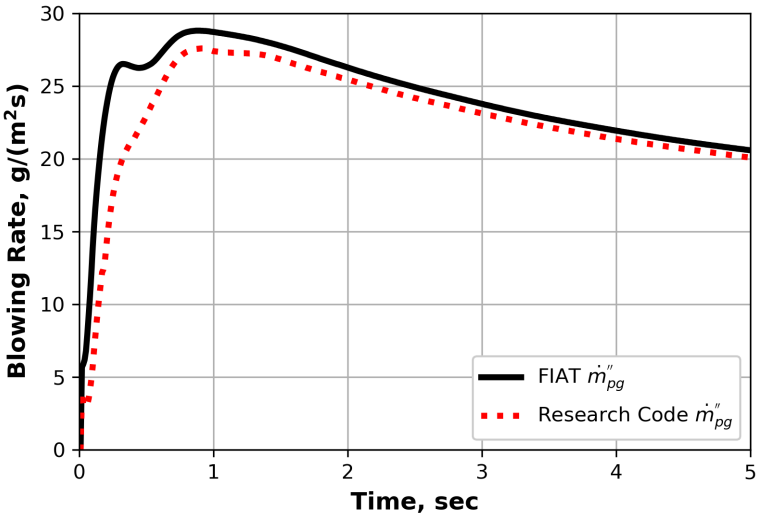


Figure 3.24: Abrupt change in pyrolysis gas blowing rate in verification case 7

CHAPTER 4

THERMAL NON-EQUILIBRIUM AND CHEMICAL PHENOMENA

In the previous chapters, local solid and gas temperatures are assumed to be equal, and pyrolysis gases are considered to be in chemical equilibrium. These assumptions greatly facilitate the modeling and analysis of the charring ablative materials since the pyrolysis gases can be treated as a single entity and a single energy equation is required to be solved in order to obtain the temperature distribution on the material. However, these assumptions may break down and thus thermal and chemical non-equilibrium shall be included in the analysis. In this chapter, modeling of thermal and chemical non-equilibrium phenomena that may take place beneath the ablating surface is considered. In addition, results of the additional verification and validation studies are presented.

Local thermal equilibrium between the solid and fluid phases in a porous media is achieved when thermal communication is effective and physical properties are close enough so that the local temperature difference between the phases is negligibly small [79]. Indeed, at the interface between the phases temperature and heat flux must be the same; however, the average temperature over a representative elementary volume, over which the macroscopic quantities are obtained by statically averaging microscopic quantities, does not have to be identical for the two phases [80]. When a significant heat generation takes place in any one of the phases, or when the boundary conditions change substantially with respect to time, and when the phases have considerable different thermal properties, the system will be far from the local thermal equilibrium [81].

In the literature on charring ablative materials, there has been little discussion about the local thermal non-equilibrium and there exist contradictory reports about the im-

portance of this phenomenon. Some researchers [14, 16, 23, 27, 82] recognize that local thermal equilibrium assumption may not be valid for all materials over all temperature and pressure regimes and then could lead to false prediction of the recession rate and in-depth temperatures. However, other works [83, 84] suggest that characteristic values for typical charring ablative materials such as pore size and velocity of the pyrolysis gases lead to effective thermal interaction between the phases, i.e. local thermal equilibrium.

Similar to the local thermal non-equilibrium phenomenon, effects of chemical equilibrium assumption have been subject to appreciable debate in the existing few works. Chen and Milos [25] claim that presence of chemical non-equilibrium does not significantly alter the in-depth thermal response performance predicted using the chemical equilibrium gas model whereas Lachaud et al. [26] reported that an increase in the predicted temperatures is observed when chemical non-equilibrium is assumed compared to chemical equilibrium solution and Scoggins [23] stated that the char temperature is lower for the reacting gases than the frozen flow.

4.1 Governing Equations

4.1.1 Thermal Non-equilibrium

When local thermal equilibrium is not assumed between the solid and fluid inside a porous medium, two separate but coupled energy equations have to be solved: fluid energy conservation equation and solid energy conservation equation. The thermal interaction between the phases can be approached either by the examination of the microstructure of the material or by empiricism. When empiricism is applied, two-equation models that contain volumetric heat transfer coefficient, h_V, as a parameter at the solid-fluid interface are used. The energy equations are then given of the form [85]:

$$\epsilon \rho_f c_{p,f} \left[\frac{\partial T_f}{\partial t} + \nabla \cdot (\mathbf{u_f} T_f) \right] = \epsilon k_f \nabla^2 T_f + h_V (T_s - T_f) \tag{4.1}$$

$$\rho_s c_{p,s} \frac{\partial T_s}{\partial t} = (1 - \epsilon) k_s \nabla^2 T_s - h_V (T_s - T_f) \tag{4.2}$$

for the fluid and solid phases, respectively. It should be noted that while the fluid density, ρ_f, is the true density, density of the solid phase, ρ_s, is the bulk density.

In the context of charring ablative materials, thermal decomposition of the solid phase produces pyrolysis gases and thus, the interfacial mass transfer must be included in the energy equations. The gas and solid phase energy equations are then given of the following integral forms for an arbitrary control volume as:

$$\underbrace{\frac{\mathrm{d}}{\mathrm{d}t}\iiint \epsilon\rho_{pg}e_{pg}\mathrm{d}V}_{\text{energy storage}} + \underbrace{\iint \epsilon k_{pg}\nabla T_{pg}\cdot\mathbf{n}\mathrm{d}S}_{\text{conduction}} + \underbrace{\iint \epsilon\rho_{pg}h_{pg}\mathbf{u_{pg}}\cdot\mathbf{n}\mathrm{d}S}_{\text{gas flow}} - \underbrace{\iint \epsilon\rho_{pg}h_{pg}\mathbf{u_{cs}}\cdot\mathbf{n}\mathrm{d}S}_{\text{grid convection}} - \underbrace{\iiint h_V(T_s-T_{pg})\mathrm{d}V}_{\text{thermal coupling}} - \underbrace{\iiint \dot{m}'''_{gen}h_{pg}\mathrm{d}V}_{\text{mass transfer}} = 0 \tag{4.3}$$

$$\underbrace{\frac{\mathrm{d}}{\mathrm{d}t}\iiint \rho_s e_s\mathrm{d}V}_{\text{energy storage}} + \underbrace{\iint (1-\epsilon)k_s\nabla T_s\cdot\mathbf{n}\mathrm{d}S}_{\text{conduction}} - \underbrace{\iint \rho_s h_s\mathbf{u_{cs}}\cdot\mathbf{n}\mathrm{d}S}_{\text{grid convection}} + \underbrace{\iiint h_V(T_s-T_{pg})\mathrm{d}V}_{\text{thermal coupling}} + \underbrace{\iiint \dot{m}'''_{gen}h_{pg}\mathrm{d}V}_{\text{mass transfer}} = 0 \tag{4.4}$$

It is supposed that the generated gases are at the same temperature as the solid phase following Plumb's simplified, semi-heuristic phasic energy equation [86] that was developed to model phase change in porous media.

4.1.1.1 Volumetric Heat Transfer Coefficient

The volumetric heat transfer coefficient is the crucial parameter that couples the gas phase energy equation to the solid phase energy equation and its proper determination is essential for the accuracy of the analysis. There exist several remarkable studies on the estimation of the volumetric heat transfer coefficient primarily for low porosity packed beds [87–89] or metal foams [90–92]. Nevertheless, use of the correlations obtained with packed beds or metal foams for lightweight charring ablative materials may yield unrealistic results due to several factors such as much lower porosity and mean particle diameter and much higher thermal conductivity for metals than for insulator [93]. In this work, correlation developed by Nakayama et al. [94] for low

density consolidated porous media is adopted for the estimation of the volumetric heat transfer coefficient between the phases. This correlation covers most of available data on high porosity ceramic foams and other correlations [95, 96] developed for high porosity porous materials. The correlation uses the mean pore diameter, d_m, as characteristic length in defining the volumetric Nusselt number, Nu_V, as:

$$Nu_V = \frac{h_V d_m^2}{k_{pg}} = 0.07 \left(\frac{\epsilon}{1-\epsilon} \right)^{2/3} \left(\frac{\epsilon u_{pg} d_m}{\nu_{pg}} \right) Pr \tag{4.5}$$

where ν is the kinematic viscosity and Pr is the Prandtl number of the pyrolysis gas mixture. Eq. 4.5 is given for $0.7 \leq \epsilon \leq 0.95$ and $3 \leq (\epsilon u_{pg} d_m / \nu_{pg}) \leq 1000$. A minimum volumetric Nusselt number of $Nu_{V,min} = 0.3$, which corresponds roughly to the value obtained when $\epsilon = 0.7$ and $(\epsilon u_{pg} d_m / \nu_{pg}) = 3$, is defined, since it is obvious and rational that a limiting Nusselt number, i.e. a constant plateau value, should exist at low velocity/stagnant flow condition where conduction prevails over advection in heat transfer rate between the solid and fluid [97].

In general, porosity, ϵ, and permeability, κ, of the charring ablative materials are given, and the mean particle diameter is an unknown parameter. In order to estimate the mean pore diameter through porosity and permeability of the material, the following two correlations are utilized:

$$\kappa = 3.824 \epsilon^{24.93} d_f^{1.947} \tag{4.6}$$

where d_f is the equivalent fiber (strut) diameter, and

$$\frac{d_f}{d_m} = 2\sqrt{\frac{1-\epsilon}{3\pi}} \left(\frac{1}{1 - e^{-(1-\epsilon)/0.004}} \right) \tag{4.7}$$

The first empirical formula, Eq. 4.6, is derived by Kamiuto [98] using parameter estimation method to the available experimental data for open-cellular foams and relates the permeability to the porosity and equivalent fiber diameter. The second correlation, Eq. 4.7, proposed by Calmidi [99] using open cell representation for complex structure of foams illustrated in Figure 4.1 gives the mean pore diameter as a function of porosity and equivalent fiber diameter. The mean pore diameter can thus be expressed a function of porosity and permeability. It is worth to note that the mean pore diameter is not a constant since permeability and porosity of the ablative material changes during heating due to pyrolysis decomposition.

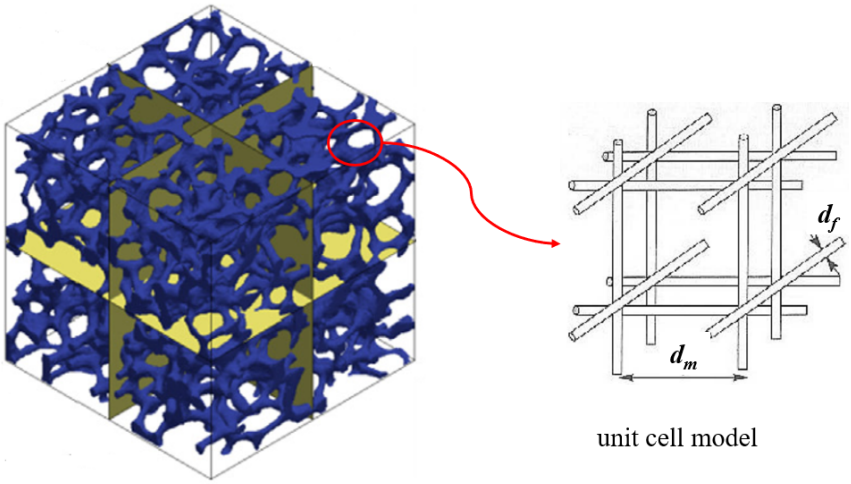


Figure 4.1: Detailed and unit cell representation of open cell foams [100, 101]

4.1.2 Chemical Phenomena

4.1.2.1 Chemical Reactions and Chemical Time Scales

Chemical reactions can occur on very different time scales compared to other phenomena such as fluid flow and diffusion and advection of heat. Figure 4.2 compares the time scales in a chemically reacting flow with time scales of different processes. Damköhler number, Da, the ratio of characteristic flow time, τ_{flow}, to characteristic chemical time, τ_{flow}, is used to define the chemistry models and is given as :

$$Da = \frac{\tau_{flow}}{\tau_{chem}} \tag{4.8}$$

If chemical reactions are very slow compared to other processes, i.e. $Da \to 0$, the chemical composition can be assumed to be fixed, and flow is denoted as *frozen*. In contrast, if the chemical reactions are very fast compared to other processes, i.e. $Da \to \infty$, flow is denoted as in *chemical equilibrium* and thermodynamics are sufficient to determine the chemical composition. Apart from these two limiting cases, chemical composition of a mixture can only be determined through *finite-rate* chemical reactions.

If the flow is assumed to be frozen, then the initial chemical composition does not change in space and time. If the flow is assumed to be in chemical equilibrium, the

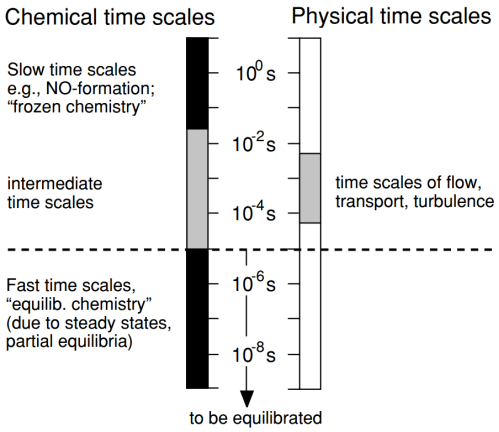


Figure 4.2: Time scales in a chemically reacting flow [102]

equilibrium composition can be determined via a state variable, the free enthalpy of Gibbs function, G, which is defined as:

$$G = H - TS \tag{4.9}$$

where H and S is the enthalpy and entropy, respectively. The capital letters denote that they are extensive properties. The criterion for chemical equilibrium is the minimization of the energy:

$$(\mathrm{d}G)_{p,T} = 0 \tag{4.10}$$

where the subscripts represent the conditions that are kept constant during the process, i.e. pressure and temperature. For the calculation of equilibrium composition, species in the mixture must be determined in advance and the conserved variables, i.e. chemical elements, must be specified. Then, the minimization procedure yields a set of non-linear equations which are in general solved by Newton's method.

If the flow is neither frozen nor in chemical equilibrium, chemical reactions must be evaluated in order to determine the mixture composition. A chemical reaction can be described in general as:

$$A + B + C + \ldots \xrightarrow{k} D + E + F + \ldots \tag{4.11}$$

where $A, B, C, \ldots$ denote the species involved in the reaction. The rate of consumption or production of a species, i.e. *reaction rate*, is expressed using the rate law. For instance, the reaction rate of species A can be expressed as:

$$\frac{\mathrm{d}[A]}{\mathrm{d}t} = -k[A]^a[B]^b[C]^c \ldots \tag{4.12}$$

where k is the rate coefficient, and the exponents $a, b, c, \ldots$ are the reaction orders of the corresponding species. The sum of the all exponents is regarded as the overall reaction order. The rate coefficient strongly depends on the temperature, and in general, is expressed using the Arrhenius law as:

$$k = ZT^{\vartheta} e^{-E_a/(R_u T)} \tag{4.13}$$

where ϑ is the temperature exponent.

In general, the chemical time scale of a reaction is a function of rate coefficient and reactant concentrations, and is independent of the length scale of the medium where the reaction takes place. Due to the Arrhenius kinetics, chemical time scale of a reaction increases exponentially as the temperature decreases and different reactions have vastly different time scales.

4.1.2.2 Species Mass Conservation

In chemically reacting flows species mass conservation equations have to be solved in addition to the energy, momentum and global mass conservation equations. The species mass conservation equations for reacting pyrolysis gases flowing through a porous decomposing and receding medium can be written as:

$$\begin{aligned} &\frac{\mathrm{d}}{\mathrm{d}t}\iiint \epsilon\rho_{pg} Y_i \mathrm{d}V + \iint [\epsilon\rho_{pg} Y_i(\mathbf{u_{pg}} - \mathbf{u_{cs}} + \mathbf{U_{k,i}})] \cdot \mathbf{n}\mathrm{d}S \\ &= \iiint \epsilon\dot{\omega}_i^{'''}\mathrm{d}V + \iiint \dot{m}_{gen,i}^{'''}\mathrm{d}V, \quad i = 1, 2, 3, \ldots, N_S \end{aligned} \tag{4.14}$$

where $\dot{\omega}^{'''}$ is the volumetric mass production rate due to finite-rate homogeneous reactions, $\dot{m}_{gen,i}^{'''}$ is the mass production rate due to pyrolysis decomposition reactions and N_S is the number of species. The diffusion velocity of a species i, $\mathbf{U_{k_i}}$, can be approximated using Fick's law of diffusion as given in Eq. 2.29.

The mass production rate due to pyrolysis decomposition is governed by decomposition kinetics and the mass fractions of each species at the decomposition products. If the decomposition is assumed to be under chemical equilibrium, mass fraction of each species can be determined using a chemical equilibrium routine. Otherwise, heterogeneous chemical reactions have to be taken into account. The mass production rate due to finite-rate homogeneous reactions is governed by a set of chemical

reactions which can be expressed in compact notation as:

$$\sum_{i=1}^{N_S} v_{ij}^{'} A_i \overset{k_j^f}{\underset{k_j^r}{\leftrightarrows}} \sum_{i=1}^{N_S} v_{ij}^{''} A_i, , \quad j = 1, 2, 3, \ldots, N_R \tag{4.15}$$

where $v_{ij}^{'}$ and $v_{ij}^{''}$ denote stoichiometric coefficients of species i as a reactant and a product of reaction j, respectively, k_j^f and k_j^r are the forward and reverse reaction rate coefficients for reaction j and N_R is the number of reactions. The reaction rate of reaction j, r_j, can then be expressed as:

$$r_j = k_j^f \prod_{i=1}^{N_S} [A_i]^{v_{ij}^{'}} - k_j^r \prod_{i=1}^{N_S} [A_i]^{v_{ij}^{''}} \tag{4.16}$$

Then, the rate of consumption or production of species i in reaction j, $\dot{\omega}_{ij}$, is:

$$\dot{\omega}_{ij}^{'''} = r_j (v_{ij}^{''} - v_{ij}^{'}) \tag{4.17}$$

Total mass production or consumption rate of species i is then expressed as:

$$\dot{\omega}_i^{'''} = MW_i \sum_{j=1}^{N_R} r_j (v_{ij}^{''} - v_{ij}^{'}) = MW_i \sum_{j=1}^{N_R} \dot{\omega}_{ij}^{'''} \tag{4.18}$$

Eq. 4.14 has to be solved for each species at each control volume along with energy, momentum, and global mass conservation equations. However, since the species mass fraction must add up to unity, the generally accepted procedure in combustion calculations is to solve $N_S - 1$ species conservation equations at each control volume and compute the mass fraction of the N_S^{th} species as:

$$Y_{N_S} = 1 - \sum_{i=1}^{N_S - 1} Y_i \tag{4.19}$$

Energy, momentum and global mass conservation equations remain intact and are not presented here, again. However, in order to explicitly show the influence of chemical reactions on the energy equation, the gas phase energy equation is written in terms of

sensible enthalpy, h^s_{pg}, and heat of formation, h^o_{pg}, instead of absolute enthalpy as:

$$\begin{aligned}
&\underbrace{\frac{\mathrm{d}}{\mathrm{d}t}\iiint(\epsilon\rho_{pg}h^s_{pg}-p)\mathrm{d}V}_{\text{energy storage}}+\underbrace{\iint\epsilon k_{pg}\nabla T_{pg}\cdot\mathbf{n}\mathrm{d}S}_{\text{conduction}}+\underbrace{\iint\epsilon\rho_{pg}h^s_{pg}\mathbf{u_{pg}}\cdot\mathbf{n}\mathrm{d}S}_{\text{gas flow}}\\
&\qquad-\underbrace{\iint\epsilon\rho_{pg}h^s_{pg}\mathbf{u_{cs}}\cdot\mathbf{n}\mathrm{d}S}_{\text{grid convection}}-\underbrace{\iiint h_V(T_s-T_{pg})\mathrm{d}V}_{\text{thermal coupling}}\\
&-\underbrace{\iiint\dot{m}'''_{gen}(h^0_{pg}+h^s_{pg})\mathrm{d}V}_{\text{mass transfer}}-\underbrace{\iiint\epsilon\left(\sum_{i=1}^{N_S}h^o_{pg,i}\dot{\omega}'''_i\right)\mathrm{d}V}_{\text{reactions}}=0
\end{aligned}\tag{4.20}$$

It shall be highlighted that since species diffusion is not considered in this work, the gas phase energy equation remains intact. Otherwise, an additional term accounting for species diffusion must be included in the gas phase energy equation.

4.1.2.3 Thermodynamic and Transport Properties of Pyrolysis Gases

Properties of the pyrolysis gas mixture depend on the temperature, pressure and composition of the mixture which alters unless flow is frozen. Thus, these variables must be determined in advanced and mixture properties are then evaluated. Accuracy of a numerical simulation heavily depends on how properly these properties are evaluated. Different theories and techniques for the evaluation of these properties are well documented in some sources such as [103, 104]. Here, only the adopted techniques are addressed.

Thermodynamic properties of a gaseous species i include the internal energy, e_i, entropy, s_i, enthalpy, h_i, and specific heats, $c_{p,i}$ and $c_{v,i}$. The specific heats are defined as:

$$c_{p,i}=\left(\frac{\partial h_i}{\partial T}\right)_p,\quad c_{v,i}=\left(\frac{\partial e_i}{\partial T}\right)_V \tag{4.21}$$

Thermodynamic properties are evaluated using NASA-9 polynomials [105]. These polynomials give more accurate predictions than other methods because they take into account the results of most accurate available experimental data. Properties are computed for standard state of one atmosphere pressure and one mole of matter. The molar heat capacity of a species at constant pressure for standard state, $\hat{C}^0_p$, is given

in the following form:

$$\frac{\hat{C}_p^0}{R_u} = \sum_{i=1}^{7} a_i T^{i-3} \tag{4.22}$$

where $a_i (i = 1, \ldots, 7)$ are the temperature coefficients, the superscript ^{0} denotes the standard state of one atmosphere and the *hat* accent $\hat{}$ states that property is given on molar basis. The enthalpy and entropy values are then calculated by integrating $\hat{C}_p^0$ and $\hat{C}_p^0/T$, respectively, as:

$$\frac{\hat{H}^0}{R_u} = \sum_{i=1, i\neq 2}^{7} a_i \frac{T^{i-2}}{i-2} + a_2 \ln T + \frac{b_1}{T} \tag{4.23}$$

$$\frac{\hat{S}^0}{R_u} = \sum_{i=1, i\neq 3}^{7} a_i \frac{T^{i-3}}{i-3} + a_3 \ln T + b_2 \tag{4.24}$$

where b_1 and b_2 are integration constants. In order to obtain the unit mass basis values, above relations can be divided by molecular weight, MW, of the corresponding species. Specific heat at constant volume and internal energy are then obtained using the following relationships:

$$c_v = c_p - \frac{R_u}{MW} \tag{4.25}$$

$$e = h - \frac{p}{\rho} \tag{4.26}$$

Entropy of an ideal gas is a function of both temperature and pressure whereas other properties is a function of temperature only. Between two thermodynamic states at different pressures the entropy difference can be obtained as:

$$s_2 - s_1 = s_2^0(T_2) - s_1^0(T_1) - \frac{R_u}{MW} \ln \frac{p_2}{p_1} \tag{4.27}$$

After evaluating the thermodynamic properties for each species, properties of the mixture are calculated as mass fraction weighted sums of the individual species properties as:

$$h = \sum_{i=1}^{N_S} Y_i h_i \tag{4.28}$$

$$e = \sum_{i=1}^{N_S} Y_i e_i \tag{4.29}$$

$$s = \sum_{i=1}^{N_S} Y_i s_i \tag{4.30}$$

Mixture specific heats are calculated through the partial derivatives of the mixture enthalpy and internal energy with respect to temperature. It shall be noted that for mixtures in chemical equilibrium the mass fractions of species are function of temperature. This dependency introduces an additional term to the specific heats of mixtures in chemical equilibrium as:

$$c_{p,eq} = \sum_{i=1}^{N_S} Y_i \left(\frac{\partial h_i}{\partial T}\right)_p + \underbrace{\sum_{i=1}^{N_S} h_i \left(\frac{\partial Y_i}{\partial T}\right)_p}_{\text{additional term}} \tag{4.31}$$

$$c_{v,eq} = \sum_{i=1}^{N_S} Y_i \left(\frac{\partial e_i}{\partial T}\right)_V + \underbrace{\sum_{i=1}^{N_S} e_i \left(\frac{\partial Y_i}{\partial T}\right)_V}_{\text{additional term}} \tag{4.32}$$

Transport properties of a gaseous species i include the dynamic viscosity, μ_i, thermal conductivity, k_i. Since species diffusion is not considered in this work, evaluation of diffusion coefficients is not addressed. Expression for the transport properties of individual gases, in general, are derived from kinetic theory of gases, and it is out of scope of this work. Once individual properties are known, mixture-averaged properties can be evaluated. For the dynamic viscosity, the semi-empirical Wilke formula [106] is used:

$$\mu = \sum_{i=1}^{N_S} \frac{X_i \mu_i}{\sum_{i=j}^{N_S} X_j \Phi_{ij}} \tag{4.33}$$

where X is the mole fraction and Φ_{ij} is defined as:

$$\Phi_{ij} = \frac{1}{\sqrt{8}} \left(1 + \frac{MW_i}{MW_j}\right)^{-0.5} \left(1 + \left(\frac{\mu_i}{\mu_j}\right)^{0.5} \left(\frac{MW_i}{MW_j}\right)^{0.25}\right)^2 \tag{4.34}$$

In the case of thermal conductivity, the following averaging formula [107] is used:

$$k = 0.5 \left(\sum_{i=1}^{N_S} X_i k_i + \frac{1}{\sum_{i=1}^{N_S} X_i / k_i}\right) \tag{4.35}$$

4.2 Numerical Implementation

Discretization of the gas phase and solid phase energy equations, i.e. Eq. 4.3 and Eq. 4.4, respectively, results in the sensitivity matrix of the form:

$$\begin{bmatrix} r_0 & \mathbf{0} & \mathbf{0} \\ \mathbf{r_{pg}} & \mathbf{G} & \mathbf{\Gamma} \\ \mathbf{r_s} & \mathbf{\Gamma} & \mathbf{S} \end{bmatrix} \begin{bmatrix} \Delta\dot{s} \\ \mathbf{\Delta T_{pg}} \\ \mathbf{\Delta T_s} \end{bmatrix} = \begin{bmatrix} f_1 \\ \mathbf{f_{pg}} \\ \mathbf{f_s} \end{bmatrix} \tag{4.36}$$

where $\mathbf{G}$ and $\mathbf{S}$ contain the coefficients for the gas and solid energy equations, and $\mathbf{\Gamma}$ stands for the coupling terms with volumetric heat transfer coefficient between the two phases. $\mathbf{r}$ accounts for the sensitivities due to surface recession, and $\mathbf{f}$ is the residual vector. The linear system in Eq. 4.36 is solved using the Crout decomposition [63], a LU factorization algorithm, iteratively until the convergence of the residuals is achieved.

Species conservation equations are in general stiff differential equations whose solution requires special treatment. Several options are assessed such as coding by hand or integrating an external stiff ordinary equation solver library such as CVODE [108] to the research code. Coding by hand would be very painful and error-prone especially for the evaluation of the chemical source terms. For each chemical species a Jacobian matrix of $N_S \times N_S$ has to be formed and solved using Newton's method. However, since the equations are in general stiff, different methods other than first-order implicit Euler may need to be employed. Solving the differential equations via CVODE would alleviate the workload considerably. However, Jacobian matrix still has to be formed inside the research code and supplied to the CVODE. These alternatives do not provide the desired flexibility such that different reaction mechanisms with different set of chemical species would require substantial re-coding. Ultimately, it is figured out that integration of Cantera, an open-source library which performs chemical kinetics and equilibrium calculations, [109] to the research code and utilizing its existing solvers would overcome the drawbacks of the aforementioned alternatives.

Cantera offers several zero-dimensional (0D) and one-dimensional (1D) reacting flow simulation tools and is integrated with CVODE, which provides implementations of the variable coefficient Adams-Moulton method and the Backward Differentiation Formula methods to integrate first-order non-stiff and stiff ordinary differential equa-

tions, respectively. Applicability of the 1D reacting flow simulation tools is hindered by the fact that Cantera does not take into account terms that arise from the movement of the mesh due to surface recession and species mass production rate due to pyrolysis decomposition reactions. Zero-dimensional simulation tools are, in general, used to model various homogeneous *reactors* which contain quantities that may evolve temporally but not spatially. Although reactors are zero-dimensional, they can be used as building blocks to model complex practical applications. Reactors can have multiple inlets/outlets which can be constants or functions. A reactor network can be constructed connecting several reactors. Reactors can also be connected to the *reservoirs* which can be thought of as an infinitely large volume, in which all states are predefined and never change from their initial values. In addition, heat transfer can be defined between reactors and volume of the reactor may change with time.

Since reactors can be used as a well-defined small component of the global structure and can interact with other components, usage of them seems to be appealing to model the species mass conservation equations within the ablative material. It is deduced that each control volume can be regarded as a reactor in which chemical reactions take place and a reactor network can be formed to simulate the 1D domain. Figure 4.3 depicts the spatial discretization of a 1D domain and its reactor network representation to imitate Eq. 4.14.

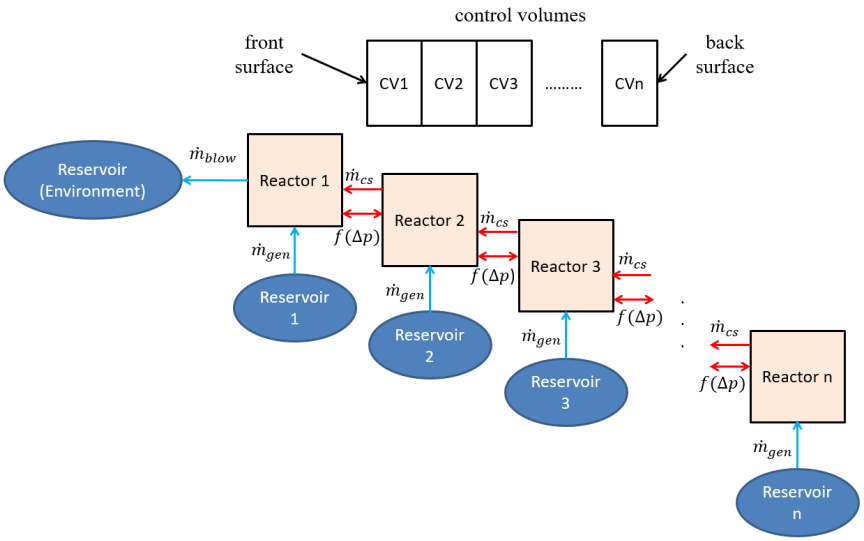


Figure 4.3: Reactor network representation of a 1D domain

The net change in the mass of each species in a reactor is given as:

$$\frac{\mathrm{d}}{\mathrm{d}t}(mY_i) = \sum_{in} \dot{m}_{in} Y_{in,i} - \sum_{out} \dot{m}_{out} Y_i + \dot{m}_{reac,i}, \quad i = 1, 2, 3, \ldots, N_S \tag{4.37}$$

where $\dot{m}_{reac,i}$ is the species mass generation due to homogeneous and/or heterogeneous reactions. Since rate change of the content of the reactor and species mass generation term due to homogeneous reactions are taken into account inherently, the important point is to define the inlets and outlets of each reactor properly. At this point it would be beneficial to summarize the Cantera's built-in two flow devices used to model mass transfer between reactors/reservoirs, briefly. The first one is denoted as *MassFlowController* which allows the mass flow rate to be specified either constant or time-dependent. The second one is denoted as *Valve* which allows the mass flow rate to be specified as a function of pressure difference as:

$$\dot{m} = K_v(p_2 - p_1) = K_v \Delta p \tag{4.38}$$

where K_v is the valve coefficient and can be either constant or an arbitrary function. By setting the K_v to a sufficiently large value, very small pressure differences will result in between the reactors/reservoirs. This method is applied to impose pressure boundary condition at the ablating surface.

Mass transfer terms depicted in Figure 4.3 and the corresponding terms given in Eq. 4.14 can be written as:

$$\begin{gathered} \iint [\epsilon \rho_{pg} Y_i(\mathbf{u_{pg}})] \cdot \mathbf{n} \mathrm{d}S = f(\Delta p) Y_i \\ \iint [\epsilon \rho_{pg} Y_i(\mathbf{u_{cs}})] \cdot \mathbf{n} \mathrm{d}S = \dot{m}_{cs} Y_i \\ \iiint \dot{m}'''_{gen,i} \mathrm{d}V = \dot{m}_{gen} Y_i \\ i = 1, 2, 3, \ldots, N_S \end{gathered} \tag{4.39}$$

The first term in Eq. 4.39 is the species mass transport due to the bulk motion of the pyrolysis gases which is evaluated using Darcy's law, i.e. Eq. 2.17. In reactor network approach, it is modeled using the *Valve* object by setting the K_v as:

$$K_v = S \rho_{pg} \frac{\kappa}{\mu \Delta z} \tag{4.40}$$

The second term is the species mass transport due to the control surface movement resulting from the receding ablating surface. This term is modeled using the *MassFlowController* object by setting the mass flow rate as:

$$\dot{m}_{cs} = S\epsilon\rho_{pg}u_{cs} \tag{4.41}$$

where u_{cs} is given in Eq. 3.10.

The last term is the mass production rate due to pyrolysis decomposition reactions of the solid phase. Since this generation term cannot be defined within a reactor, reservoirs are introduced in the reactor network, and a *MassFlowController* object is used to model this term by setting the mass flow rate as:

$$\dot{m}_{gen} = \dot{m}'''_{gen}V \tag{4.42}$$

where $\dot{m}'''_{gen}$ is the volumetric mass generation due to decomposition process which is calculated by solving the solid continuity equation, and V is the volume of the corresponding control volume, i.e. reactor.

The solution procedure for the entire system of governing equations can then be outlined as follows:

- Surface recession rate and nodal temperatures are computed from the solid and gas phase energy equations iteratively and the grid is updated at every iteration by using contracting grid scheme. Solid density, gas density, as well as gas velocity are kept constant.
- Nodal solid densities are computed from the solution of solid phase continuity and pyrolysis kinetic equations. The updated temperatures and grid are used.
- Nodal gas densities and species mole and mass fractions are computed solving the species continuity equations using Cantera. Darcy's law is used to determine the pyrolysis gas velocity. The updated gas temperatures and the grid are used. Flow device definitions are updated.

The sequential (segregated) solution scheme is illustrated in Figure 4.4 and Figure 4.5. The dependent variables for each conservation equation are shown in rectangle boxes in Figure 4.4. The solution of the conservation equations is calculated independently

at every time step. A first-order implicit time integration scheme is employed to solve energy equations. Cantera uses CVODE to integrate species continuity equations in the reactor network. For each global time step, CVODE takes as many integrator time steps as necessary as shown in Figure 4.5.

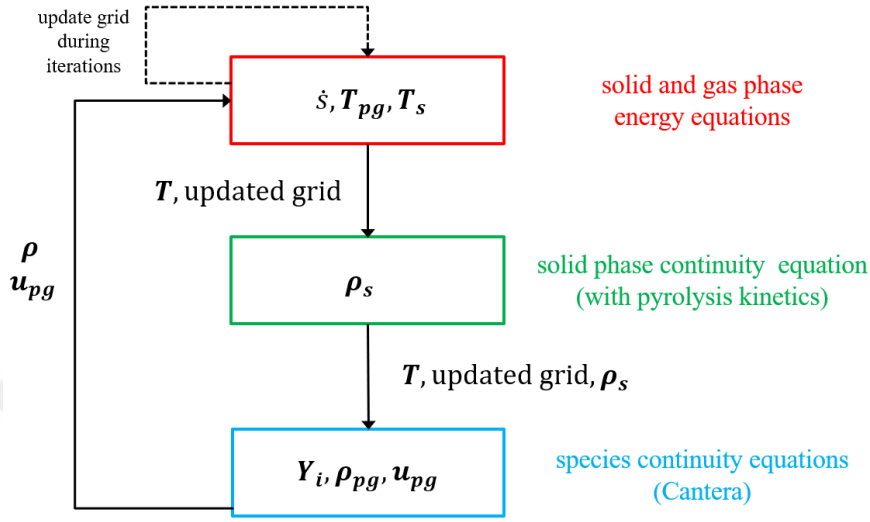


Figure 4.4: Solution procedure

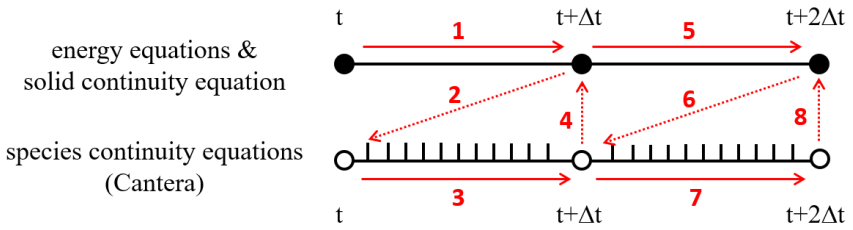


Figure 4.5: Time progress of the solution

4.3 Verification and Validation Studies

In this section, results of additional verification and validation studies are demonstrated. These studies intend to show that implementation of the reactor network approach and thermal non-equilibrium phenomenon and creation of B' Tables are carried out properly. In addition, comparison of estimations with arc-jet test data of PICA material is presented. Verification of homogeneous chemical reaction calcu-

lations is not considered since these calculations are carried out using a third party library, i.e. *Cantera*, which has its own verification studies.

4.3.1 Validity of Ideal Gas Approximation

In order to exhibit ideal gas behavior, a gas has to have one defining attribute: gas molecules do not exert any forces on one another, therefore, no inter-molecular potential energy exists. This attribute suggests that an ideal gas does not undergo a phase change even if it is compressed to zero volume, and is strict assumption except supercritical substances at low pressure [110]. The ideal gas approximation becomes less rational if a gas is not super-heated due to closeness of the molecules.

Deviation from the true property, i.e. the validity of the ideal gas assumption, can be quantified in two ways: Difference measure and ratio measure. In the first, the deviation is expressed in the form of:

$$F_{dev} = F - F_{id} \tag{4.43}$$

where F is the true property, the subscripts dev and id refer to deviation and ideal values, respectively. In the latter, the deviation takes the form of:

$$F_{dev} = \frac{F}{F_{id}} \tag{4.44}$$

In this work, the compressibility factor approach, which is a ratio measure, is utilized to validate the ideal gas behavior of the pyrolysis gas mixture. The compressibility factor, Z, is defined as:

$$Z = \frac{p}{\rho T}\frac{MW}{R_u} \tag{4.45}$$

The compressibility factor indicates the deviation of the volume from the ideal gas volume at the same temperature and pressure. For an ideal gas $Z = 1$, and the deviation from unity is a measure of the differences between the actual value and the ideal gas value. Compressibility factor tables for different gases as a function of temperature and pressure can be found in the literature. However, the common approach is to use the generalized compressibility data which is valid for different gases that are not strongly polar or hydrogen bonded [103] when non-dimensional

reduced temperature, T_r, and reduced pressure, p_r, are introduced, i.e. the principle of corresponding states. The reduced properties used to evaluate the compressibility of a gas are defined as:

$$T_r = \frac{T}{T_c} \tag{4.46}$$

$$p_r = \frac{p}{p_c} \tag{4.47}$$

where the subscript c denotes the properties at the critical point.

The principle of corresponding states can be extended to mixtures by regarding the mixture as if it is a single pure component having critical properties calculated by one of several mixture rules [111]. One widely used mixture rule is Kay's rule in which mole fraction averaged critical properties are used to determine the compressibility factor as:

$$T_c = \sum_{i=1}^{N_S} X_i T_{c,i} \tag{4.48}$$

$$p_c = \sum_{i=1}^{N_S} X_i p_{c,i} \tag{4.49}$$

Table 4.1: Initial mole fractions of pyrolysis gases of TACOT material [77]

C	CH_4	C_2H_2	C_2H_4	C_2H_6	C_6H_6
0.0	0.10	0.0	0.0	0.0	0.004 79

C_6H_5OH	CO	CO_2	H_2	H_2O
0.089 14	0.057 63	0.015 65	0.4992	0.2336

The pyrolysis gas mixture of the TACOT material contains 11 species and the reference (initial) mole fractions of the species are given in Table 4.1. Variation of the mole fractions with temperature are evaluated under the assumption of chemical equilibrium at one atmosphere pressure. Then, using Kay's rule, reduced properties of the pyrolysis gas mixture are calculated as a function of the mixture temperature

and shown in Figure 4.6. Reduced properties of individual species, whose reduced pressure is greater than 1.0×10^{-5}, as a function temperature are given in Figure 4.7. As seen, the reduced pressure of the mixture lies between 0.01 and 0.04. Figure 4.8 shows the generalized compressibility factor chart. At this very low reduced pressure range, regardless of the reduced temperature, the compressibility factor is very close to unity. Thus, it can be claimed that pyrolysis gas mixture obeys the ideal gas law.

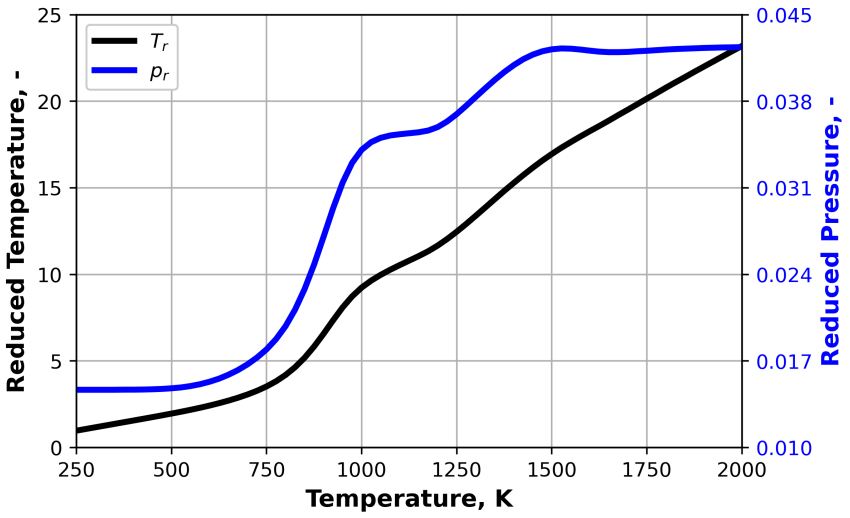


Figure 4.6: Reduced property variation of pyrolysis gas mixture

4.3.2 Steady-State Porous Flow

This verification study is performed to prove that the usage of flow devices in a reactor network can simulate the pyrolysis gas flow through the porous ablative material properly. Darcy's law is implemented to model the gas flow inside the porous material as discussed in Section 2.1.3 and the *Valve* flow device is introduced between the reactors to model the gas flow resulting from pressure gradient.

This verification problem and its analytical solution are taken from [112] and it considers the steady flow of a gas through a porous material. At steady-state the continuity equation can be written as:

$$\nabla \cdot (\epsilon \rho_{pg} \mathbf{u_{pg}}) = 0 \tag{4.50}$$

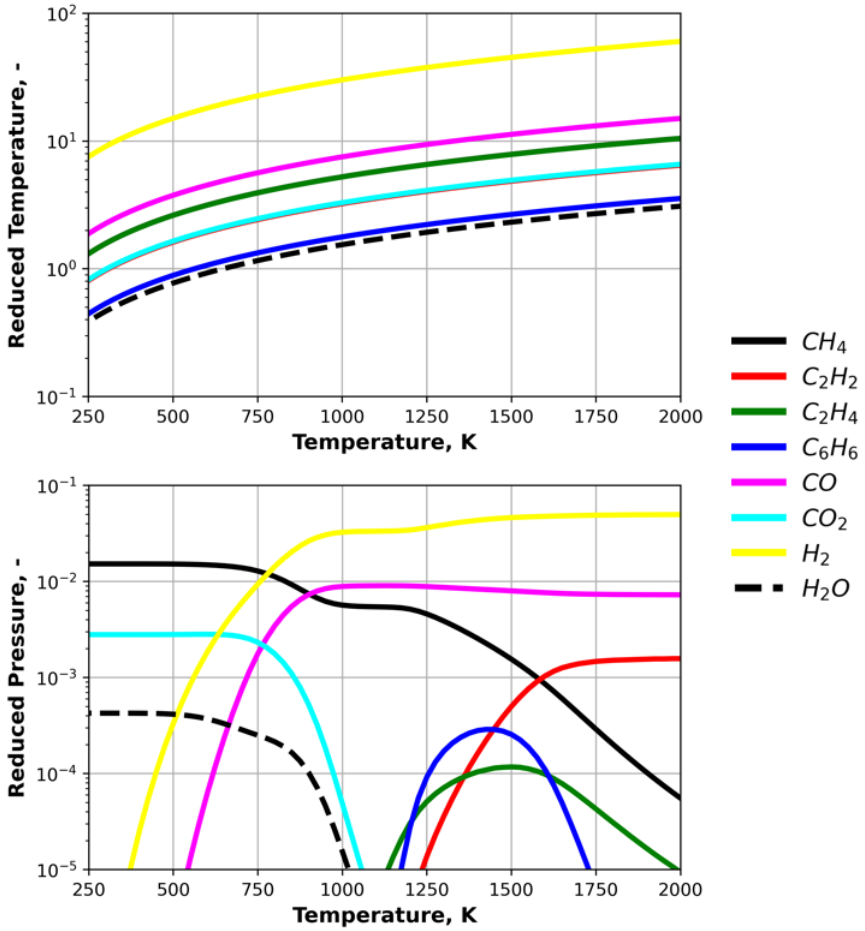


Figure 4.7: Reduced property variation of individual species

Substitution of Eq. 2.16 into Eq. 4.50 and assuming that the gas obeys the ideal law yield the following expression:

$$\frac{\kappa T}{\mu_{pg}} \frac{R_u}{MW} \nabla \cdot (\rho_{pg} \nabla \rho_{pg}) = 0 \tag{4.51}$$

For one-dimensional domain Eq. 4.51 can be expressed as:

$$\frac{\mathrm{d}}{\mathrm{d}z} \left(\rho_{pg} \frac{\mathrm{d}\rho_{pg}}{\mathrm{d}z} \right) = 0 \tag{4.52}$$

or

$$\rho_{pg} \frac{\mathrm{d}\rho_{pg}}{\mathrm{d}z} = C \tag{4.53}$$

where C is a constant. Integration of Eq. 4.53 along with the following boundary conditions:

$$\begin{aligned} \rho_{pg}(z = 0) &= \rho_0 \\ \rho_{pg}(z = L) &= \rho_L \end{aligned} \tag{4.54}$$

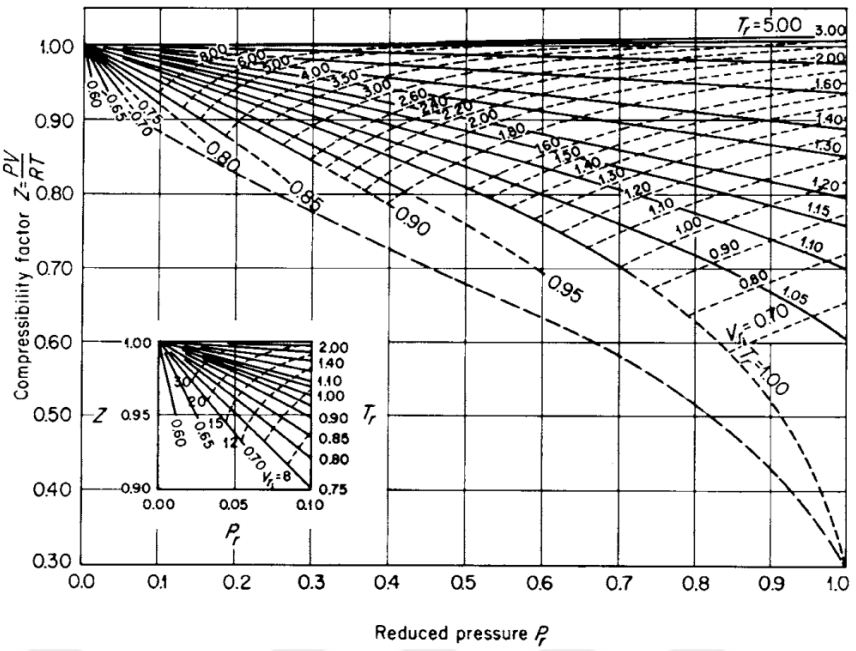


Figure 4.8: Generalized compressibility chart [103]

results in:

$$\rho_{pg}(z) = \left[\frac{\rho_L^2 - \rho_0^2}{L} z + \rho_0^2\right]^{0.5} \tag{4.55}$$

The pressure field can be obtained by invoking the ideal gas law as:

$$p(z) = \left[\frac{p_L^2 - p_0^2}{L} z + p_0^2\right]^{0.5} \tag{4.56}$$

Table 4.2 gives the simulation parameters for this verification problem. The grid convergence study is not necessary for this problem since the steady-state solution is independent of element size. Figure 4.9 compares the result of the research code with the analytical solution. Research code result is obtained using 100 equal-size elements. The L_2 error norm is calculated as $1.306\,35 \times 10^{-5}\ kg/m^3$.

4.3.3 Two-Equation Model

This verification case demonstrates the proper implementation of the two-equation model by comparing the solution against non-equilibrium porous media modeling performed using a commercial computational fluid dynamics code, i.e. *Star-CCM+* [113]. A $0.1\ m$ porous medium is discretized into 100 equal-size cells. The en-

Table 4.2: Problem parameters for steady porous flow problem

Property	Value
Length, L, m	0.1
Pressure at front face, p_0, Pa	100 000.0
Pressure at back face, p_L, Pa	10 000.0
Temperature, T, K	300.0
Molecular weight, MW, $kg/kmol$	28.013
Permeability, κ, m^2	2.0×10^{-11}
Dynamic viscosity, μ, $Pa \cdot s$	1.8017×10^{-5}

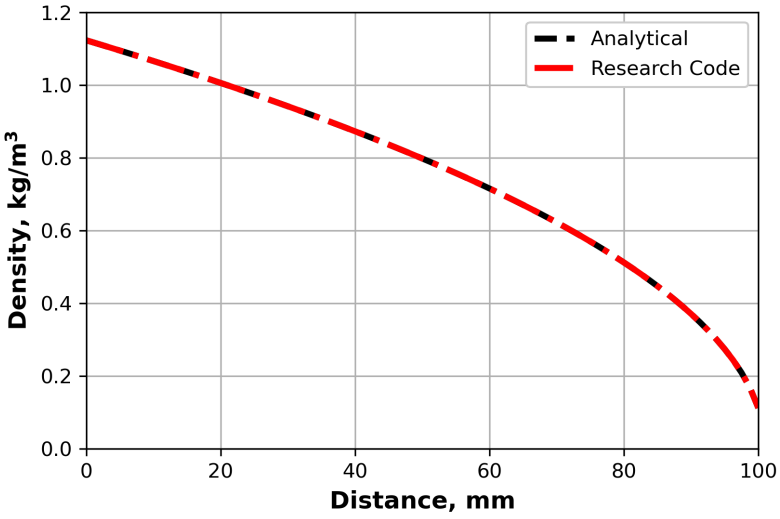


Figure 4.9: Comparison result for steady porous flow verification study

tire domain is initialized at 300 K and one atmosphere pressure. The porosity and permeability of the porous medium are kept constant as 0.5 and 1.0×10^{-10} m^2, respectively. Constant heat flux of 2000 W/m^2 is applied to the front surface. Adiabatic boundary condition is set to both the solid and fluid regions of the back surface. The verification problem is illustrated in Figure 4.10. The volumetric heat transfer coefficient between the solid and fluid domains is set to 5 $W/(m^3 \cdot K)$. Constant properties

of the solid and fluid are given in Table 4.3 and Table 4.4, respectively.

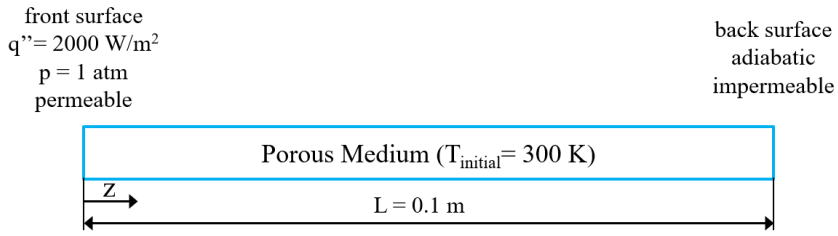


Figure 4.10: Boundary conditions for two-equation model verification study

Table 4.3: Properties of solid domain

Property	Value
Density, ρ, kg/m^3	20.0
Specific heat, c_p, $J/(kg \cdot K)$	1000.0
Thermal conductivity, k, $W/(m \cdot K)$	0.2

Table 4.4: Properties of fluid domain

Property	Value
Molecular weight, MW, $kg/kmol$	25.0
Dynamic viscosity, μ, $Pa \cdot s$	1.0×10^{-5}
Specific heat, c_p, $J/(kg \cdot K)$	5000.0
Thermal conductivity, k, $W/(m \cdot K)$	0.001

Figure 4.11 and Figure 4.12 compare the temperature variation at three different locations of the porous medium with those obtained from *Star-CCM+* for the solid and fluid phases, respectively. Figure 4.13 gives the comparison results for the variation of temperature difference between the phases. Table 4.5 gives the infinity error norms of the solid and fluid temperatures, i.e. $L_{\infty,s}$ and $L_{\infty,f}$, respectively. It is clear that a very good agreement is achieved between the codes.

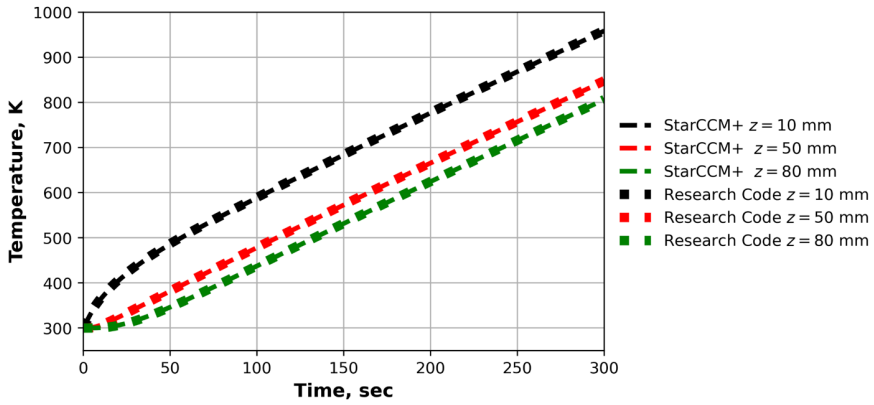


Figure 4.11: Comparison results for solid temperatures

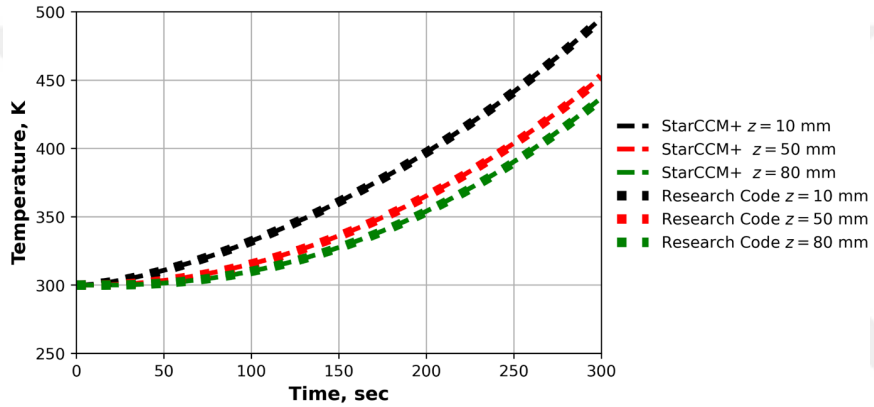


Figure 4.12: Comparison results for fluid temperatures

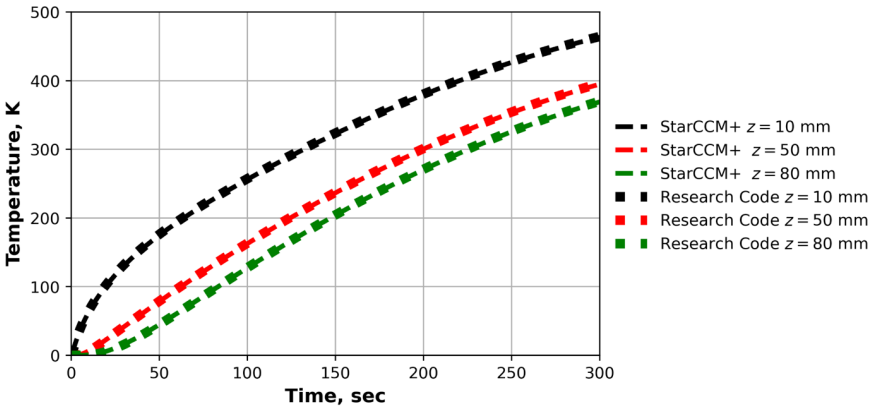


Figure 4.13: Comparison results for temperature differences between the phases

Table 4.5: L_∞ error norms for verification of two-equation model

Error Norm	T_{10mm}	T_{50mm}	T_{80mm}
$L_{\infty,s}$, %	0.148	0.103	0.489
$L_{\infty,f}$, %	0.156	0.108	0.039

4.3.4 Creation of $B^{'}$ Tables

In thermo-chemical ablation model, surface mass balance must be solved in conjunction with in-depth governing equations and surface energy balance equation to determine the surface recession rate at the ablating surface. The traditional method is to use the so-called $B^{'}$Table that gives the non-dimensional consumption rate of the material as a function of non-dimensional pyrolysis gas mass flux, wall temperature and pressure. Surface mass balance phenomenon, non-dimensional mass fluxes and the corresponding balance equation are addressed in Section 2.2. The surface mass balance equation is given as:

$$\rho_e u_e C_m Y_{i,e} + \dot{m}^{''}_{ch} Y_{i,ch} + \dot{m}^{''}_{pg} Y_{i,pg} = (\dot{m}_{ch} + \dot{m}_{pg} + \rho_e u_e C_m) Y_{i,w} \tag{4.57}$$

Eq. 4.57 can be written in terms of non-dimensional mass fluxes as:

$$Y_{i,e} + B^{'}_{ch} Y_{i,ch} + B^{'}_{pg} Y_{i,pg} = (B^{'}_{ch} + B^{'}_{pg} + 1) Y_{i,w} \tag{4.58}$$

where $B^{'}_{ch} = \dot{m}_{ch}/\rho_e u_e C_m$ and $B^{'}_{pg} = \dot{m}_{pg}/\rho_e u_e C_m$ are the non-dimensional mass fluxes of the char and pyrolysis gases, respectively. Eq. 4.58 can be re-written as:

$$B^{'}_{ch} = \frac{B^{'}_{pg}(Y_{i,pg} - Y_{i,w}) + (Y_{i,e} - Y_{i,w})}{Y_{i,ch} - Y_{i,w}} \tag{4.59}$$

In Eq. 4.59, $B^{'}_{ch}$ and $Y_{i,w}$ are unknown quantities provided that the composition of the pyrolysis gases and char are known. Composition of the pyrolysis gases depends on the chemical model used such as *frozen* and *chemical equilibrium* and is determined inside the research code, and in general char is assumed to be pure carbon. $Y_{i,w}$ can be calculated assuming equilibrium chemistry as long as species list, temperature and pressure are provided. Then, the non-dimensional mass flux of char, $B^{'}_{ch}$, can be

calculated using Eq. 4.59. Once $B_{ch}^{'}$ is known, the thermo-chemical erosion rate, $\dot{s}$, can be evaluated as:

$$\dot{s} = \frac{B_{ch}^{'} \rho_e u_e C_m}{\rho_{ch}} \tag{4.60}$$

For the TACOT material, a list of 25 species (C; H; O; N; CH_4; CN; CO; CO_2; C_2; C_2H; $C_2H_2, acetylene$; C_3; C_4; $C_4H_2, butadiyne$; C_5; HCN; H_2; H_2O; N_2; CH_2OH; CNN; CNC; $CNCOCN$; C_6H_6; HNC) is defined along with solid graphite, $C(gr)$, for equilibrium calculations in Cantera. At the edge of the boundary layer, elemental mole fractions of O/N : $0.21/0.79$ are defined. For the pyrolysis gas mixture, elemental mole fractions of $C/H/O$: $0.206/0.679/0.115$ are used. $B_{ch}^{'}$ and h_w are evaluated in the temperature range of 250 – 3500 K for six different non-dimensional pyrolysis mass flux values of 10, 3, 1, 0.6, 0.2, and 0.1.

Figure 4.14 and Figure 4.15 compare the absolute wall enthalpy, h_w, and non-dimensional mass flux of the char, $B_{ch}^{'}$, values to those provided in [77], respectively. It is clear that an exact match is obtained.

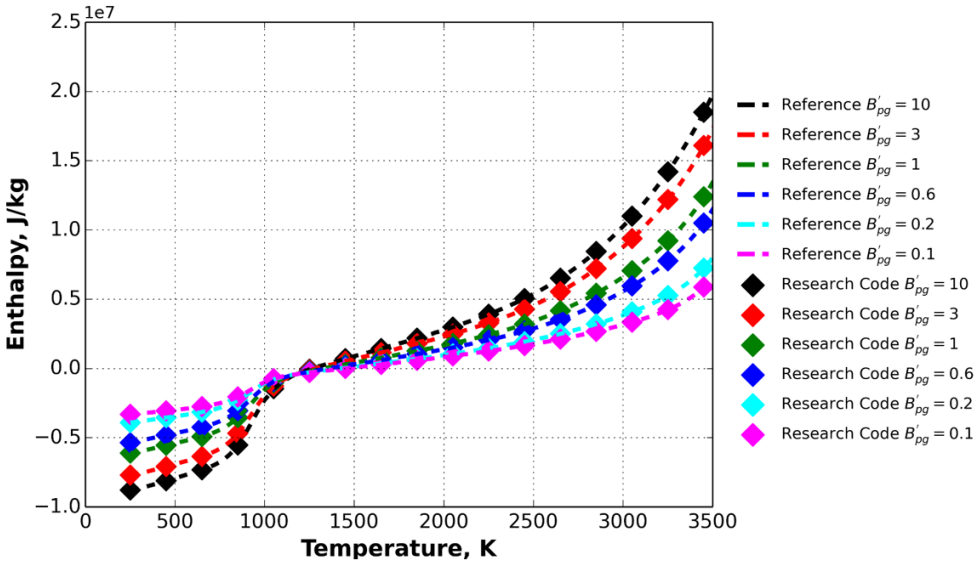


Figure 4.14: Comparison results for wall enthalpy, h_w

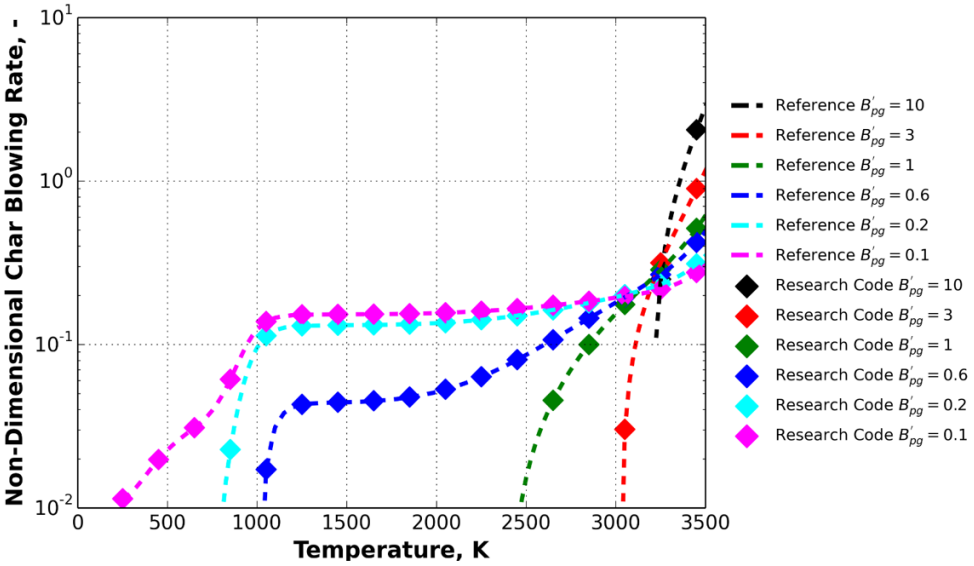


Figure 4.15: Comparison results for non-dimensional char mass flux, B'_{ch}

4.3.5 Comparison with Arc-Jet Test Data

The aim of this validation study is to assure that the developed numerical tool is capable of replicating real response of charring ablative materials. For this purpose, arc-jet test data of PICA is compared with those estimated using the research code. PICA is a lightweight charring ablative material developed at NASA Ames Research Center, and it is made of carbon-fiber impregnated with phenolic resin. Although there exist several works regarding its microstructure and arc-jet test data in the literature, complete material model of PICA is not publicly available. However, TACOT relies on open-literature data of PICA and is similar regarding elemental composition [114]. Then, it is expected that TACOT serves as a stand-in for PICA. Therefore, in this validation study, TACOT material model is used to simulate the thermal response of PICA in arc-jet environment as done in [115].

Arc-jet tests have been frequently used for characterization and performance assessment of ablative materials. For PICA, multiple arc-jet tests were carried out at NASA Ames Research Center and test results were documented in [116]. Surface temperature of the PICA samples was recorded using optical pyrometer whose uncertainty was approximately 5%. In-depths temperatures were measured using thermocouples. At the end of each test, the surface recession was measured using calipers with un-

certainty of $\pm 0.5\ mm$.

Table 4.6: Parameters for the selected arc-jet test case

q''_{cw}, W/m^2	h_{stag}, J/kg	p_{stag}, kPa	Argon Mass Fraction	Exposure Time, s
3.95×10^6	2.28×10^7	17.2	0.08	34.0

One arc-jet test dataset is selected for this validation study. Parameters of the selected arc-jet test are given in Table 4.6. In order to simulate the arc-jet test, recovery enthalpy, h_r, of arc-jet stream and heat transfer coefficient between arc-jet stream and material, $\rho_e u_e C_h$, have to be defined as boundary condition. The recovery enthalpy is equal to the stagnation enthalpy, h_{stag}, of the arc-jet stream. It is a known value as it was estimated by the facility and is given in Table 4.6. The heat transfer coefficient is an unknown parameter, however, since the cold wall heat flux value, q''_{cw}, on the surface was measured using slug-calorimeter, the heat transfer coefficient can be estimated. The heat transfer coefficient can be expressed as:

$$\rho_e u_e C_h = \frac{q''_{cw}}{h_r - h_w} \tag{4.61}$$

To evaluate the heat transfer coefficient using Eq. 4.61, the wall enthalpy, h_w, must be determined. To do that, the following approach is adopted. The arc-jet stream is composed of partly dissociated air with additional argon (Ar). In this case, the mass fraction of Ar is 0.08. The arc-jet stream is assumed to be in chemical equilibrium at the surface. Using Cantera, equilibrium composition of dissociated air with argon is determined at the cold wall temperature of $300.0\ K$. The corresponding wall enthalpy is evaluated as $1706.3\ J/kg$. Then, the heat transfer coefficient is calculated as $0.173\ kg/(m^2 \cdot s)$.

Figure 4.16 compares the predicted temperature histories on the surface and at three depths inside the material with arc-jet test data. Table 4.7 compares the estimated total surface recession with the measured value at the end of the arc-jet test. It is seen that the predicted surface temperature and total surface recession are in good agreement with test data. General trends in in-depth temperatures fairly match, as well. Considering the uncertainties associated with material modeling and experimental data,

it can be stated that the research code can be used reliably to estimate the thermal response of charring ablative materials.

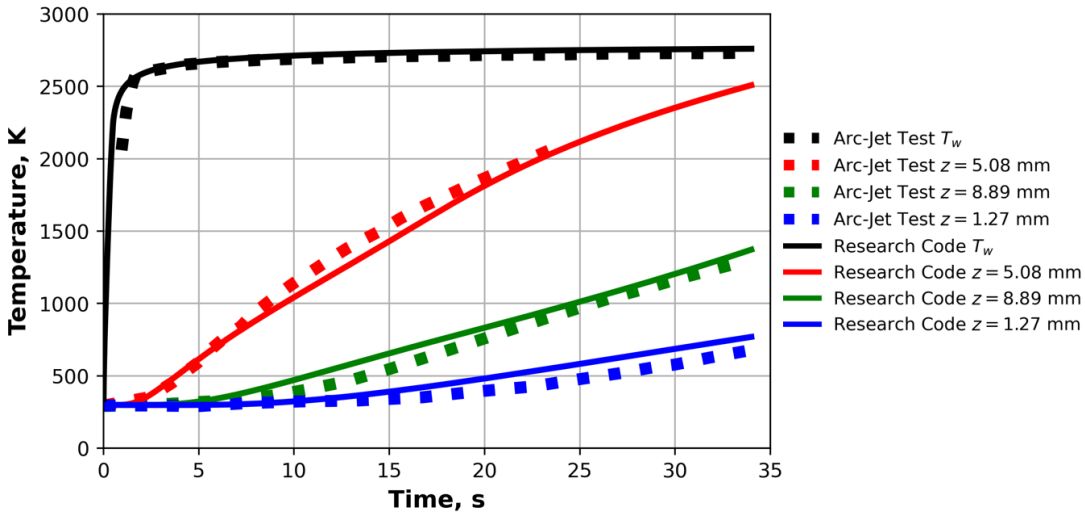


Figure 4.16: Comparison of temperatures on the surface and at three depths

Table 4.7: Comparison of total surface recession

Arc-Jet Test, mm	Research Code, mm	Error, $\%$
4.43	4.10	7.45

CHAPTER 5

SIMULATION RESULTS

As described in the previous chapters, response of charring ablative materials can be estimated under various assumptions and different complexity levels and in the context of this work a numerical framework that enables modeling of charring ablative materials at different degrees of fidelity is developed. This chapter is devoted to the investigation of the effects of modeling assumptions on the thermal response of a charring ablative material. First, effects of chemical non-equilibrium under local thermal equilibrium assumption is addressed. Then, influence of both thermal and chemical non-equilibrium on the thermal response of charring ablatives are examined. In addition, effects of pore structure parameters, i.e. porosity and permeability, on the outcome of the thermal and chemical non-equilibrium solutions are explored.

Numerical simulations are performed for two test cases provided by ablation modeling workshops. Test cases are denoted as *Case 1* and *Case 2* and described in section 3.2.6 and 3.2.7, respectively. In the first test case, a sample of $0.05\ m$ fictitious Theoretical Ablative Composite for Open Testing (TACOT) material, initially at $298\ K$, is heated on one side at $1644\ K$ for $45\ s$ at atmospheric pressure, and adiabatic boundary condition is set on the other (back) surface. No surface recession is allowed. In the second case, a sample of $0.05\ m$ thick fictitious material TACOT, initially at $300\ K$, is heated on one side by thermo-chemical convection at atmospheric pressure and surface recession is allowed. The heat transfer coefficient is ramped from zero to $0.3\ kg/(m^2 \cdot s)$ at $0.1\ s$, and then held constant for $45\ s$. The corresponding recovery enthalpy is $1.5 \times 10^6\ J/kg$. Adiabatic boundary condition is set on the back surface.

Pyrolysis gas mixture of the TACOT material that contains 11 species (see Table 4.1) are used in all simulations. In frozen flow simulations, the initial chemical compo-

sition of the pyrolysis gas mixture is kept constant throughout the simulations. In the simulations where chemical equilibrium is assumed, pyrolysis gas mixture inside each control volume is equilibrated under local gas temperature and pressure at every time step. In the simulations where finite rate chemistry is taken into account, reaction mechanism proposed by April et al. [117] and given in Table 5.1 is taken as basis. However, the 5^{th} reaction is omitted since it is a zero-order reaction which yields unrestricted consumption of C and H_2. This unreasonable behavior is also reported in [118, 119] and gives rise to negative mass fractions during simulations.

Table 5.1: Reaction mechanism for pyrolysis gases between $535\ K$ and $1925\ K$ [117]

#	Reaction Formula	Rate Law	E_a, $kcal/mol$	Z	ϑ
1	$CH_4 \rightarrow 0.5H_2 + 0.5C_2H_6$	$k[A]$	95.0	7.6×10^{14}	0
2	$C_2H_6 \rightarrow C_2H_4 + H_2$	$k[A]$	70.0	3.1×10^{14}	0
3	$C_2H_4 \rightarrow C_2H_2 + H_2$	$k[A]$	40.0	2.6×10^{8}	0
4	$C_2H_2 \rightarrow 2C + H_2$	$k[A]^2$	10.0	2.1×10^{10}	0
5	$C + 2H_2 \rightarrow CH_4$	k	17.0	2.0×10^{9}	0
6	$C_6H_5OH + H_2 \rightarrow H_2O + C_6H_6$	$k[A]$	45.0	2.0×10^{13}	0
7	$C_6H_6 \rightarrow 3C_2H_2$	$k[A]$	35.0	1.4×10^{9}	0
8	$C + H_2O \rightarrow CO + H_2$	$k[A][B]$	82.0	1.2×10^{12}	1
9	$CO + H_2O \rightarrow CO_2 + H_2$	$k[A][B]$	30.0	1.0×10^{12}	0
10a	$C + CO_2 \rightarrow 2CO$	$k[A]$	50.0	1.0×10^{6}	1
10b	$2CO \rightarrow C + CO_2$	$k[A]^2$	61.0	1.0×10^{-9}	0

Thermal non-equilibrium is the default mode of the developed code and volumetric heat transfer coefficient is calculated using Eq. 4.5. In order to obtain results under the local thermal equilibrium assumption, the volumetric heat transfer coefficient between the phases is set to a sufficiently high value, i.e. $1 \times 10^{15}\ W/(m^3 \cdot K)$. All simulations are carried out using 100 elements with a cell growth rate of 1.02 and time step of $0.01\ s$. Results of the grid independence study are given in Appendix C.

5.1 Effects of Chemical Non-equilibrium under Local Thermal Equilibrium Assumption

In this section, results of the numerical simulations with three different chemistry models under local thermal equilibrium assumption are presented to distinguish the sole effects of chemical reactions on the response of lightweight ablative materials.

Figure 5.1 compares the temperature variations at five in-depth locations for frozen, equilibrium, and finite-rate chemistry models for Case 1 in which no surface recession is allowed. It is clear that temperatures calculated with equilibrium chemistry assumption are always apparently lower than those calculated with frozen flow assumption except at the depth of $16\ mm$. The difference can be attributed to the difference in the internal energies of the pyrolysis gas mixtures. The internal energy of the equilibrated pyrolysis gas mixture increases sharply at certain temperature ranges, i.e. approximately $650 - 1000\ K$ and $1200 - 1600\ K$, as shown in Figure 5.2 compared to the frozen mixture value. This also leads to considerable difference in the specific heats at certain temperature ranges. Thus, pyrolysis gas mixture in chemical equilibrium absorbs more heat to increase its temperature compared to the frozen flow. As the distance from the front surface increases, the gap between the temperature solutions initially gets larger. The maximum temperature difference at the end of the simulation is approximately $51\ K$, i.e. 4.38% of the solution obtained under chemical equilibrium assumption for the depth of $4\ mm$. Temperature gap between the solutions seems to be diminishing at the depth of $8\ mm$ to $39.5\ K$; however, on percent scale it is 4.6% of the solution obtained under chemical equilibrium assumption. At the depth of $16\ mm$ the temperature difference between the solutions is small, i.e. around $1\ K$. This somewhat unanticipated outcome might be related to the relative closeness of the specific heats of the pyrolysis gas mixtures below $600\ K$. Most probably, at further depths the temperature gap between the solutions is also negligible.

Sharp increases in the internal energy of the equilibrated pyrolysis gas mixture results from the substantial change in species concentration, i.e. species mass fractions, at certain temperature regions as shown in Figure 5.3. As temperature changes from $650\ K$ to $1000\ K$, mole fractions of CH_4, CO_2 and H_2O reduce considerably whereas

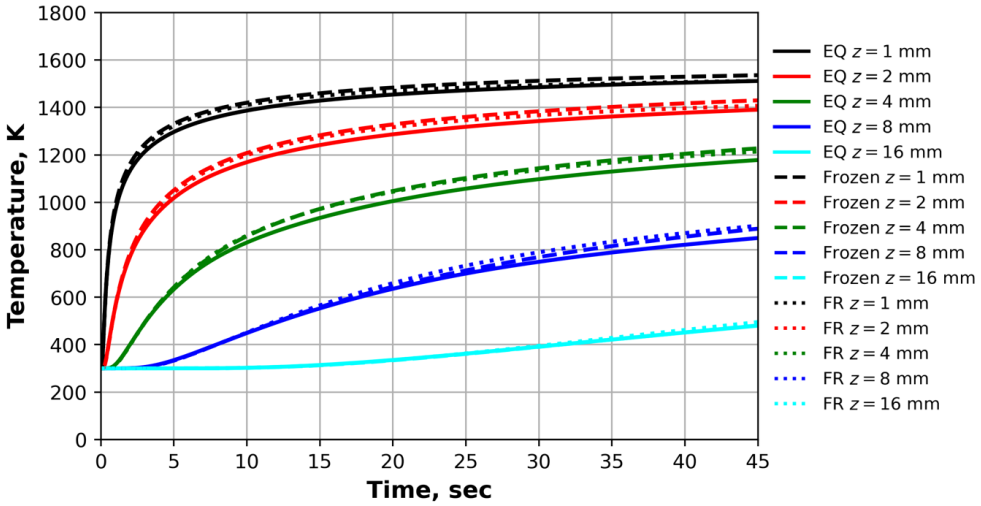


Figure 5.1: Temperature solutions obtained using equilibrium (EQ), frozen and finite-rate (FR) chemistry models for Case 1

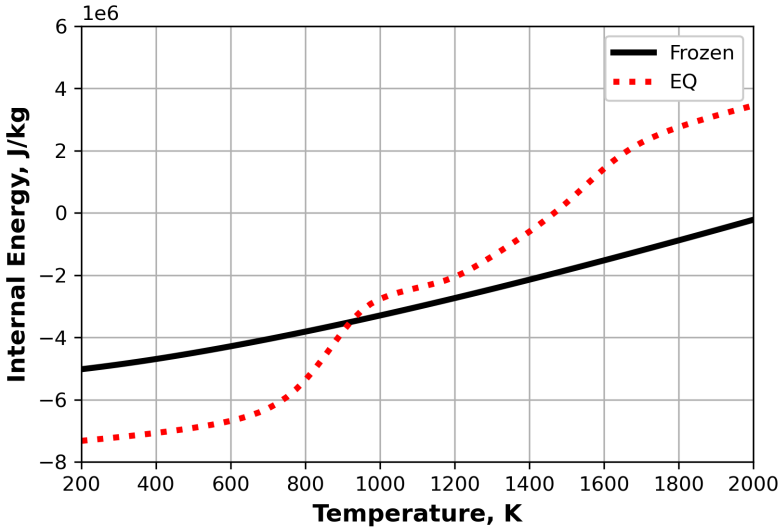


Figure 5.2: Variation of internal energies of the pyrolysis gas mixture for frozen and chemical equilibrium conditions

mole fractions of H_2 and CO rise. The second temperature region in which the internal energy of the equilibrated pyrolysis gas mixture changes rapidly corresponds to the conversion of CH_4 to H_2 and C_2H_2. Rapid changes in internal energy leads to large humps in specific heat values, as well.

Temperatures predicted under the finite-rate chemistry assumption are initially very

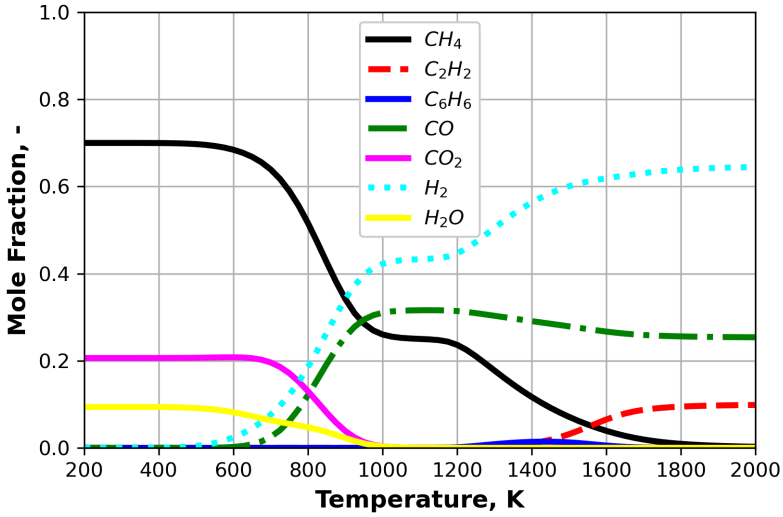


Figure 5.3: Equilibrium mole fraction variations of pyrolysis gas species as a function of temperature

close to those predicted with the frozen flow assumption at depths close to the front surface. Nevertheless, as time progresses they tend to shift towards the equilibrium solution. This result preliminary suggests that the reactions given in Table 5.1 are overall endothermic. Enthalpy of reactions, Δh_R, are given in Table 5.2 at two different temperature. The negative sign indicates that heat is released, i.e. the reaction is exothermic. It is clear that all reactions are not endothermic. At the depths of 8 and 16 mm, the finite-rate solution starts to give higher temperatures than frozen flow solution. It is difficult to compare the net contribution of each reaction, but a possible explanation may be that at relatively lower temperatures the dominant reactions are not endothermic but exothermic.

Figure 5.4 provides the variations in the depths of the pyrolysis and char fronts, defined as 98% and 2% virgin material, respectively, for Case 1. It is obvious that chemical equilibrium assumption yields lower depths of pyrolysis and char fronts. This result supports the lower temperature predictions already presented as lower temperatures retard the decomposition process and lead to lesser depths for the pyrolysis and char fronts. At the end of the simulation time, the difference between the frozen and equilibrium solutions for the pyrolysis and char fronts are 0.10 mm and 0.32 mm, respectively. The finite-rate solution yields higher depth for the pyrolysis

Table 5.2: Enthalpy of reactions at $550\ K$ and $1600\ K$

#	Reaction Formula	$\Delta h_{R,550K},\ J/kg$	$\Delta h_{R,1600K},\ J/kg$
1	$CH_4 \rightarrow 0.5H_2 + 0.5C_2H_6$	3.4325×10^7	3.6515×10^7
2	$C_2H_6 \rightarrow C_2H_4 + H_2$	1.4037×10^8	1.4215×10^8
3	$C_2H_4 \rightarrow C_2H_2 + H_2$	1.8201×10^8	1.8689×10^8
4	$C_2H_2 \rightarrow 2C + H_2$	1.2101×10^9	1.2139×10^9
5	$C_6H_5OH + H_2 \rightarrow H_2O + C_6H_6$	-6.6972×10^7	-7.7453×10^7
6	$C_6H_6 \rightarrow 3C_2H_2$	6.1055×10^8	6.0486×10^8
7	$C + H_2O \rightarrow CO + H_2$	-5.8455×10^8	-5.8354×10^8
8	$CO + H_2O \rightarrow CO_2 + H_2$	-3.9356×10^7	-2.9407×10^7
9a	$C + CO_2 \rightarrow 2CO$	-5.4519×10^8	-5.5413×10^8
9b	$2CO \rightarrow C + CO_2$	5.4519×10^8	5.5413×10^8

front compared to the frozen and equilibrium solutions. This finding indicates higher temperature predictions and supports the aforementioned statement that exothermic reactions become dominant at relatively low temperatures. For the char front, the finite rate solution lies between the frozen and equilibrium flow solutions, as expected.

Figure 5.5 compares the temperature variations at the front surface and different locations inside the ablative material using the frozen, equilibrium, and finite-rate chemistry models for Case 2 in which surface recession is calculated using the conventional $B^{'}$ method. Maximum temperature differences between the solutions are given in Table 5.3. It is seen that surface temperature, T_w, and temperatures at depths of 1 and $2\ mm$ are almost identical to each other. Maximum temperature differences at these locations are less than 2%. Nevertheless, at depth of 4 and $8\ mm$ it is observable that temperature difference between the equilibrium solution and other two solutions begins to increase at about $600\ K$, reaches its peak at around $1000\ K$ and then the solutions tend to become closer as the surface recesses and location approaches to the

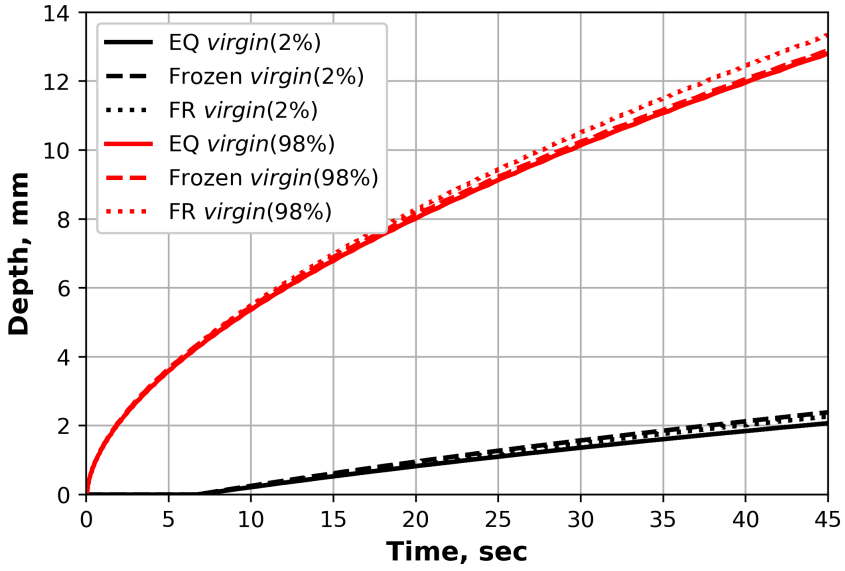


Figure 5.4: Pyrolysis and char fronts for Case 1

surface. Although it is unnoticeable, this behavior might also take place at all depths, too. This behavior might also be related to the differences in specific heats of the pyrolysis gas mixtures as they are considerably different between 650 and 1000 K.

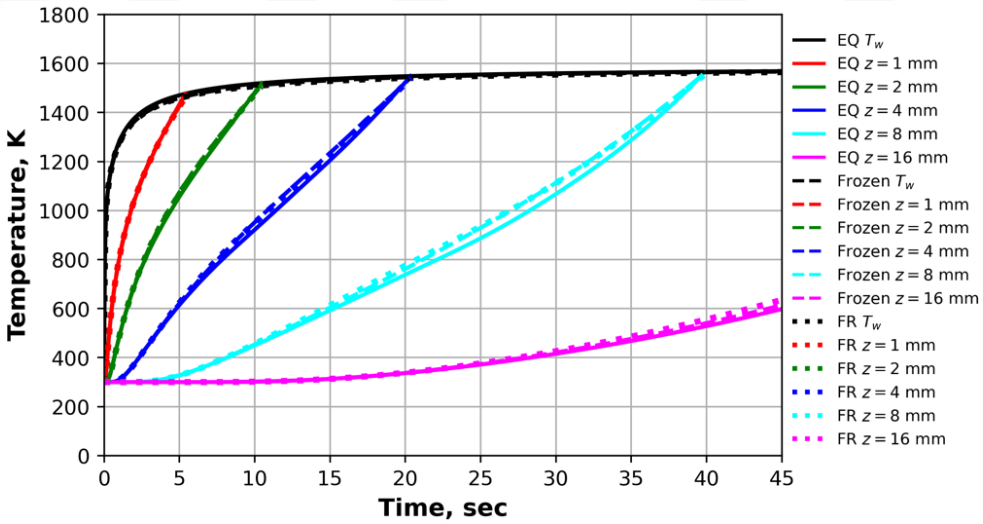


Figure 5.5: Temperature solutions obtained using equilibrium (EQ), frozen and finite-rate (FR) chemistry models for Case 2

Figure 5.6 shows the variations in the depths of the pyrolysis and char fronts for

Table 5.3: Maximum temperature differences for Case 2

Temperature Difference	z_{1mm}	z_{2mm}	z_{4mm}	z_{8mm}	z_{16mm}
$max\left(\frac{T_{frozen}-T_{EQ}}{T_{frozen}}\right)$, %	0.65	1.74	3.23	4.65	2.6
$max\left(\frac{T_{frozen}-T_{FR}}{T_{frozen}}\right)$, %	0.46	0.59	−0.51	−1.81	−3.52

Case 2. It is worth noting that char front corresponds to the surface recession, as well. Similar to Case 1, chemical equilibrium assumption yields lower depth of pyrolysis front; however, all chemical models yield almost equivalent depths for the char front. It can thus be inferred that the chemistry model does not have substantial influence on the surface recession rate.

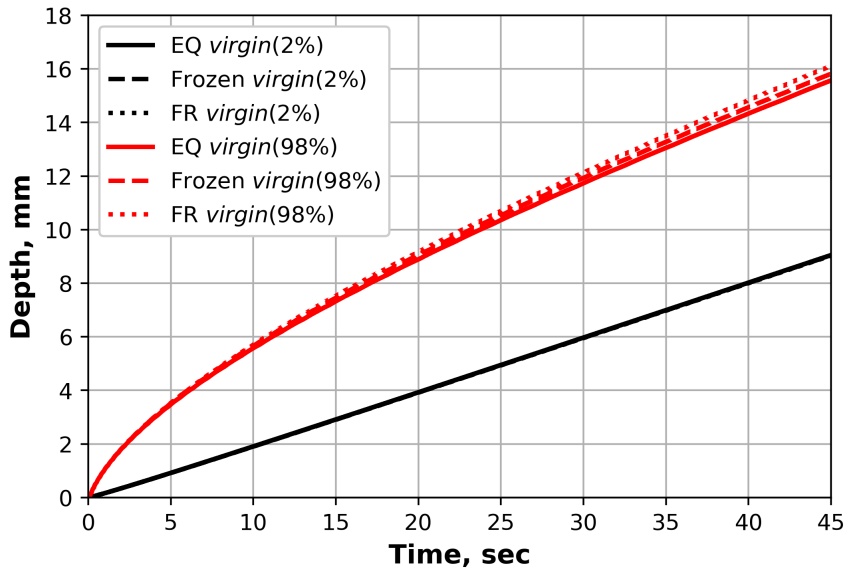


Figure 5.6: Pyrolysis and char fronts for Case 2

Figure 5.7 compares the mole concentrations of major species, i.e. CH_4, C_2H_2, CO, CO_2, and H_2, injected to the boundary layer predicted by finite-rate solutions for Case 1 and Case 2. Mole fractions for other species are not shown due to their very low concentrations. It is rather surprising that while the species mole fractions vary considerably over time for Case 1, their variation becomes negligible as time advances for Case 2. This can be explained as follows. When the front surface is stationary, i.e.

in Case 1, the char layer becomes thicker with time, and thus pyrolysis gas mixture may undergo further chemical reactions over time. However, when surface recedes, i.e. Case 2, the process advances in a quasi-steady fashion, and thus content of the pyrolysis gas mixture injected to the boundary layer does not change substantially.

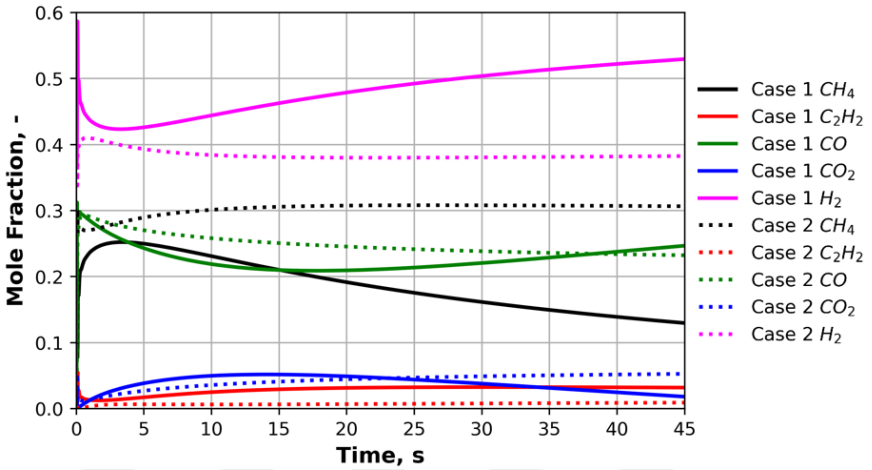


Figure 5.7: Species injected to the boundary layer

5.2 Thermal and Chemical Non-equilibrium

In this section, results of the numerical simulations which take into account local thermal non-equilibrium are presented. Two chemical models are considered: Frozen and finite-rate.

Figure 5.8 demonstrates the temperature differences between the pyrolysis gas mixture and solid phase, i.e. $\Delta T = T_{pg} - T_s$, at different depths for Case 1. It can be deduced that as heat wave penetrates into the ablative material, temperature differences between the pyrolysis gas mixture and solid phase increase. Then, temperatures get closer and local thermal equilibrium is eventually established at all depths. The deeper the location lies, the less temperature difference is observed. This might be attributed to the decreasing intensity of the heat wave. Another possible explanation may be related to the pyrolysis gas production rate. Since local thermal non-equilibrium is much more significant when abrupt changes take place, diminishing changes result in less temperature differences at deeper locations. The impact of the

local thermal non-equilibrium on the solid temperature and the depths of pyrolysis and char fronts are rather negligible, thus they are not plotted for comparison.

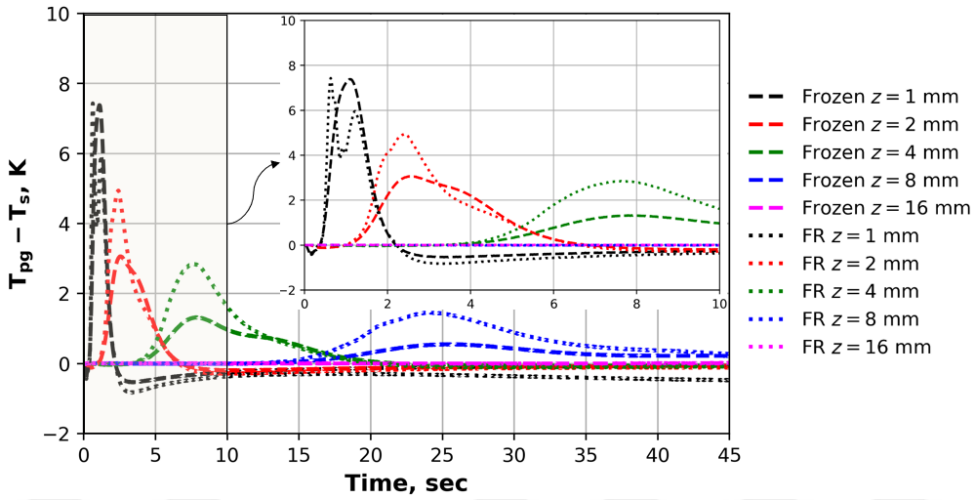


Figure 5.8: Temperature differences between the pyrolysis gas mixture and solid phase at different depths for Case 1

In order to observe the effects of chemical reactions at local thermal non-equilibrium condition more clearly, temperature differences between the pyrolysis gas mixtures are plotted and given in Figure 5.9. Pyrolysis gas mixture temperatures predicted by frozen flow assumption are always higher at depths close to the surface, i.e. $z = 1\ mm$ and $z = 2\ mm$. The differences, first, get larger; then diminish, and finally start to increase again. This may indicate a competition between endothermic and exothermic reactions. At deeper locations, i.e. 8 and $16\ mm$, exothermic reactions become dominant with time as the temperature of pyrolysis gas mixture predicted by the finite-rate model gets larger than frozen flow solution.

Temperature differences between the pyrolysis gas mixture and solid phase for Case 2 are given in Figure 5.10. Since temperatures differ at the front surface, too, they are included in the plot. Evolution of the temperature differences beneath the receding surface are similar to those observed in Case 1. However, while the pyrolysis gas temperature is higher than the solid temperature inside the ablative material, it is lower at the front surface. As the front surface recedes and any location inside the material becomes closer to the front surface, pyrolysis gas temperature at that location begins to be lower than the temperature of the solid. Indeed, this behavior is related to the

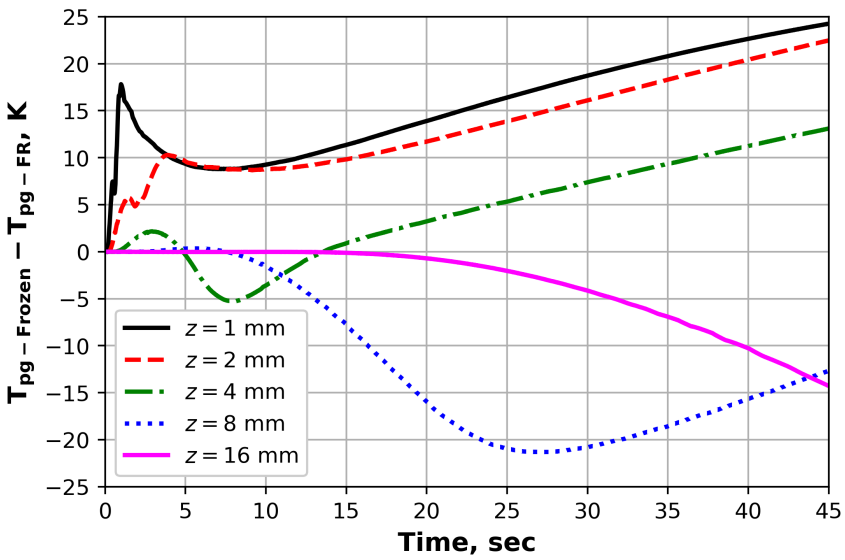


Figure 5.9: Temperature differences between the pyrolysis gas mixtures at different depths for Case 1

application of the boundary conditions. The thermo-chemical convection is applied only to the solid phase, i.e. pyrolysis gas mixture is adiabatic at the receding surface. Pyrolysis gas mixture is heated by the solid phase and thus its temperature is always lower than the temperature of the solid phase at locations very close to the receding surface. However, combined effects of advection and diffusion make the pyrolysis gas temperature higher than the solid temperature inside the material. The impact of the local thermal non-equilibrium on the surface recession, solid temperature and the depths of pyrolysis and char fronts are not significant, thus they are not given for comparison.

Temperature differences between the pyrolysis gas mixtures obtained under different chemistry models is given in Figure 5.11. Beneath the receding surface, the differences fluctuate over time getting larger and smaller. As stated above, a possible explanation might be that a competition between endothermic and exothermic reactions takes place. At the receding surface, the temperature difference between the pyrolysis gas mixtures approximates to the constant value of $2.4\ K$ after $30\ s$. The constant temperature difference after $30\ s$ might imply that both solutions reach a quasi-steady form.

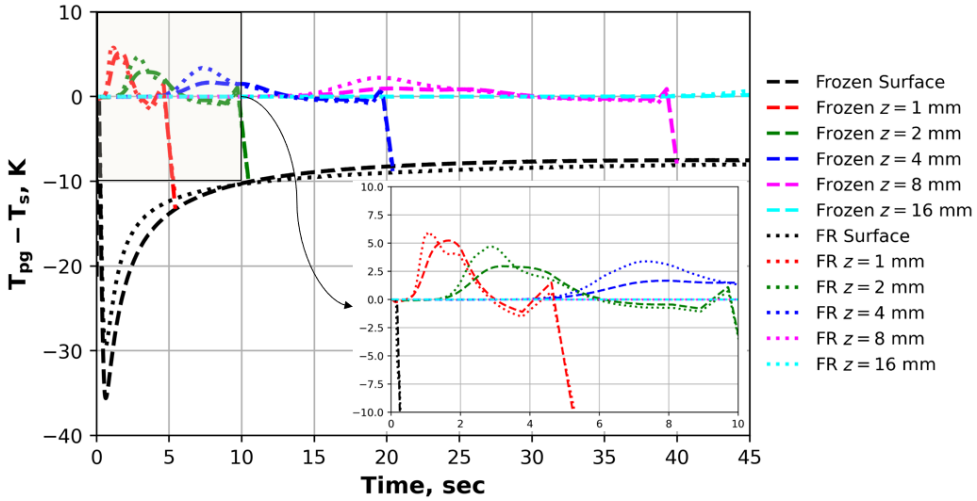


Figure 5.10: Temperature differences between the pyrolysis gas mixture and solid phase at different depths for Case 2

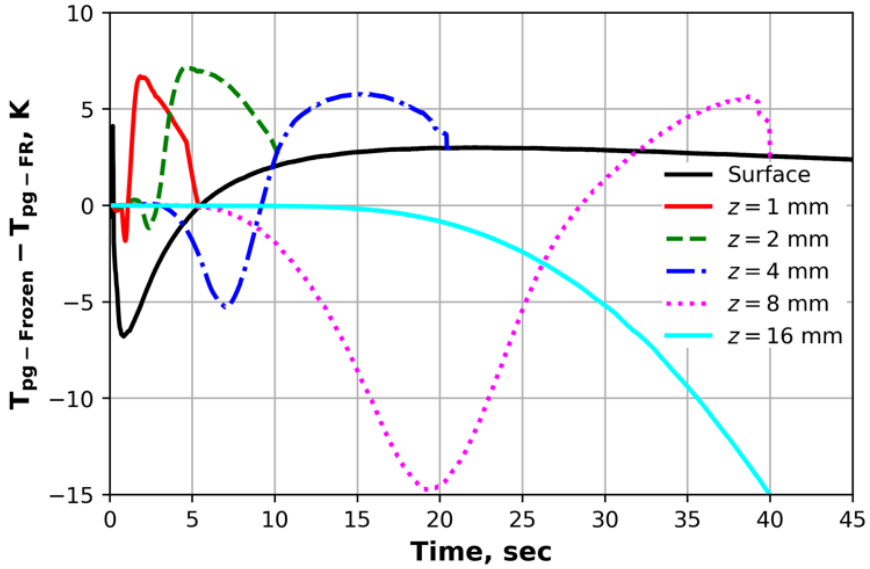


Figure 5.11: Temperature differences between the pyrolysis gas mixtures at different depths for Case 2

5.3 Effects of Material Properties

In this section, influences of pore structure parameters, i.e. porosity and permeability, on the thermal and chemical non-equilibrium solutions are examined for Case 1 in which the front surface is stationary. Porosity is the fraction of the bulk volume of

the fluid phase, i.e. pyrolysis gas mixture, and it directly affects the effective density of the solid, effective thermal conductivities and flow velocity. Permeability is the measure of the flow conductance of the porous medium, and it is directly related to the flow velocity inside the medium. Porosity and permeability are the main macroscopic pore structure parameters that may have considerable effects on the thermal response of the porous ablative materials.

Although porosity and permeability are somewhat correlated, these pore structure parameters are perturbed independently in order to observe the sole effect of each parameter. The parameter test matrices for the porosity and permeability are given in Table 5.4 and Table 5.5, respectively.

Table 5.4: Test matrix for porosity

Perturbation	ϵ_v	ϵ_{ch}
-10%	0.72	0.765
Baseline	0.8	0.85
$+10\%$	0.88	0.935

Table 5.5: Test matrix for permeability

Perturbation	κ_v, m^2	κ_{ch}, m^2
$0.2\times$ Baseline	3.2×10^{-12}	4.0×10^{-12}
Baseline	1.6×10^{-11}	2.0×10^{-11}
$5\times$Baseline	0.8×10^{-10}	1.0×10^{-10}

5.3.1 Porosity

Porosity of the initial virgin material is perturbed from the baseline value of 0.80 to 0.72 and 0.88 while keeping the permeability of the virgin and char at the baseline

values. Char porosity value is also perturbed accordingly. Simulations are carried out for two chemical models, i.e. frozen and finite-rate, as thermal non-equilibrium between the phases is taken into account.

Figure 5.12 demonstrates the temperature variations of the solid and frozen pyrolysis gas mixture at different depths with varying porosity levels. The plots suggest that lower porosity level leads to an increase in the both solid and gas temperatures at all depths throughout the simulation time. While a 10% reduction in porosity yields relatively close solid temperatures to the baseline values, a 10% increase in porosity gives much more considerably difference from the baseline values. Table 5.6 gives the maximum temperature differences from the baseline solution for frozen flow. The results may be attributed to the increasing thermal resistance of the charring ablative materials with porosity level. Similar to the solid temperatures, higher porosity levels yield lower gas temperatures at all depths throughout the simulation time.

Table 5.6: Maximum temperature differences from the baseline solution for frozen flow

Temperature Difference	z_{1mm}	z_{2mm}	z_{4mm}	z_{8mm}	z_{16mm}
$max\left(\frac{T_{s,072}-T_{s,080}}{T_{s,080}}\right),\ \%$	2.4	2.9	3.4	3.8	2.4
$max\left(\frac{T_{pg,072}-T_{pg,080}}{T_{pg,080}}\right),\ \%$	10.7	7.4	5.5	4.6	2.4
$max\left(\frac{T_{s,088}-T_{s,080}}{T_{s,080}}\right),\ \%$	-6.3	-7.6	-8.7	-9.4	-5.3
$max\left(\frac{T_{pg,088}-T_{pg,080}}{T_{pg,080}}\right),\ \%$	-6.7	-7.6	-8.7	-9.4	-5.3

Figure 5.13 gives the differences between the frozen pyrolysis gas mixture and solid phase, i.e. $\Delta T = T_{pg} - T_s$, at different depths for varying porosity levels. Similar to the results presented in Section 5.2, initially temperature differences between the pyrolysis gas mixture and solid phase increase. Then, temperatures get closer and local thermal equilibrium is eventually established at all depths. The higher the porosity is, the shorter time is required to reach the local thermal equilibrium condition. As the porosity decreases, temperature difference between the phases becomes

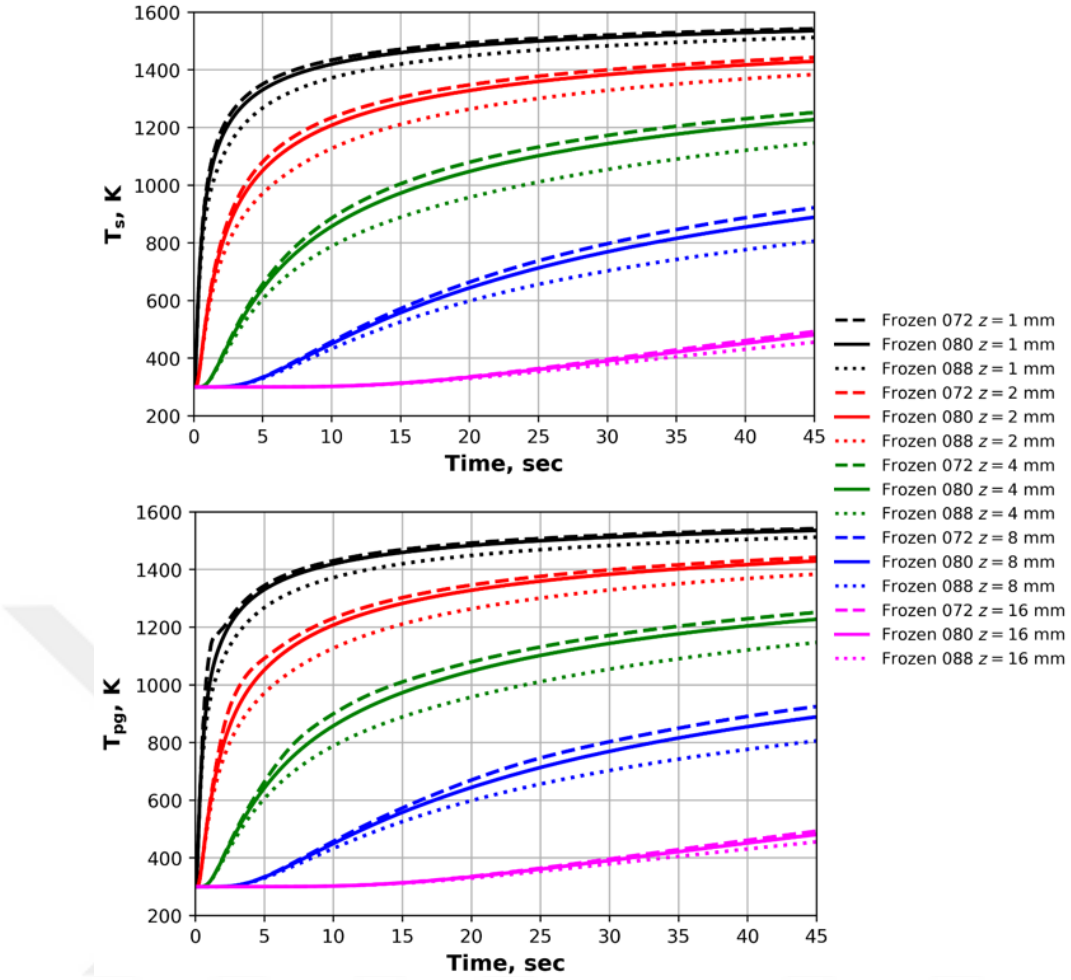


Figure 5.12: Effects of porosity on solid and frozen pyrolysis gas mixture temperatures

more notable. Porosity level of 0.88 leads to local thermal equilibrium from the very beginning of the simulation. The estimated volumetric heat transfer coefficients at different locations are plotted in Figure 5.14. It is obvious that increasing porosity leads to order of magnitude increase in volumetric heat transfer coefficient. That's why solutions with higher porosity values converge to local thermal equilibrium solutions rapidly. The results suggest that volumetric heat transfer coefficient is very sensitive to the porosity level. It can also be deduced that local thermal equilibrium solution is sufficient when porosity is higher than 0.80.

Figure 5.15 shows the variations in the depths of the pyrolysis and char fronts along with pyrolysis gas mixture blowing rates under frozen flow assumption. As expected,

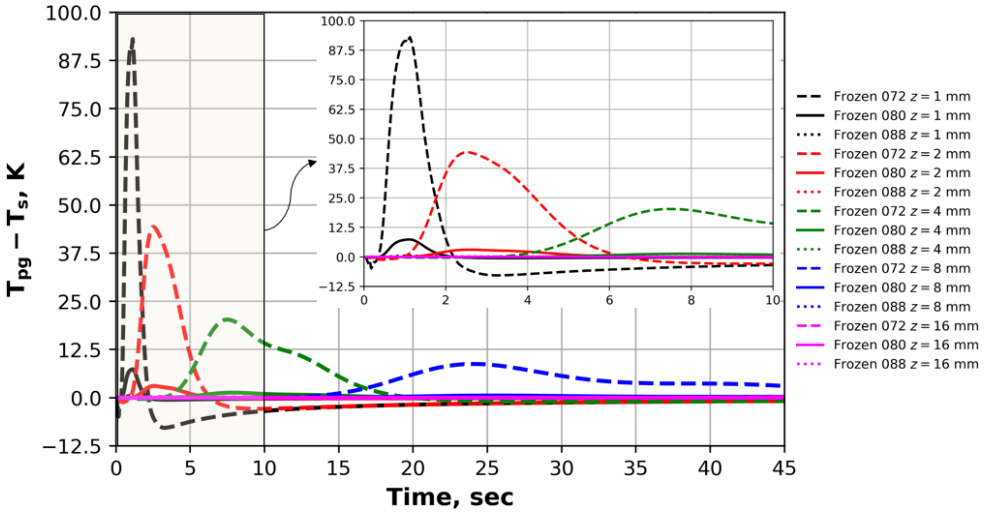


Figure 5.13: Temperature differences between the frozen pyrolysis gas mixture and solid phase at different depths for varying porosity values

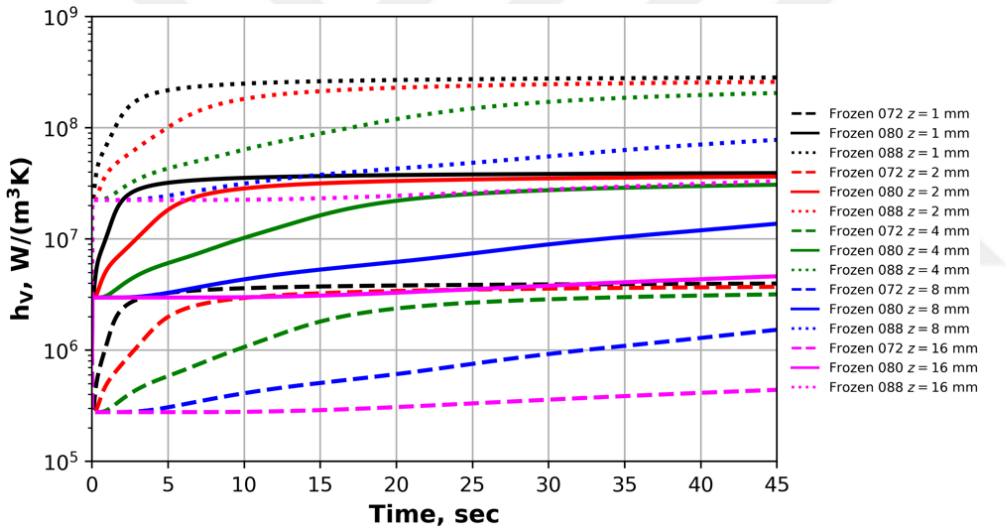


Figure 5.14: Volumetric heat transfer coefficient between the frozen pyrolysis gas mixture and solid at different depths for varying porosity values

a negative correlation exists between the porosity level and depths for pyrolysis and char fronts owing to decreasing temperature with porosity level. As the porosity level decreases, more pyrolysis gases are injected to the boundary layer. Two factors contribute to the rise in blowing rate. First, as stated above, lower porosity levels result in higher temperatures inside the ablative materials and this accelerates the thermal decomposition process. Secondly, density of the virgin material gets larger

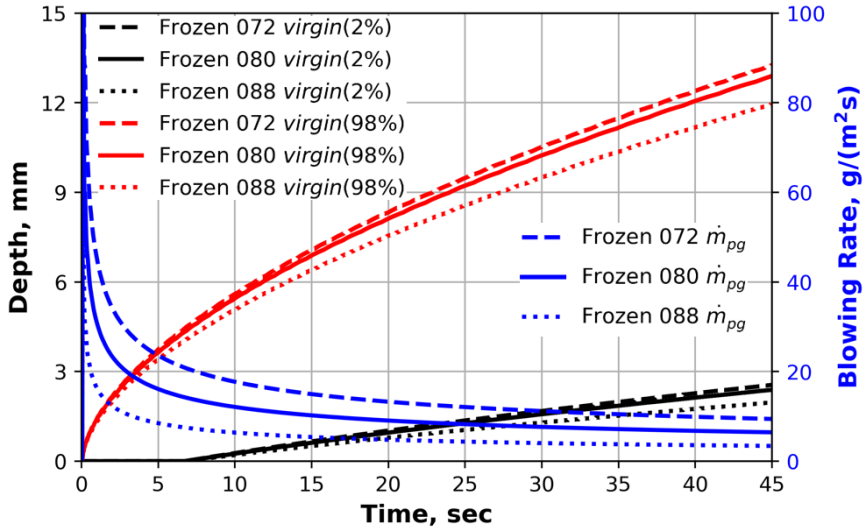


Figure 5.15: Effects of porosity on blowing rates and pyrolysis and char fronts for frozen flow

as porosity of the material reduces. In other words, there exists more virgin material that can thermally decompose and produce more pyrolysis gases as porosity of the material reduces.

Figure 5.16 demonstrates the temperature variations of the solid and pyrolysis gas mixture at different depths with varying porosity levels when chemical reactions are taken into considerations. Table 5.7 gives the maximum temperature differences from the baseline solution. The results are in accordance with the results of the frozen flow solutions as the lower the material porosity is, the higher solid and gas temperatures at all depths are observed.

Figure 5.17 shows the variation of the differences between the pyrolysis gas mixture and solid phase, i.e. $\Delta T = T_{pg} - T_s$, at different depths obtained through finite-rate solutions. Similar to the results already presented for frozen flow, initially temperature differences between the pyrolysis gas mixture and solid phase increase and, then, temperatures get closer. Higher porosity level fosters the local thermal equilibrium between the phases. The estimated volumetric heat transfer coefficients at different locations are plotted in Figure 5.18. Compared to the frozen flow solutions, the volumetric heat transfer coefficients are, in general, relatively lower which induce higher temperature differences between the phases. The reason for this is not clear, but it

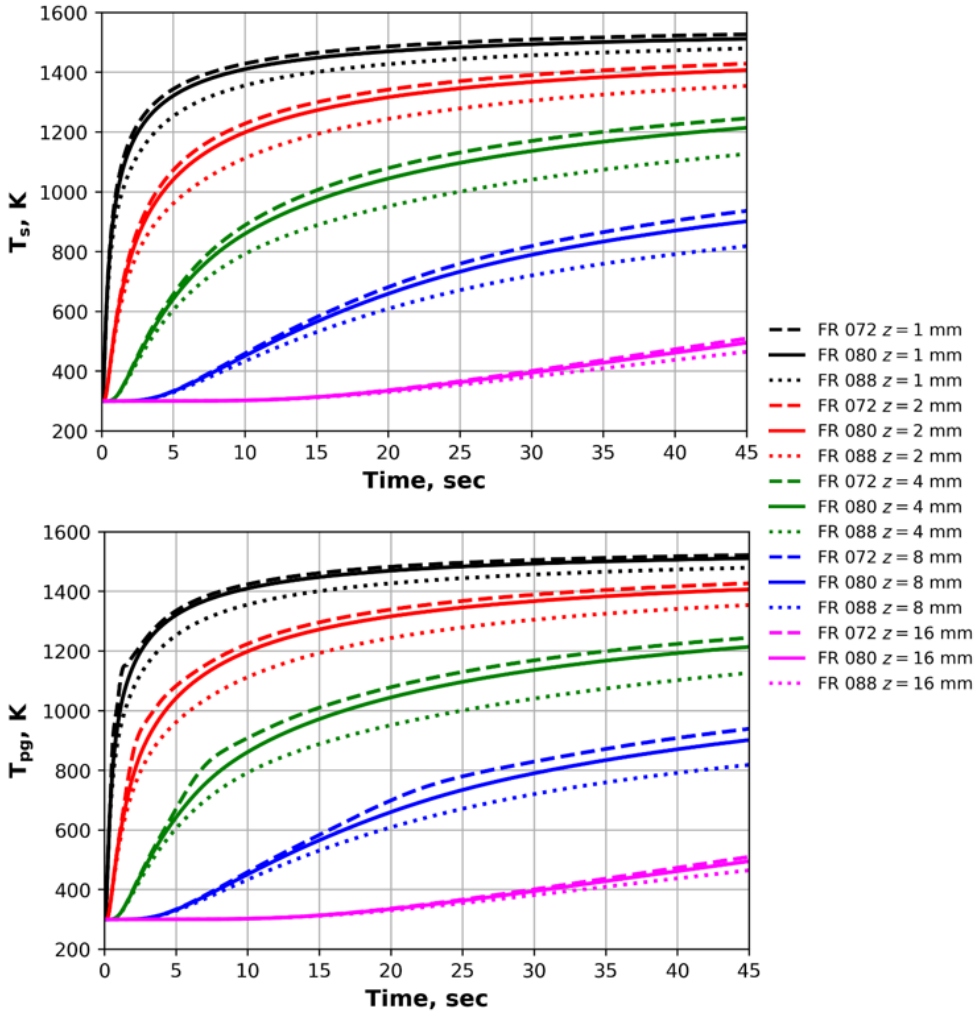


Figure 5.16: Effects of porosity on solid and reacting pyrolysis gas mixture temperatures

may stem from the differences between the properties of the gas mixtures.

Figure 5.19 gives the variations in the depths of the pyrolysis and char fronts along with pyrolysis gas mixture blowing rates obtained through finite-rate solutions. The results match those obtained under frozen flow assumption as the porosity level and depths for pyrolysis and char fronts are negatively correlated and as the porosity level decreases, more pyrolysis gases are injected to the boundary layer owing to the increased temperatures and density.

In order to obverse the influence of chemical reactions along with the change in porosity level on the material response more clearly, temperature differences between the

Table 5.7: Maximum temperature differences from the baseline solution in finite-rate chemistry model

Temperature Difference	z_{1mm}	z_{2mm}	z_{4mm}	z_{8mm}	z_{16mm}
$max\left(\frac{T_{s,072}-T_{s,080}}{T_{s,080}}\right)$, %	2.7	3.0	3.5	3.9	2.8
$max\left(\frac{T_{pg,072}-T_{pg,080}}{T_{pg,080}}\right)$, %	10.7	10.2	8.3	6.6	2.9
$max\left(\frac{T_{s,088}-T_{s,080}}{T_{s,080}}\right)$, %	−6.5	−7.8	−8.9	−9.2	−6.1
$max\left(\frac{T_{pg,088}-T_{pg,080}}{T_{pg,080}}\right)$, %	−6.6	−7.8	−8.9	−9.2	−6.1

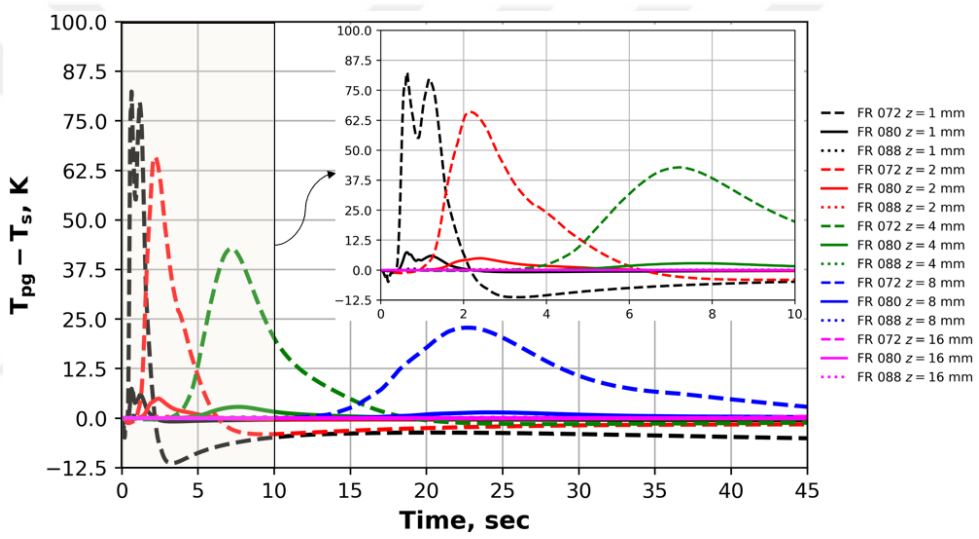


Figure 5.17: Effects of porosity on temperature differences between the solid and reacting pyrolysis gas mixture

solids as well as pyrolysis gas mixtures of frozen flow and finite-rate solution are plotted and given in Figure 5.20 and Figure 5.21, respectively. Temperatures of the solid material predicted by frozen flow assumption are always higher than those obtained through finite rate solutions at depths close to the surface, i.e. $z = 1\,mm$ and $z = 2\,mm$. At lower depths, negative temperature differences are observed. As stated previously, this indicates temporary dominance of exothermic reactions. Results for the pyrolysis gas mixtures are similar to those for solid material. However, difference from the baseline results are much more significant when the initial virgin porosity is

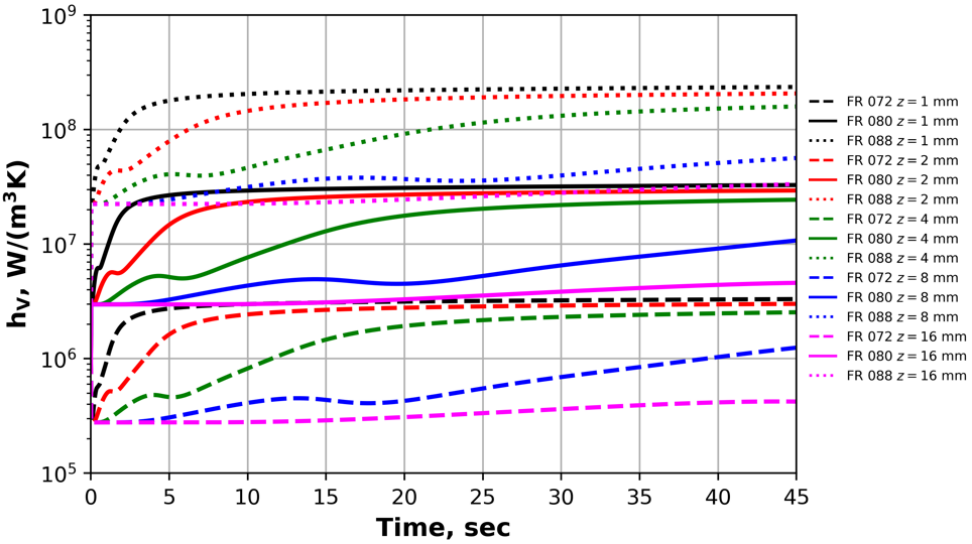


Figure 5.18: Volumetric heat transfer coefficient between the pyrolysis gas mixture and solid at different depths for varying porosity values in finite-rate solutions

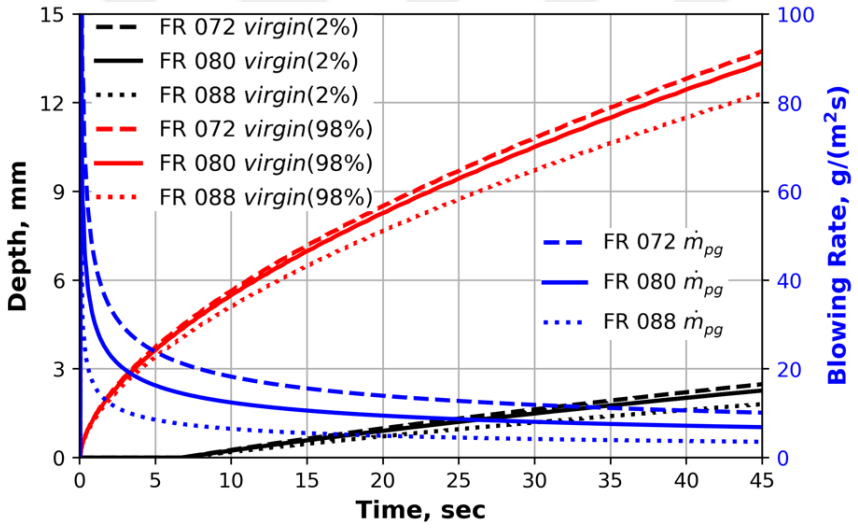


Figure 5.19: Effects of porosity on blowing rates and pyrolysis and char fronts in finite-rate chemistry model

0.72. This result seems to be related to the fact that at lower porosity levels the volumetric heat transfer between the phases is lower. Therefore, pyrolysis gas mixture temperature can deviate from the solid temperature more easily.

Figure 5.22 compares the mole concentrations of major species, i.e. CH_4, C_2H_2, CO, CO_2, H_2 and C injected to the boundary layer predicted by finite-rate solutions for

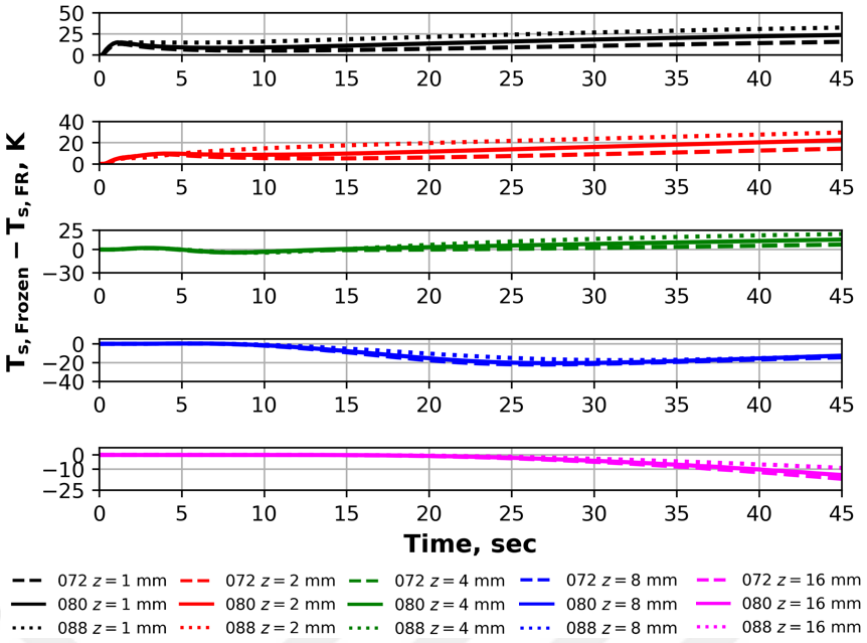


Figure 5.20: Temperature differences between the solids at different depths

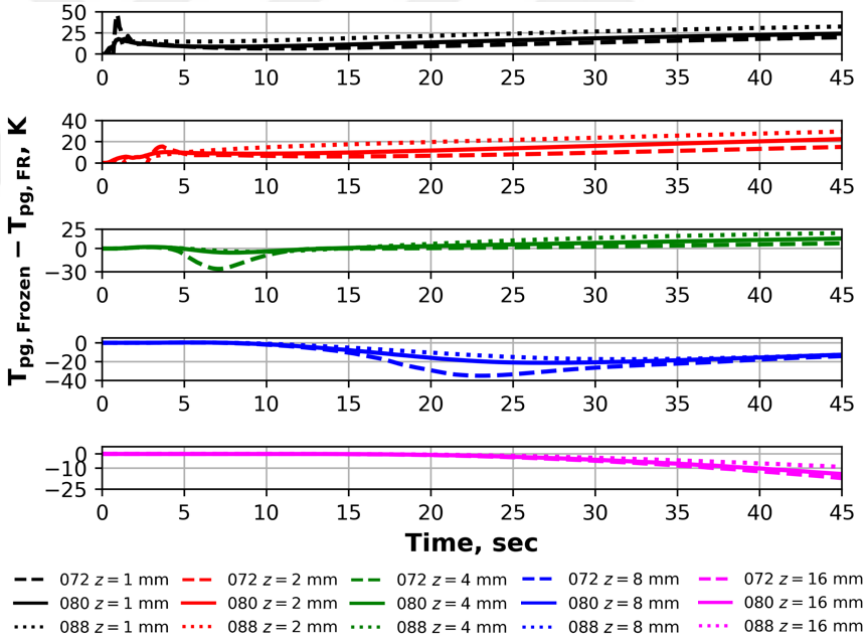


Figure 5.21: Temperature differences between the pyrolysis gas mixtures at different depths

different porosity values. Mole fractions for other species are not shown due to their very low concentrations. Time variations of the species concentrations for different porosity levels are almost identical. However, increasing the porosity level causes

higher H_2 and CO injections, and lower CH_4 and CO_2 injections to the boundary layer most probably due to the change in temperature field inside the ablative material.

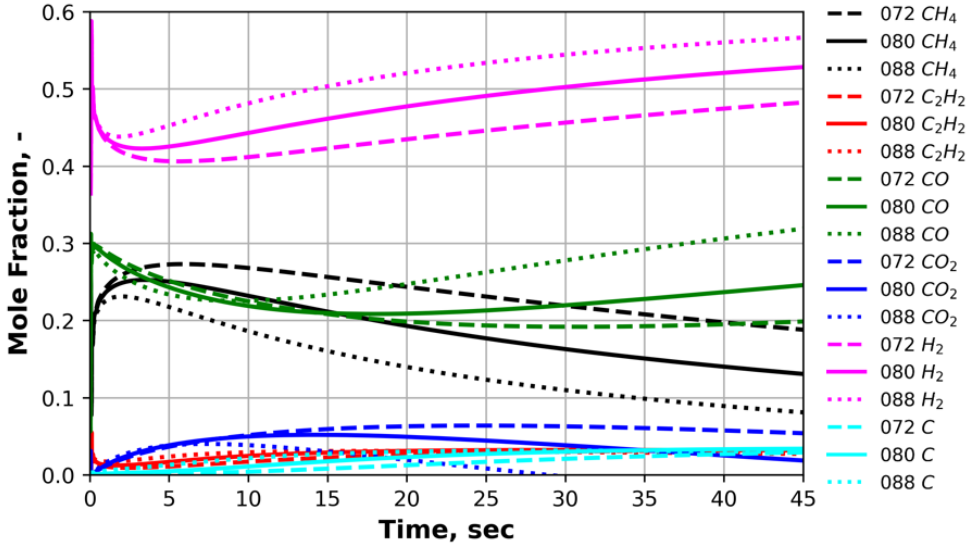


Figure 5.22: Effects of porosity on major species injected to the boundary layer

5.3.2 Permeability

In order to investigate the influence of the variation of permeability on the thermal response of the lightweight charring ablative materials, simulations with various values of permeability are performed while keeping the porosity of the virgin and char material at the baseline values of 0.80 and 0.85, respectively. The results presented are for permeabilities equal to the baseline values of 1.6×10^{-11} and 2.0×10^{-11} m^2 denoted as $1 - B$, five times the baseline values denoted as $5 - B$, and one-fifth the baseline values denoted as $02 - B$.

Plots for the variation of the solid and pyrolysis gas mixture temperatures as permeability changes are not given since results are close to each other, and it is rather hard to differentiate the curves from each other. However, maximum temperature differences from the baseline values are given in Table 5.8 and Table 5.9 for the frozen flow and finite-rate solutions, respectively. As seen, the maximum solid temperature differences between the solutions are less than 0.5% for the most part and then can

be regarded as negligible for engineering analyses. For the pyrolysis gas mixture, lower permeability values make no significant changes; however, higher permeability values result in noticeable differences in particular at depths close to the surface. It is also apparent that chemical reactions amplify the maximum temperature deviations from the baseline solution for the pyrolysis gas mixture. Another remarkable point is that at higher permeability values while the solid temperature deviations from the baseline solutions are negligible, the pyrolysis gas temperature deviations from the baseline solutions are visible. This result indicates abated thermal interaction between the solid and pyrolysis gases, i.e. lower volumetric heat transfer coefficient between the phases.

Table 5.8: Maximum temperature differences from the baseline solution for frozen flow

Temperature Difference	z_{1mm}	z_{2mm}	z_{4mm}	z_{8mm}	z_{16mm}
$max\left(\frac{T_{s,02-B}-T_{s,1-B}}{T_{s,1-B}}\right)$, %	<0.5	<0.5	<0.5	<0.5	<0.5
$max\left(\frac{T_{pg,02-B}-T_{pg,1-B}}{T_{pg,1-B}}\right)$, %	<0.5	<0.5	<0.5	<0.5	<0.5
$max\left(\frac{T_{s,5-B}-T_{s,1-B}}{T_{s,1-B}}\right)$, %	<0.5	<0.5	<0.5	<0.5	<0.5
$max\left(\frac{T_{pg,5-B}-T_{pg,1-B}}{T_{pg,1-B}}\right)$, %	2.8	1.5	0.7	<0.5	<0.5

Table 5.9: Maximum temperature differences from the baseline solution in finite-rate chemistry model

Temperature Difference	z_{1mm}	z_{2mm}	z_{4mm}	z_{8mm}	z_{16mm}
$max\left(\frac{T_{s,02-B}-T_{s,1-B}}{T_{s,1-B}}\right)$, %	<0.5	<0.5	<0.5	<0.5	<0.5
$max\left(\frac{T_{pg,02-B}-T_{pg,1-B}}{T_{pg,1-B}}\right)$, %	−0.6	<0.5	<0.5	<0.5	<0.5
$max\left(\frac{T_{s,5-B}-T_{s,1-B}}{T_{s,1-B}}\right)$, %	−2.1	−0.7	<0.5	<0.5	<0.5
$max\left(\frac{T_{pg,5-B}-T_{pg,1-B}}{T_{pg,1-B}}\right)$, %	3.5	2.5	1.6	0.8	<0.5

Figure 5.23 and Figure 5.24 show the temperature differences between the pyrolysis gas mixture and solid phase, i.e. $\Delta T = T_{pg} - T_s$, at different depths for the frozen flow and finite-rate solution, respectively. Similar to the results presented in the previous subsection, as heat wave penetrates into the ablative material, temperature differences between the pyrolysis gas mixture and solid phase increase and then, temperatures get closer. The smaller the permeability is, the shorter time is required to reach the local thermal equilibrium condition. As the permeability gets larger, temperature difference between the phases becomes more notable. The baseline and smaller values lead to local thermal equilibrium from the very beginning of the simulation. Thus, it can be deduced that local thermal equilibrium solution is sufficient for both frozen and finite-rate solutions when virgin permeability is smaller than $1.6 \times 10^{-11}\ m^2$ for the material under consideration. It is also worth to restate that, as seen, chemical reactions increase the temperature differences between the solid and pyrolysis gas mixture.

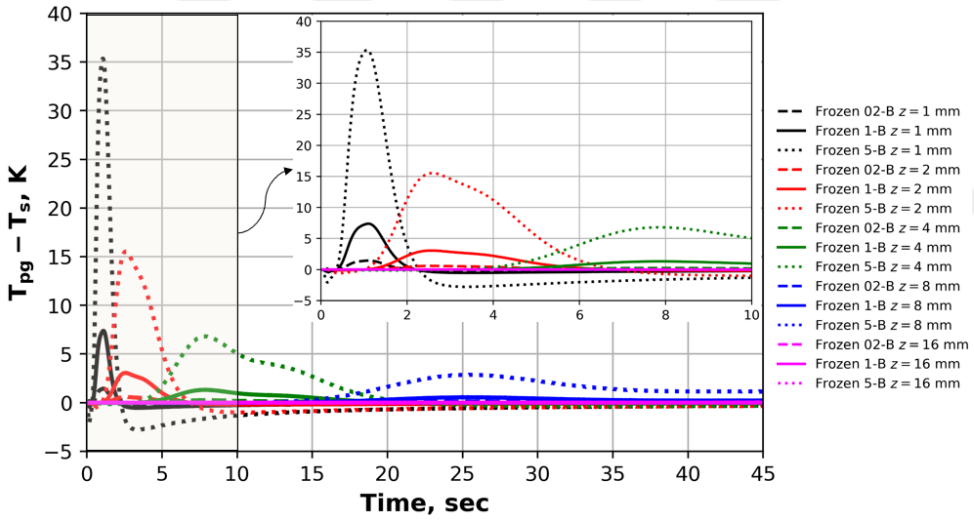


Figure 5.23: Temperature differences between the frozen pyrolysis gas mixture and solid phase at different depths for varying permeability values

The estimated volumetric heat transfer coefficients at different locations are plotted in Figure 5.25 and Figure 5.26 for the frozen flow and finite-rate solutions, respectively. It is apparent that the volumetric heat transfer coefficient is also very sensitive to the permeability level and reducing permeability leads to order of magnitude increase in volumetric heat transfer coefficient. Therefore, solutions with lower permeabil-

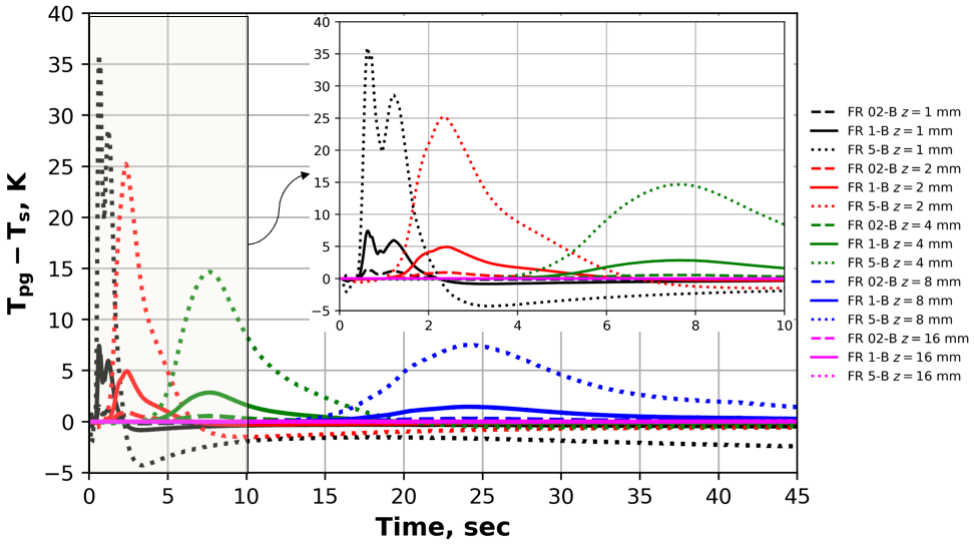


Figure 5.24: Temperature differences between the reacting pyrolysis gas mixture and solid phase at different depths for varying permeability values

ity values converge to local thermal equilibrium solutions rapidly. As observed in the previous subsection, compared to the frozen flow solutions, the volumetric heat transfer coefficients obtained through finite-rate solutions are relatively lower, hence, it gives rise to higher temperature differences between the phases.

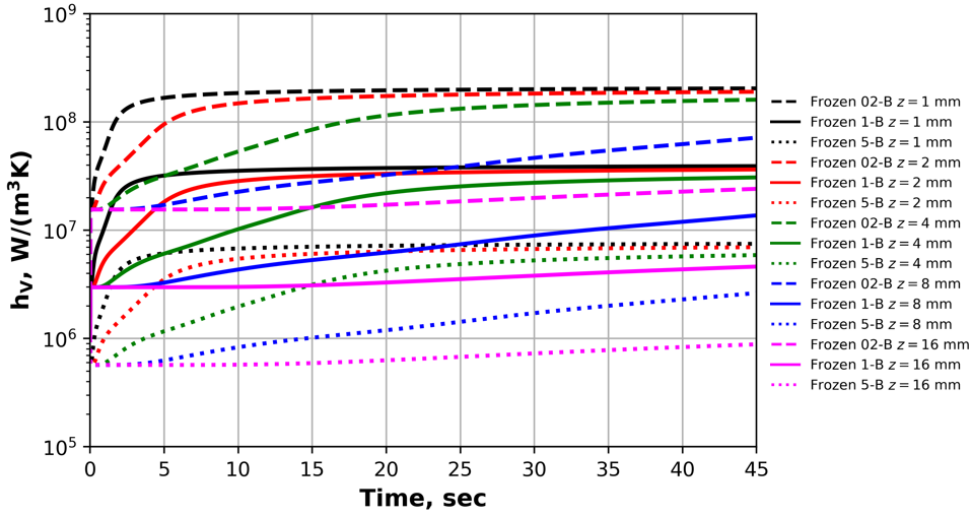


Figure 5.25: Volumetric heat transfer coefficient between the frozen pyrolysis gas mixture and solid at different depths for varying permeability values

As done in the previous subsection, so as to examine the influence of chemical re-

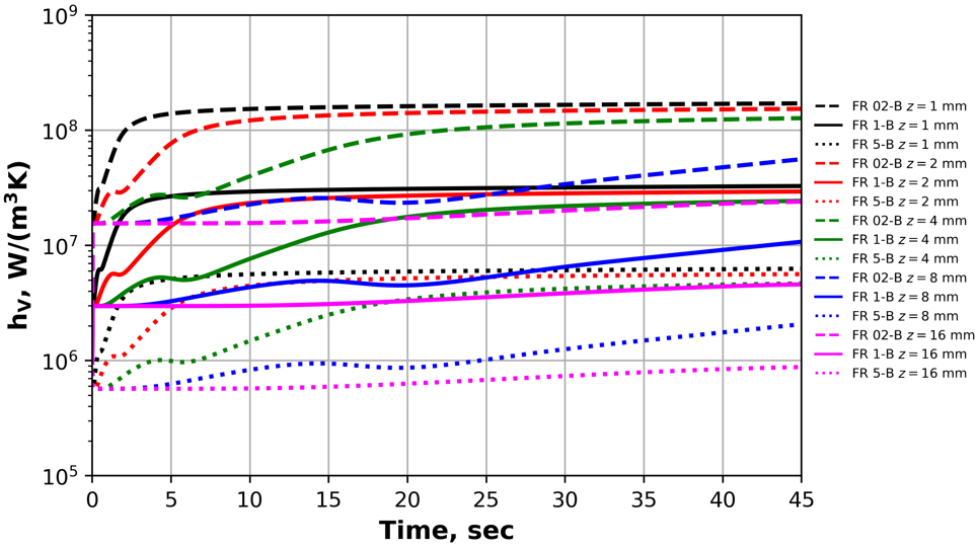


Figure 5.26: Volumetric heat transfer coefficient between the reacting pyrolysis gas mixture and solid at different depths for varying permeability values

actions along with the change in permeability level on the material response more clearly, temperature differences between the solids as well as pyrolysis gas mixtures of frozen flow and finite-rate solution are plotted and given in Figure 5.27 and Figure 5.28, respectively. Temperatures of the solid material predicted by frozen flow assumption are always higher than those obtained through finite rate solutions at depths close to the surface, i.e. $z = 1\ mm$ and $z = 2\ mm$. At lower depths, negative temperature differences are also observed. As stated previously, this suggests limited dominance of exothermic reactions. It is clear that differences from the baseline results are not perceptible. Results for the pyrolysis gas mixtures are similar to those for solid material. Differences from the baseline results are hardly seen when the initial virgin permeability is five times larger than the baseline value.

Figure 5.29 compares the mole concentrations of major species injected to the boundary layer predicted by finite-rate solutions. Mole fractions for other species are not shown due to their very low concentrations. Unlike to the variation of porosity, changes in permeability have almost no effect on the species concentration injected into the boundary layer. This implies that permeability variation does not alter the temperature field inside the material under consideration significantly.

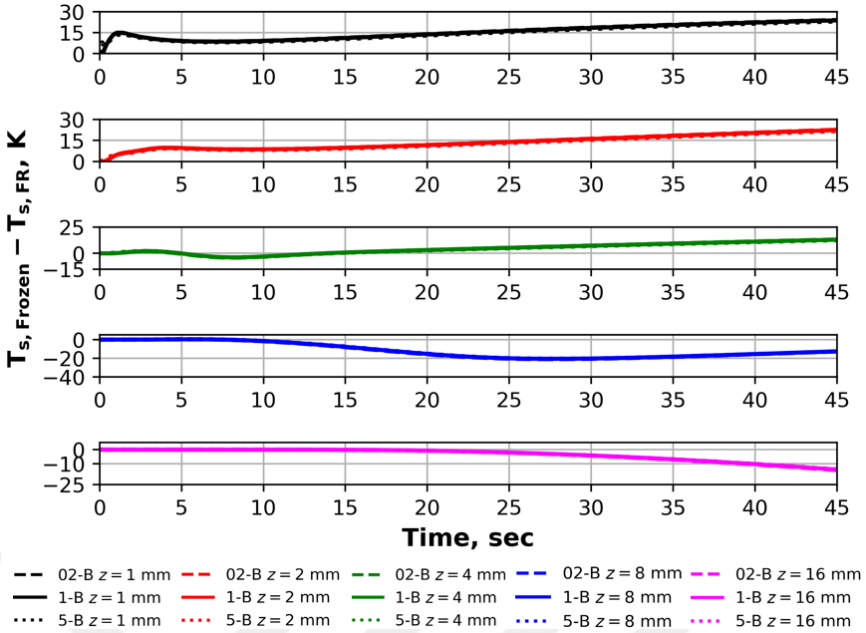


Figure 5.27: Temperature differences between the solids at different depths

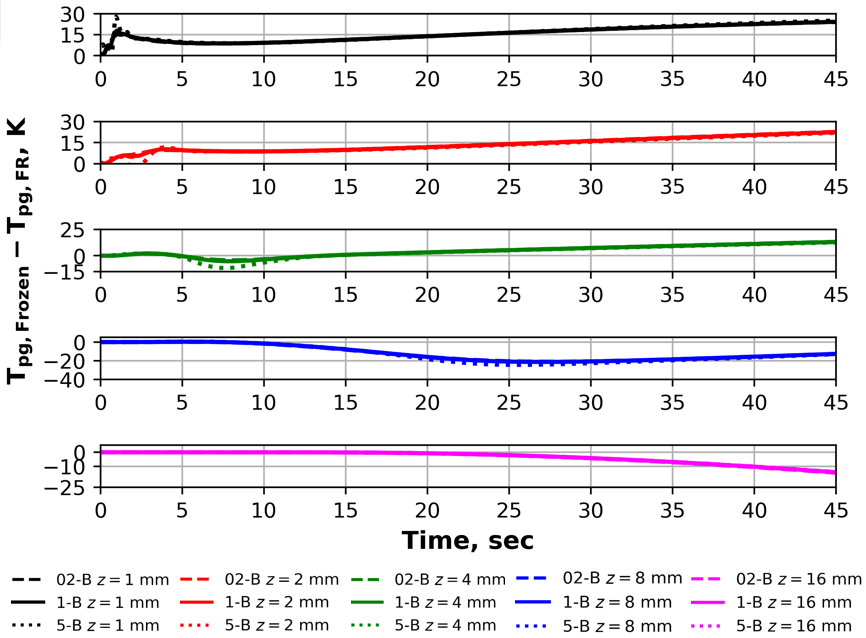


Figure 5.28: Temperature differences between the pyrolysis gas mixtures at different depths

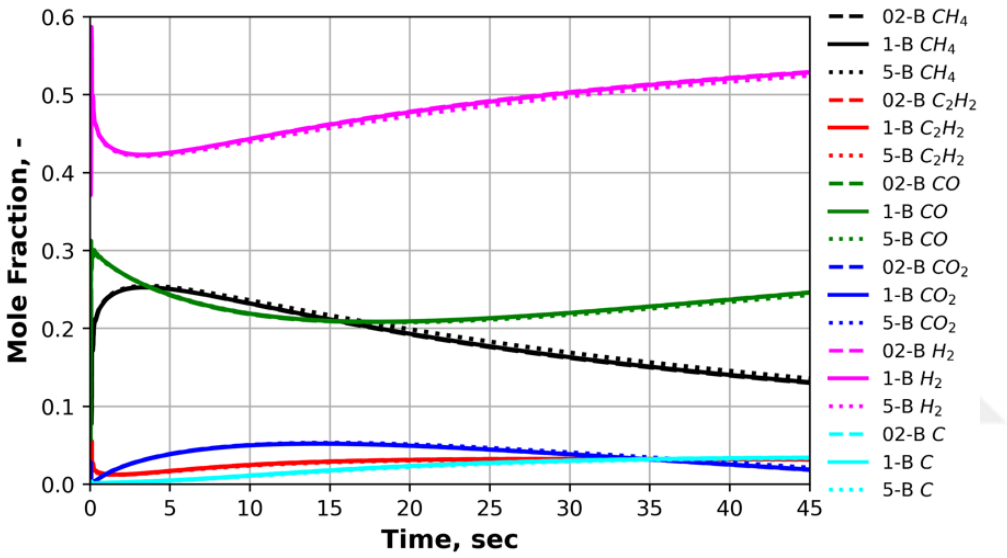


Figure 5.29: Effects of permeability on major species injected to the boundary layer

CHAPTER 6

CONCLUSIONS AND FUTURE WORK

6.1 Conclusions

A charring ablative material response framework that is able to handle thermal and chemical non-equilibrium is developed in the context of this work. The framework is flexible such that different modeling approaches as well as different reaction mechanisms can be easily implemented. It allows predicting responses of various charring ablative materials with different levels of complexity and provides a versatile framework for engineering analyses. Usage of reactor network approach provides a considerable advantage because fidelity of the code can easily and rigorously be increased by defining new flow devices and/or interactions. As an example, heterogeneous reactions can also be defined inside each reactor which then allows the modeling of the decomposition (pyrolysis) process more realistic if the reaction mechanism and the corresponding rates are known.

Effects of different chemistry models for pyrolysis gas mixtures on the response of lightweight ablative materials are examined for two test cases with and without local thermal equilibrium assumption. The results suggest that the equilibrium chemistry model yields lower in-depth temperatures mainly due to higher specific heats of the pyrolysis gas mixture. Finite-rate solutions do not always lie between the equilibrium and frozen flow solutions indicating a competition between endothermic and exothermic reactions. One interesting finding from the finite-rate solutions is that surface recession influences the molar concentrations of the species injected to the boundary layer. It is observed that thermal non-equilibrium solutions ultimately converge to the thermal equilibrium solutions. This may be attributed to the fact that the charac-

teristic length, i.e. the mean pore diameter d_m, of the material under consideration is rather small $O(10^{-5})\ m$. As a consequence, volumetric heat transfer coefficients greater than $10^6\ W/(m^3K)$ are estimated.

Influences of the porosity and permeability variations on the thermal and chemical non-equilibrium solutions are also investigated. It is seen that higher porosity and lower permeability induce local thermal equilibrium. In addition, as reported in [80], it is observed that sudden changes in boundary conditions lead to thermal non-equilibrium between the phases, however, as the time progresses, the thermal front slows down and local thermal equilibrium is eventually established.

6.2 Future Work

Although modeling of ablative materials dates back to 1960s and extensive studies have been carried out, there still exists room for further research stemming from complexity and vastness of the subject. The following potential research areas and augmentations to the research code are highlighted:

- New reaction mechanism for pyrolysis gases
- Increasing dimensionality
- Modeling species diffusion
- Detailed modeling of pyrolysis gas transport
- In-depth ablation (volume ablation) and surface chemistry

6.2.1 New Reaction Mechanism for Pyrolysis Gases

The reaction mechanism used to obtain the finite-rate solutions dates from 1970s and consists of multistep, irreversible reactions based on very specific reaction paths which provoke nonphysical mole fractions in calculations. In addition, it is claimed in [119] that this reaction mechanism does not agree well with decomposition of phenolic gas. Another reaction mechanism was developed by Scoggins [23] but it has

no basis in experimental work, therefore, it needs further verification and validation studies. As a result, a new reliable reaction mechanism is highly demanded and its development would be a major contribution to the modeling of charring ablative materials.

6.2.2 Increasing Dimensionality

The research code currently solves only 1D problems. Extension of the research code to 2D and 3D domains would allow performing optimization studies to determine the shape and thickness of the ablative thermal protection material. Furthermore, effects of orthotropic material properties and uneven surface recession can be investigated. In addition to the thermal response of the material, thermal stresses can also be taken into account in the extended domains. However, it is thought that the implementation of the reactor network approach could be impractical due to huge computational expenses. One remedy to this problem may be parallelization of the code.

6.2.3 Implementation of Species Diffusion

In finite-rate solutions diffusion of species is not considered. Mass transfer due to diffusion in porous media may not be negligible compared to advection at low pressures [38]. In addition, not only the overall blowing rate, but also the proper determination of the blowing rate of individual species enables a more accurate analysis of boundary layer flow-material interaction [120]. Therefore, differences between the solutions with and without species diffusion along with thermal (non-)equilibrium and determination of conditions which make it considerable may contribute to the existing literature. Furthermore, Fick's law may not be suitable for estimation of diffusion fluxes in multi-component gas mixtures, excluding binary mixtures [11]. A promising alternative is the dusty gas model. No ablative material response code uses the dusty gas model owing to its more complicated nature. Implementation of this model would bring a novel contribution to the ablation literature.

Modeling species diffusion will add additional term to the gas phase energy equation and species conservation equation. Required modifications in the gas phase energy

equation seem to be accomplish-able. However, feasibility of the modifications to solve the species continuity equations along with reactor network approach shall be figured out.

6.2.4 Pyrolysis Gas Transport

Pyrolysis gas flow inside the porous ablative material is modeled using the Darcy's law like majority of the other existing codes. Indeed, Darcy's law is derived for 1D incompressible flow under steady state conditions, and it only accounts for viscous resistance of the flow at low speeds. Thus, appropriateness of its usage is arguable. There exist some alternatives. One is the Darcy-Forchheimer equation that takes into account the flow inertia at high speed flows. Another option is the implementation of the unsteady porous flow momentum equations. These models can be implemented in the research code. In addition, modeling the pyrolysis gas flow at very low pressures, i.e. when continuum regime is not valid, may be studied.

6.2.5 Surface Chemistry and Volume Ablation

In this work, ablation is assumed to occur at the boundary surface, and it is treated as a boundary condition using $B^{'}$ Tables based on a very simplified boundary layer approach under chemical equilibrium assumption. Indeed, pyrolysis gas mixture injected to the surface could react with boundary layer gases in a finite-rate fashion along with the oxidation of surface. In addition, As stated in Chapter 2, several studies suggest that species from the boundary layer can diffuse to the porous material and react in depth with solid resulting in mass loss in particular at low pressures. This hypothesis then considers the ablation not only as a surface phenomenon but a surface/volume phenomenon.

Implementation of a surface thermo-chemical model would allow for finite-rate heterogeneous reactions instead of assuming thermo-chemical equilibrium at the surface. The surface recession rate is strongly dependent on how much oxygen and nitrogen atoms reach the surface. The amount of these species is dependent on the flow environment and the composition of the injected pyrolysis gases and possible reactions

among them. More accurate estimation also requires coupling the material response code with a reactive flow solver. Without coupling with a flow solver, implementation of another model such as counter-flow reaction model can be studied to model reactions in boundary layer and at the surface. Effects of in-depth reactions and species diffusion on the surface thermo-chemistry and its subsequent effects on the ablation rate may be a novel contribution to the ablation literature.

Volume ablation requires the modeling of oxygen diffusion from the boundary layer gases inside the material and heterogeneous reactions of the diffused gas with the solid. In [38] oxidation of the char layer is modeled first at microscopic level and then macroscopic model obtained the through volume averaging. The derived macroscopic model can be implemented in the developed numerical framework. However, more accurate modeling at microscopic level and then obtaining a new macroscopic model would be much more appealing and a novel contribution to the ablation literature.

REFERENCES

[1] NASA, "Heat Shield Milestone Complete for First Orion Mission with Crew." Accessed Jul. 8, 2020 [Online]. https://www.nasa.gov/image-feature/heat-shield-milestone-complete-for-first-orion-mission-with-crew.

[2] G. P. Sutton and O. Biblarz, *Rocket Propulsion Elements*. Wiley, 9 ed., 2016.

[3] W. M. Rohsenow, J. P. Hartnett, and Y. I. Cho, eds., *Handbook of Heat Transfer*, ch. 6. McGraw-Hill, 3 ed., 1998.

[4] D. Bianchi, *Modeling of Ablation Phenomena in Space Applications*. PhD thesis, University of Rome, 2007.

[5] "Entry thermal protection," Tech. Rep. NASA-SP-8014, NASA, 1968.

[6] M. E. Tauber, "A review of high-speed, convective, heat transfer computation methods," Tech. Rep. NASA-TP-2914, NASA, 1989.

[7] G. Duffa, *Ablative Thermal Protection Systems Modeling*. AIAA, 2013.

[8] A. Mazzaracchio and M. Marchetti, "A probabilistic sizing tool and monte carlo analysis for entry vehicle ablative thermal protection systems," *Acta Astronautica*, vol. 66, pp. 821–835, 2010.

[9] M. Natali, J. M. Kenny, and L. Torre, "Science and technology of polymeric ablative materials for thermal protection systems and propulsion devices: A review," *Progress in Material Science*, vol. 84, pp. 192–275, 2016.

[10] J. H. Kuo, D. W. Ho, and O. A. Ezeyoke, "A review of numerical and experimental characterization of thermal protection material, part i: Numerical modelling," 42, AIAA/ASME/SAE/ASEE Joint Propulsion Conference and Exhibition, 2006.

[11] J. Lachaud, T. E. Magin, I. Cozmuta, and N. N. Mansour, "A short review of

ablative material response models and simulation tools," 7, European Symposium on the Aerothermodynamics, 2006.

[12] V. Kumar and B. Kandasubramanian, "Advances in ablative composite of carbon based materials: A review," *Industrial and Engineering Chemistry Research*, 2019.

[13] C. B. Moyer and R. A. Rindal, "An analysis of the coupled chemically reacting boundary layer and charring ablator, part ii: Finite difference solution for the in-depth response of charring materials considering surface chemical and energy balances," Tech. Rep. NASA-CR-1061, NASA, 1968.

[14] G. C. April, *Energy Transfer in the Char Zone of a Charring Ablator*. PhD thesis, Louisiana State University, 1969.

[15] R. K. Clark, "Simulation of pyrolysis gas flow through a char layer during ablation," Tech. Rep. NASA-TN -D-5464, NASA, 1969.

[16] R. K. Clark, *A Numerical Analysis of the Transient Response of an Ablation System Including the Effects of Thermal Non-equilibrium, Mass Transfer and Chemical Kinetics*. PhD thesis, Virginia Polytechnic Institute and State University, 1972.

[17] B. F. Blackwell and R. E. Hogan, "One-dimensional ablation using landau transformantion and finite control volume procedure," *Journal of Thermophysics and Heat Transfer*, vol. 8, no. 2, pp. 282–287, 1994.

[18] H. G. Landau, "Heat conduction in a melting solid," *Quarterly of Applied Math*, vol. 8, no. 1, pp. 81–94, 1950.

[19] A. J. Amar, "Modeling of one-dimensional ablation with porous using finite control volume procedure," Master's thesis, North Carolina State University, 2006.

[20] A. J. Amar, B. F. Blackwell, and J. R. Edwards, "Development and verification of a one-dimensional ablation code including pyrolysis gas flow," *Journal of Thermophysics and Heat Transfer*, vol. 23, no. 1, pp. 59–71, 2009.

[21] O. Joshi, *Fluid-Structure Thermal Coupling and Ablation Effects in Atmospheric Entry*. PhD thesis, Ecole Polytechnique Federale De Lausanne, 2013.

[22] A. Ayasoufi, R. K. Rahmani, G. Cheng, R. Koomumlil, and K. Neroorkar, "Numerical simulation of ablation for reentry vehicles," 9, AIAA/ASME Joint Thermophysics and Heat Transfer Conference, 2006.

[23] J. B. Scoggins, "The development of a thermochemical non-equilibrium and pyrolysis model for carbon phenolic thermal protection systems," Master's thesis, North Carolina State University, 2011.

[24] "NIST Chemical Kinetics Database." Version 7.0, Release 1.4.3, Data Version 2008.12. http://kinetics.nist.gov.

[25] Y. K. Chen and F. S. Milos, "Effects of non-equilibrium chemistry and darcy-forchheimer pyrolysis flow for charring ablator," *Journal of Spacecraft and Rockets*, vol. 50, no. 2, pp. 256–269, 2013.

[26] J. Lachaud, J. B. Scoggins, T. E. Magin, M. G. Meyer, and N. N. Mansour, "A generic local thermal equilibrium model for porous reactive materials submitted to high temperatures," *International Journal of Heat and Mass Transfer*, vol. 108, pp. 1406–1417, 2017.

[27] W. Li, J. Huang, Zhongwei, L. Wang, H. Huang, and J. Liang, "A model for thermal protection ablative material with local thermal non-equilibrium and thermal radiation mechanisms," *Acta Astronautica*, vol. 183, pp. 101–111, 2021.

[28] F. S. Milos and Y. K. Chen, "Ablation, thermal response, and chemistry program for analysis of thermal protection systems," *Journal of Spacecraft and Rockets*, vol. 50, no. 1, pp. 137–149, 2013.

[29] Y. K. Chen and F. S. Milos, "Two-dimensional implicit thermal response and ablation program for charring materials," *Journal of Spacecraft and Rockets*, vol. 38, no. 4, pp. 137–149, 2001.

[30] A. J. Amar, A. B. Oliver, B. S. Kirk, G. Salazar, and J. Droba, "Overview of the charring ablator response (char) code," 46, AIAA Thermophysics Conference, 2016.

[31] J. Lachaud and N. N. Mansour, "Porous-material analysis toolbox based on openfoam and applications," *Journal of Thermophysics and Heat Transfer*, vol. 28, no. 2, pp. 191–202, 2014.

[32] F. S. Aykan, "Numerical analysis of ablation process on a two dimensional external surface," Master's thesis, Middle East Technical University, 2005.

[33] F. S. Aykan and Z. Dursunkaya, "Iki boyutlu dis yuzeylerde isil asinma sayisal analizi," *Isi Bilimi ve Teknigi Dergisi*, vol. 28, no. 1, pp. 43–46, 2008.

[34] B. Simsek, *Aerodinamik Isinmanin ve Isil Koruma Sistemlerinin Aerodinamik Isinmaya Bagli Termo-Kimyasal Asinmasinin Incelenmesi*. PhD thesis, TOBB Ekonomi ve Teknoloji Universitesi, 2019.

[35] B. Simsek and S. Uslu, "One-dimensional aerodynamic heating and ablation prediction," *Journal of Aerospace Engineering*, vol. 32, no. 4, 2019.

[36] C. O. Alanyalioglu, "Numerical simulation of charring ablation coupled with computational fluid dynamics," Master's thesis, Middle East Technical University, 2019.

[37] R. P. Hagerty, A. L. Jaumotte, O. Lutz, and S. S. Penner, eds., *Combustion and Propulsion*, 5, Agard Colloquium, Pergamon Press, 1963.

[38] J. Lachaud, I. Cozmuta, and N. N. Mansour, "Multiscale approach to ablation modeling of phenolic impregnated carbon ablators," *Journal of Spacecraft and Rockets*, vol. 47, no. 6, pp. 910–921, 2010.

[39] P. Schrooyen, K. Hillewaert, T. E. Magin, and P. Chatelain, "Fully implicit discontinuous galerkin solver to study surface and volume ablation competition in atmospheric entry flows," *International Journal of Heat and Mass Transfer*, vol. 103, pp. 108–124, 2016.

[40] J. A. Dec, *Three Dimensional Finite Element Ablative Thermal Response Analysis Applied to Heat Shield Penetration Design*. PhD thesis, Georgia Institute of Technology, 2010.

[41] H. E. Goldstein, "Pyrolysis kinetics of nylon 6-6, phenolic resin, and their

composites," *Journal of Macromolecular Science: Part A - Chemistry*, vol. 3, no. 4, pp. 649–673, 1969.

[42] H.-K. Ahn, C. Park, and K. Sawada, "Response of heat shield material at stagnation point of pioneer-venus probes," *Journal of Thermophysics and Heat Transfer*, vol. 16, no. 3, pp. 432–439, 2002.

[43] J. B. Henderson, M. R. Tant, and G. R. Moore, "Determination of kinetic parameters for the thermal decomposition of phenolic ablative materials by a multiple heating rate method," *Thermochimica Acta*, vol. 44, pp. 253–264, 1981.

[44] M. E. Ewing, T. S. Laker, and D. T. Walker, "Numerical modeling of ablation heat transfer," *Journal of Thermophysics and Heat Transfer*, vol. 27, no. 4, pp. 615–632, 2013.

[45] H. P. G. Darcy, *Les Fontaines Publiques de la Ville de Dijon*. Dalmont, 1856.

[46] M. Kaviany, *Principles of Heat Transfer in Porous Media*. Springer, 2 ed., 1995.

[47] D. A. Nield and A. Bejan, *Convection in Porous Media*. Springer, 3 ed., 2006.

[48] A. Sullins and K. Daryabeigi, "Effective thermal conductivity of high porosity open cell nickel foam," No. 35, AIAA Thermophysics Conference, 2001.

[49] C. Tseng, M. Yamaguchi, and T. Ohmori, "Thermal conductivity of polyurethane foams from room temperature to 20 k," *Cryogenics*, vol. 37, pp. 305–312, 1997.

[50] A. Bhattacharya, V. Calmidi, and R. Mahajan, "An analytical-experimental study for the determination of the effective thermal conductivity of high porosity fibrous foams," in *Application of Porous media Methods for Engineered Materials* (R. M. Sullivan, ed.), vol. 233, pp. 13–20, ASME, 1999.

[51] K. Boomsma and D. Poulikakos, "On the effective thermal conductivity of three-dimensionally structured fluid-saturated metal foam," *International Journal of Heat and Mass Transfer*, vol. 44, no. 3, pp. 827–836, 2000.

[52] F. A. Williams, *Combustion Theory*. The Benjamin Cummings Publishing, 2 ed., 1985.

[53] R. M. Kendall, R. A. Rindal, and E. P. Bartlett, "A multi-component boundary layer chemically coupled to an ablating surface," *AIAA Journal*, vol. 5, no. 6, pp. 1063–1071, 1967.

[54] W. M. Kays and M. E. Crawford, *Convective Heat and Mass transfer*. McGraw-Hill, 3 ed., 1993.

[55] F. Moukalled, L. Mangani, and M. Darwish, *Finite Volume Method in Computational Fluid Dynamics*. Springer, 2016.

[56] P. Wesseling, *Principles of Computational Fluid Dynamics*. Springer, 2001.

[57] J. Blazek, *Computational Fluid Dynamics: Principles and Applications*. Elsevier, 3 ed., 2015.

[58] J. Crank, *Free and Moving Boundary Problems*. Clarendon Press, 1984.

[59] A. J. van Eekelen, J. M. Bouilly, S. Hudrisier, J. M. Dupillier, and Y. Aspa, "Design and numerical modeling of charring material ablators for re-entry applications," No. 11, SAMTECH Users Conference, 2009.

[60] P. G. Cross and I. D. Boyd, "Conjugate analyses of ablation in rocket nozzles," *Journal of Spacecraft and Rockets*, vol. 56, no. 5, pp. 1593–1610, 2019.

[61] A. Martin and I. D. Boyd, "Non-darcian behavior of pyrolysis gas in a thermal protection system," *Journal of Thermophysics and Heat Transfer*, vol. 24, no. 1, pp. 60–68, 2010.

[62] P. G. Cross and I. D. Boyd, "Two-dimesional modeling of ablation and pyrolysis with application to rocket nozzles," No. 46, AIAA Thermophysics Conference, 2016.

[63] S. C. Chapra and R. P. Canale, *Numerical Methods for Engineers*. McGraw-Hill, 7 ed., 2015.

[64] T. Suzuki, K. Sawada, T. Yamada, and Y. Inatani, "Gas permeability of oblique-layered carbon-cloth ablator," *Journal of Thermophysics and Heat Transfer*, vol. 18, no. 4, pp. 548–550, 2004.

[65] C. J. Roy, "Review of code and solution verification procedures for computational simulation," *Journal of Computational Physics*, vol. 205, pp. 131–156, 2005.

[66] P. Knupp and K. Salari, *Verification of Computer Codes in Computational Science and Engineering*. Chapman & Hall-CRC, 2003.

[67] "Standard for verification and validation in computational fluid dynamics and heat transfer." ASME V&V 20-2009, 2009.

[68] W. D. Callister, *Material Science and Engineering: An Introduction*. John Wiley & Sons, 7 ed., 2007.

[69] V. S. Arpacı, *Conduction Heat Transfer*. Addison-Wesley, 1966.

[70] S. Whitaker, *Fundamental Principles of Heat Transfer*. Pregamon Press, 1977.

[71] P. Vadasz, "Analytical solution to nonlinear thermal diffusion: Kirchhoff versus cole-hopf transformations," *Journal of Heat Transfer*, vol. 132, no. 12:121302, 2010.

[72] J. I. Masters, "Problem of intense surface heating of a slab accompanied by change of phase," *Journal of Applied Physics*, vol. 27, no. 5, pp. 477–484, 1956.

[73] H. S. Carslaw and J. C. Jaeger, *Conduction of Heat in Solids*. Oxford University Press, 2 ed., 1959.

[74] B. L. Clark, "A parametric study of the transient ablation of teflon," *Journal of Heat Transfer*, pp. 347–354, 1972.

[75] W. J. Minkowycz, E. M. Sparrow, and J. Y. Murthy, eds., *Handbook of Numerical Heat Transfer*, ch. 13. John Wiley & Sons, 2 ed., 2006.

[76] J. Lachaud, A. Martin, T. V. Eekelen, I. Cozmuta, and B. Laub, "Ablation workshop test case." 4th Ablation Workshop, 2011.

[77] "Theoretical anlative composite for open testing (tacot)." 5th Ablation Workshop, 2012. Version 2.2.

[78] J. Lachaud, A. Martin, T. V. Eekelen, and I. Cozmuta, "Ablation test-case series #2." 5th Ablation Workshop, 2012.

[79] D.-Y. Lee and K. Vafai, "Analytical characterization and conceptual assessment of solid and fluid temperature differentials in porous media," *Journal of Heat and Mass Transfer*, vol. 42, pp. 423–435, 1999.

[80] D. B. Ingham and I. Pop, eds., *Transport Phenomena in Porous Media III*, ch. 6. Elsevier, 1 ed., 2005.

[81] W. M. Rohsenow, J. P. Hartnett, and Y. I. Cho, eds., *Handbook of Heat Transfer*, ch. 9. McGraw-Hill, 3 ed., 1998.

[82] M. Stackpoole, S. Sepka, I. Cozmuta, and D. Kontinos, "Post-flight evaluation of stardust sample return capsule forebody heatshield material," 46, AIAA Aerospace Sciences Meeting and Exhibit, 2008.

[83] N. Puiroux, M. Prat, and M. Quintard, "Non-equilibrium theories for macroscale heat transfer: Ablative composite layer systems," *International Journal of Thermal Sciences*, vol. 43, pp. 541–554, 2004.

[84] J. Florio, J. Henderson, F. Test, and R. Hariharan, "A study of effects of the assumption of local thermal equilibrium on the overall thermally-induced response of a decomposing, glass-filled polymer composite," *International Journal of Heat and Mass Transfer*, vol. 34, no. 4, pp. 135–147, 1991.

[85] A. Nakayama, F. Kuwahara, M. Sugiyama, and G. Xu, "A two-energy equation model for conduction and convection in porous media," *International Journal of Heat and Mass Transfer*, vol. 44, pp. 4375–4379, 2001.

[86] O. A. Plumb, "Convective melting of packed beds," *International Journal of Heat and Mass Transfer*, vol. 37, no. 5, pp. 829–836, 1994.

[87] A. G. Dixon and D. L. Cresswell, "Theoretical prediction of effective heat transfer parameters in packed beds," *AIChE Journal*, vol. 25, no. 4, pp. 663–676, 1979.

[88] N. Wakao and S. Kaguei, *Heat and Mass Transfer in Packed Beds*. Gordon and Breach Science Publishers, 1982.

[89] F. Kuwahara, M. Shirota, and A. Nakayama, "A numerical study of interfacial convective heat transfer in two-energy equation model for convection in porous media," *International Journal of Heat and Mass Transfer*, vol. 44, pp. 1153–1159, 2001.

[90] V. V. Calmidi and R. L. Mahajan, "Forced convection in high porosity metal foams," *Journal of Heat Transfer*, vol. 122, no. 3, pp. 557–566, 2000.

[91] C. Y. Zhao, T. Kim, T. J. Lu, and H. P. Hodson, "Thermal transport in high porosity cellular metal foams," *Journal of Thermophysics and Heat Transfer*, vol. 18, no. 3, pp. 309–307, 2004.

[92] H. Wang and L. Guo, "Volumetric convective heat transfer coefficient model for metal foams," *Heat Transfer Engineering*, pp. 1–12, 2018.

[93] L. B. Younis and R. Viskanta, "Experimental determination of the volumetric heat transfer coefficient between stream of air and ceramis foam," *International Journal of Heat and Mass Transfer*, vol. 36, no. 6, pp. 1425–1434, 1993.

[94] A. Nakayama, K. Ando, C. Yang, Y. Sano, F. Kuwahara, and J. Liu, "A study on interstitial heat transfer in consolidated and unconsolidated porous media," *Heat Mass Transfer*, vol. 45, pp. 1365–1372, 2009.

[95] X. Fu, R. Viskanta, and J. P. Gore, "Measurement and correlation of volumetric heat transfer coefficients of cellular ceramics," *Experimental Thermal and Fluid Science*, vol. 17, pp. 285–293, 1998.

[96] K. Kamiuto and S. S. Yee, "Heat transfer correlations for open-cellular porous materials," *International Communications in Heat and Mass Transfer*, vol. 32, pp. 947–953, 2005.

[97] S. Meinicke, K. Dubil, T. Wetzel, and B. Dietrich, "Heat transfer correlations for open-cellular porous materials," *International Journal of Heat amd Mass Transfer*, vol. 149, no. 119201, 2019.

[98] A. Oechsner, G. E. Murch, and M. J. S. de Lamos, eds., *Cellular and Porous Materials: Thermal Properties Simulation and Prediction*, ch. 6. Wiley-VCH, 2008.

[99] V. V. Calmidi, *Transport Phenomena in High Porosity Fibrous Metal Foams*. PhD thesis, University of Colorado-Boulder, 1998.

[100] D. Vijay, P. Goetze, R. Wulf, and U. Gross, "Homogenized and pore-scale analyses of forced convection through open cell foams," *International Journal of Heat amd Mass Transfer*, vol. 123, pp. 787–804, 2018.

[101] A. Bhattacharya, V. V. Calmidi, and R. L. Mahajan, "Thermophysical properties of high porosity metal foams," *International Journal of Heat amd Mass Transfer*, vol. 45, pp. 1017–1031, 2002.

[102] J. Warnatz, U. Mass, and R. W. Dibble, *Combustion*. Springer, 3 ed., 2006.

[103] B. E. Poling, J. M. Prausnitz, and J. P. O'Connell, *The Properties of Gases and Liquids*. McGraw-Hill, 5 ed., 2001.

[104] J. O. Hirshfelder, C. F. Curtiss, and R. B. Bird, *Molecular Theory of Gases and Liquids*. John Wiley & Sons, 1964.

[105] B. J. McBride, M. J. Zehe, and S. Gordon, "Nasa glenn coefficients for calculating thermodynamic properties of individual species," tech. rep., NASA, 2002. NASA/TP-2002-211556.

[106] C. R. Wilke, "A viscosity equation for gas mixtures," *Journal of Chemical Physics*, vol. 18, pp. 517–522, 1950.

[107] R. J. Kee, M. E. Coltrin, and P. Glaborg, *Chemically Reacting Flow: Theory and Practice*. John Wiley & Sons, 2003.

[108] S. D. Cohen and A. C. Hindmarsh, "Cvode, a stiff/nonstiff ode solver in c," *Computers in Physics*, vol. 10, no. 2, pp. 138–143, 1996.

[109] D. G. Goodwin, R. L. Spieth, H. K. Moffat, and B. W. Weber, "Cantera: An object-oriented software toolkit for chemical kinetics, thermodynamics, and transport processes." Version 2.4.0. https://www.cantera.org.

[110] J. P. O'Connell and J. M. Haile, *Thermodynamics: Fundamentals for Applications*. Cambridge University Press, 1 ed., 2005.

[111] J. M. Moran, H. N. Shapiro, D. D. Boettner, and M. B. Bailey, *Fundamentals of Engineering Thermodynamics*. John Wiley & Sons, 8 ed., 2014.

[112] O. Schroeder, "Verificationand validation studies for the kats aerothermodynamics and material response solver," Master's thesis, University of Kentucky, 2018.

[113] "Simcenter star-ccm+." Version 13.06. https://www.plm.automation.siemens.com, Siemens PLM.

[114] J. H. Langston, C. Wong, N. Diaz, F. Stefani, J. H. Koo, and M. Salita, "Validation of ablation model of pica using fully implicit ablation and thermal response program," No. 55, AIAA SciTech Forum, 2017.

[115] Y. Wang, T. K. Risch, and J. H. Koo, "Assessment of a one-dimensional finite element charring ablation material response model for phenolic-impregnated carbon ablator," *Aerospace Science and Technology*, vol. 91, pp. 301–309, 2019.

[116] F. Milos and Y. Chen, "Ablation and thermal response property model validation for phenolic impregnated carbon ablator," *Journal of Spacecraft and Rockets*, vol. 47, no. 5, pp. 786–805, 2010.

[117] G. C. April, R. W. Pike, and E. G. D. Valle, "Modeling reactive gas flow in the char layer of an ablator," *AIAA Journal*, vol. 9, no. 6, pp. 1113–1119, 1971.

[118] B. S. Venkatachari, G. C. Cheng, and R. P. Koomullil, "Uncertainty analysis of surface ablation," No. 47, AIAA Aerospace Sciences Meeting including the New Horizons Forum and Aerospace Exposition, 2009.

[119] A. Martin, "Modeling of chemical non-equilibrium effects in a charring ablator," No. 51, AIAA Aerospace Sciences Meeting including the New Horizons Forum and Aerospace Exposition, 2013.

[120] H. Weng, *Multi-dimensional Modeling of Pyrolysis Gas Transport inside Orthotropic Charring Ablators*. PhD thesis, University of Kentucky, 2014.

APPENDIX A

NEWTON'S METHOD

Newton's linearization method is employed for the iterative solution of the nonlinear equations. Linearization is enabled by expanding the nonlinear function in a Taylor series and truncating the series after the first derivative term. If a nonlinear equation is of the form:

$$f(x) = 0 \tag{A.1}$$

it can be approximated using the first two terms of the Taylor series at $x = x_0$ as:

$$f(x) \approx f(x_0) + \left.\frac{\mathrm{d}f(x)}{\mathrm{d}x}\right|_{x=x_0} (x - x_0) \tag{A.2}$$

A new estimate for the solution of x is expressed in general as:

$$x^{v+1} = x^v - \frac{f(x^v)}{\frac{\mathrm{d}f(x^v)}{\mathrm{d}x}} \tag{A.3}$$

where v is the iteration counter. The iteration continues until the change in $x^{v+1} - x^v$ is small as desired.

The Newton's method can be extended and applied to nonlinear systems of equations. Assume a system of nonlinear equations as:

$$\begin{aligned} f_1(x_1, x_2, \ldots, x_n) &= 0 \\ f_2(x_1, x_2, \ldots, x_n) &= 0 \\ &\vdots \\ f_n(x_1, x_2, \ldots, x_n) &= 0 \end{aligned} \tag{A.4}$$

Each of these equations can be expanded in Taylor's series as:

$$f(\mathbf{x} + \mathbf{\Delta x}) \approx f_i(\mathbf{x}) + \frac{\partial f_i}{\partial x_1}\Delta x_1 + \cdots + \frac{\partial f_i}{\partial x_n}\Delta x_n, \quad i = 1, 2, \ldots, n \tag{A.5}$$

At the solution, as $f(\mathbf{x} + \mathbf{\Delta x}) \rightarrow 0$, Eq. A.5 can be arranged as a set of linear equations in the matrix form as:

$$\underbrace{\begin{bmatrix} \frac{\partial f_1}{\partial x_1} & \cdots & \frac{\partial f_1}{\partial x_n} \\ \vdots & \ddots & \vdots \\ \frac{\partial f_n}{\partial x_1} & \cdots & \frac{\partial f_n}{\partial x_n} \end{bmatrix}}_{\text{Jacobian}} \underbrace{\begin{bmatrix} \Delta x_1 \\ \vdots \\ \Delta x_n \end{bmatrix}}_{\text{correction vector}} = \underbrace{\begin{bmatrix} -f_1 \\ \vdots \\ -f_n \end{bmatrix}}_{\text{residual vector}} \tag{A.6}$$

where the coefficient matrix on the left-hand side is the sensitivity matrix (also called the *Jacobian*). Eq. A.6 is solved for the correction vector, and the next better approximation is found as:

$$\mathbf{x}^{v+1} = \mathbf{x}^{v} + \mathbf{\Delta x}^{v} \tag{A.7}$$

The process of forming the sensitivity matrix and calculating the new values for $\mathbf{x}$ is repeated until a convergence criterion is achieved. The major drawback of the Newton's method is that sensitivity matrix must be evaluated at every iteration.

Convergence of the solution can be checked as either the correction vector or the residual vector approaches zero. If instability is observed, the correction factor can be *damped* by an arbitrary constant as:

$$\mathbf{x}^{v+1} = \mathbf{x}^{v} + \delta\mathbf{\Delta x}^{v} \tag{A.8}$$

where δ is the damping factor. A value of $\delta = 0.2$ is generally recommended.

APPENDIX B

PROPERTIES OF TACOT MATERIAL

The *TACOT* acronym stands for Theoretical Ablative Composite for Open Testing. Its material properties are similar to low density ablative materials. It is mainly used for code development and comparison of physical models. Material properties of the TACOT material are provided in [77]. Although properties of the pyrolysis gases in chemical equilibrium except thermal conductivity are also given in [77], properties calculated using *Cantera* are used in all simulations. Here, the following tables are given for the completeness of this document. The thermo-chemistry table, i.e. $B^{'}$ Table, for the TACOT material is excluded due to length.

Table B.1: Decomposition parameters

Component	$\rho_{v,i}, kg/m^3$	$\rho_{ch,i}, kg/m^3$	Z_i, s^{-1}	$\frac{E_{a,i}}{R_u}, K$	ψ_i	T_{reac}, K
A	300.0	0	1.20×10^4	8.556×10^3	3	333.3
B	900.0	600.0	4.48×10^9	2.044×10^4	3	555.6
C	1600.0	1600.0	0	0	0	5556.0

Table B.2: Heats of formation and initial resin volume fraction

Property	Value
Virgin heat of formation, h_v^o, J/kg	-8.571×10^5
Char heat of formation, h_{ch}^o, J/kg	0.0
Resin volume fraction, Γ	0.5

Table B.3: Pore structure parameters and emissivities

Property	Virgin	Char
Porosity, ϵ	0.8	0.85
Permeability, κ, m^2	1.60×10^{-11}	2.00×10^{-11}
Tortuosity	1.2	1.1
Emissivity, ε	0.8	0.9

Table B.4: Thermo-physical properties of virgin

T, K	$c_p, J/(kg \cdot K)$	$k, W/(m \cdot K)$	$h, J/kg$
2.556×10^2	8.792×10^2	3.975×10^{-1}	-8.967×10^5
2.980×10^2	9.839×10^2	4.025×10^{-1}	-8.571×10^5
4.444×10^2	1.298×10^3	4.162×10^{-1}	-6.901×10^5
5.556×10^2	1.465×10^3	4.530×10^{-1}	-5.365×10^5
6.444×10^2	1.570×10^3	4.698×10^{-1}	-4.016×10^5
8.333×10^2	1.717×10^3	4.860×10^{-1}	-9.124×10^4
1.111×10^3	1.863×10^3	5.234×10^{-1}	4.059×10^5
1.389×10^3	1.934×10^3	5.601×10^{-1}	9.334×10^5
1.667×10^3	1.980×10^3	6.978×10^{-1}	1.477×10^6
1.944×10^3	1.989×10^3	8.723×10^{-1}	2.028×10^6
2.222×10^3	2.001×10^3	11.09×10^{-1}	2.583×10^6
2.778×10^3	2.010×10^3	17.51×10^{-1}	3.697×10^6
3.333×10^3	2.010×10^3	27.79×10^{-1}	4.813×10^6

Table B.5: Thermo-physical properties of char

T, K	$c_p, J/(kg \cdot K)$	$k, W/(m \cdot K)$	$h, J/kg$
2.556×10^2	7.327×10^2	3.975×10^{-1}	-3.216×10^4
2.980×10^2	7.829×10^2	4.025×10^{-1}	0.0
4.444×10^2	1.093×10^3	4.162×10^{-1}	1.373×10^5
5.556×10^2	1.319×10^3	4.530×10^{-1}	2.713×10^5
6.444×10^2	1.432×10^3	4.698×10^{-1}	3.936×10^5
8.333×10^2	1.675×10^3	4.860×10^{-1}	6.870×10^5
1.111×10^3	1.842×10^3	5.234×10^{-1}	1.175×10^6
1.389×10^3	1.968×10^3	5.601×10^{-1}	1.705×10^6
1.667×10^3	2.052×10^3	6.050×10^{-1}	2.263×10^6
1.944×10^3	2.093×10^3	7.290×10^{-1}	2.839×10^6
2.222×10^3	2.110×10^3	9.221×10^{-1}	3.422×10^6
2.778×10^3	2.135×10^3	14.58×10^{-1}	4.602×10^6
3.333×10^3	2.152×10^3	23.18×10^{-1}	5.793×10^6

Table B.6: Properties of pyrolysis gases in chemical equilibrium at one atmosphere

T, K	$c_p, J/(kg \cdot K)$	$h, J/kg$	$MW, kg/kmol$	$\mu, Pa \cdot s$
2.00×10^2	1.512×10^3	-7.248×10^6	2.200×10^1	8.621×10^{-6}
3.00×10^2	1.631×10^3	-7.092×10^6	2.200×10^1	1.269×10^{-5}
4.00×10^2	1.847×10^3	-6.919×10^6	2.199×10^1	1.628×10^{-5}
5.00×10^2	2.241×10^3	-6.717×10^6	2.195×10^1	1.9541×10^{-5}
6.00×10^2	3.210×10^3	-6.452×10^6	2.171×10^1	2.261×10^{-5}
7.00×10^2	6.351×10^3	-6.005×10^6	2.088×10^1	2.559×10^{-5}
8.00×10^2	1.403×10^4	-5.010×10^6	1.863×10^1	2.864×10^{-5}
9.00×10^2	1.701×10^4	-3.327×10^6	1.544×10^1	3.176×10^{-5}
1.000×10^3	6.222×10^3	-2.167×10^6	1.394×10^1	3.443×10^{-5}
1.100×10^3	3.509×10^3	-1.740×10^6	1.376×10^1	3.669×10^{-5}
1.200×10^3	6.235×10^3	-1.326×10^6	1.365×10^1	3.884×10^{-5}
1.300×10^3	8.634×10^3	-5.759×10^5	1.318×10^1	4.092×10^{-5}
1.400×10^3	9.024×10^3	3.185×10^5	1.264×10^1	4.288×10^{-5}
1.500×10^3	1.082×10^4	1.363×10^6	1.212×10^1	4.469×10^{-5}
1.600×10^3	1.238×10^4	2.569×10^6	1.160×10^1	4.636×10^{-5}
1.700×10^3	7.338×10^3	3.514×10^6	1.126×10^1	4.803×10^{-5}
1.800×10^3	4.974×10^3	4.103×10^6	1.112×10^1	4.976×10^{-5}
1.900×10^3	4.281×10^3	4.555×10^6	1.106×10^1	5.150×10^{-5}
2.000×10^3	4.078×10^3	4.957×10^6	1.103×10^1	5.322×10^{-5}

Table B.7: Properties of frozen pyrolysis gases at one atmosphere ($MW = 17.89\ kg/kmol$)

T, K	$c_p, J/(kg \cdot K)$	$k, W/(m \cdot K)$	$h, J/kg$	$\mu, Pa \cdot s$
2.00×10^2	1.873×10^3	4.859×10^{-2}	-4.930×10^6	7.392×10^{-6}
3.00×10^2	2.111×10^3	7.150×10^{-2}	-4.730×10^6	1.086×10^{-5}
4.00×10^2	2.327×10^3	9.354×10^{-2}	-4.508×10^6	1.423×10^{-5}
5.00×10^2	2.516×10^3	1.150×10^{-1}	-4.266×10^6	1.745×10^{-5}
6.00×10^2	2.679×10^3	1.362×10^{-1}	-4.006×10^6	2.052×10^{-5}
7.00×10^2	2.821×10^3	1.572×10^{-1}	-3.731×10^6	2.345×10^{-5}
8.00×10^2	2.947×10^3	1.780×10^{-1}	-3.442×10^6	2.624×10^{-5}
9.00×10^2	3.060×10^3	1.987×10^{-1}	-3.142×10^6	2.892×10^{-5}
1.000×10^3	3.164×10^3	2.193×10^{-1}	-2.830×10^6	3.150×10^{-5}
1.100×10^3	3.259×10^3	2.397×10^{-1}	-2.509×10^6	3.398×10^{-5}
1.200×10^3	3.346×10^3	2.599×10^{-1}	-2.179×10^6	3.638×10^{-5}
1.300×10^3	3.426×10^3	2.800×10^{-1}	-1.840×10^6	3.870×10^{-5}
1.400×10^3	3.499×10^3	2.998×10^{-1}	-1.494×10^6	4.096×10^{-5}
1.500×10^3	3.566×10^4	3.195×10^{-1}	-1.141×10^6	4.314×10^{-5}
1.600×10^3	3.626×10^4	3.390×10^{-1}	-7.812×10^5	4.527×10^{-5}
1.700×10^3	3.682×10^3	3.584×10^{-1}	-4.157×10^5	4.734×10^{-5}
1.800×10^3	3.733×10^3	3.775×10^{-1}	-4.498×10^4	4.936×10^{-5}
1.900×10^3	3.779×10^3	3.870×10^{-1}	1.422×10^5	5.134×10^{-5}
2.000×10^3	3.822×10^3	4.153×10^{-1}	7.107×10^5	5.327×10^{-5}

APPENDIX C

GRID INDEPENDENCY OF SOLUTION VARIABLES

Results demonstrated in Chapter 5 are obtained using 100 elements with a cell growth rate of 1.02 and time step of $0.01\ s$. Here, it is intended to show that the presented results are independent of the cell size. Only the first simulation problem, i.e. *Case 1* in which surface is stationary, is considered, and pyrolysis gas mixture is assumed to be frozen.

Application of the Richardson Extrapolation method or Grid Convergence Index for the estimation of solution uncertainty is hindered by the fact that solution variables are a function of both time and space. Therefore, so as to ensure the grid independency of the solutions variables, results obtained using different grids are compared. Solutions are obtained on three different grid resolutions named as *finer*, *baseline*, and *coarser*. The *baseline* grid corresponds to the original grid that is used to obtain the simulation results. The *finer* and *coarser* grids are constructed from the original grid using a grid refinement factor of $r = 1.5$. Cell growth rate of each grid is determined such that the ratio of the size of the smallest cell to the largest cell remains almost the same. Table C.1 shows the grid parameters.

Table C.1: Grid parameters

Grid	Number of cells	Cell growth rate
finer	150	1.013
baseline	100	1.02
coarser	66	1.03

Figure C.1 - Figure C.4 compare the variation of solution variables obtained using different grids. As seen, qualitatively, it can be stated that all grids yield the same results as it is not feasible to distinguish each curve from the others. Quantitatively, the maximum difference between the temperature solutions is less than 0.5% whereas for most of the simulation time differences are less than 0.05%. For the volumetric heat transfer coefficient, the maximum difference between the *baseline* grid and *finer* grid is also less that 0.5% whereas for most of the simulation time differences are less than 0.1%. The difference between the *baseline* grid and *coarser* grid is around 2.5% at the depth of $z = 1\ mm$ between $t = 0.8\ s$ and $t = 1.2\ s$. Apart from that, differences are less than 0.5%.

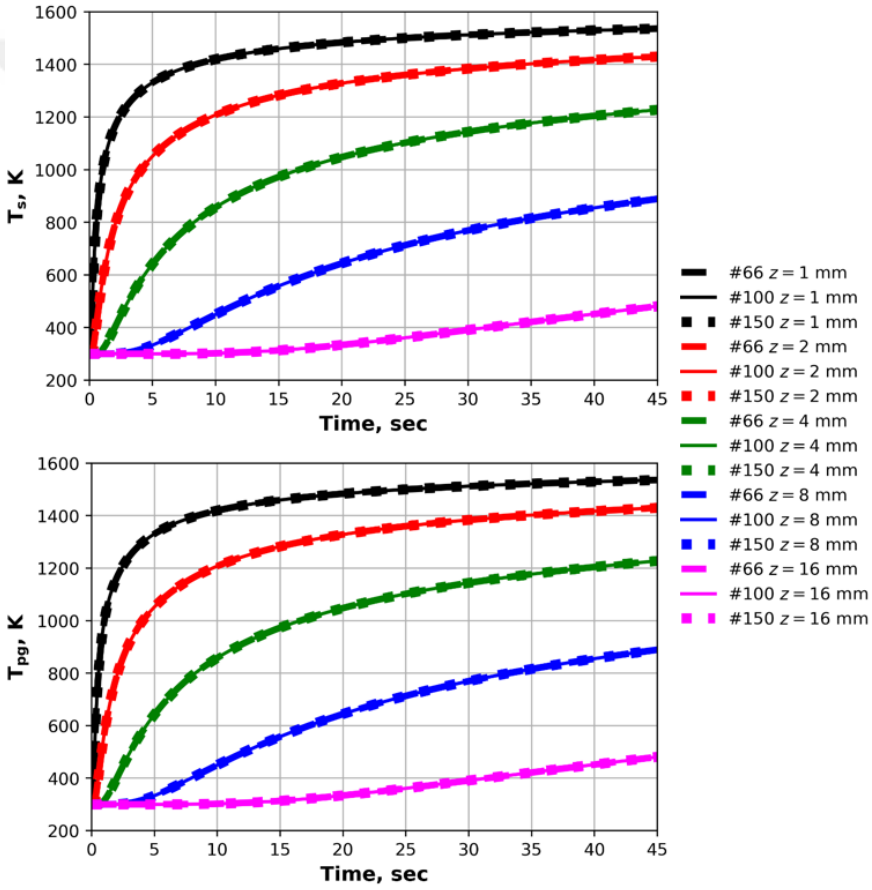


Figure C.1: Effects of cell size on solid and pyrolysis gas mixture temperatures

The maximum differences between the pyrolysis and char fronts are less than 0.5% whereas for most of the simulation time differences are less than 0.1%. However, for the pyrolysis gas blowing rate, the maximum difference between the *baseline* grid

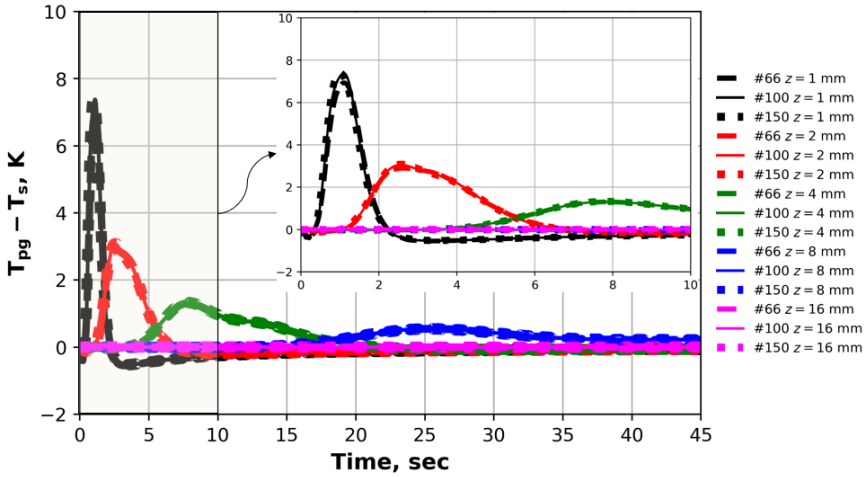


Figure C.2: Effects of cell size on temperature differences between the pyrolysis gas mixture and solid material

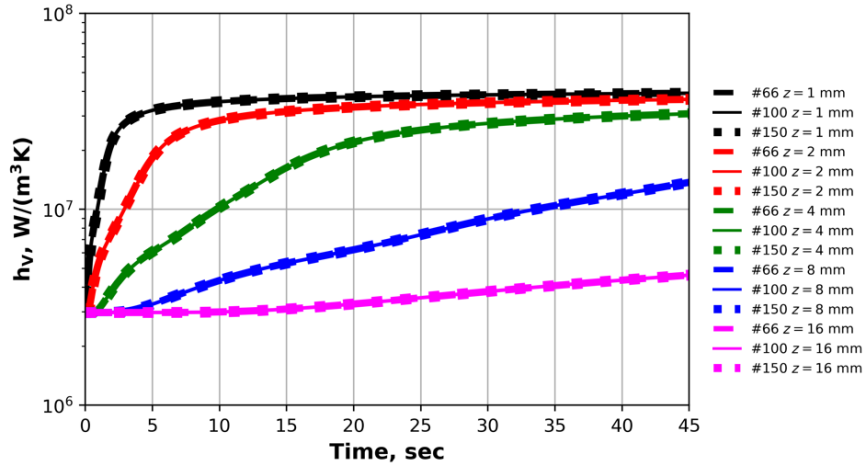


Figure C.3: Effects of cell size on volumetric heat transfer coefficient

and *finer* grid is around 26% whereas the maximum difference between the *baseline* grid and *coarser* grid is approximately 52%. In order to examine the nature of the differences, blowing rate results are re-plotted in the time range when the maximum differences take place and shown in Figure C.5. The *coarser* grid yields a damped oscillatory solution for the blowing rate between $t = 0.1$ and $t = 0.4$ s and this behavior produces large differences from the other solutions. The *baseline* and *finer* grids do not lead to oscillations in the blowing rates. Although the maximum difference between the *baseline* and *finer* grid solutions seems to be large, differences larger than 1% take place only at a few time points. For most of the simulation time differences

between the *baseline* and *finer* grid solutions are less than 0.1%.

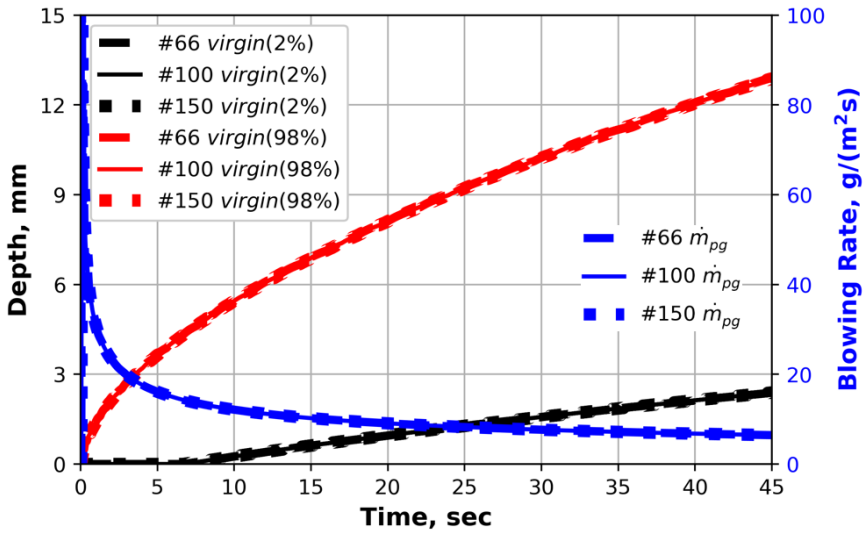


Figure C.4: Effects of cell size on evolution of pyrolysis and char fronts and pyrolysis gas blowing rates

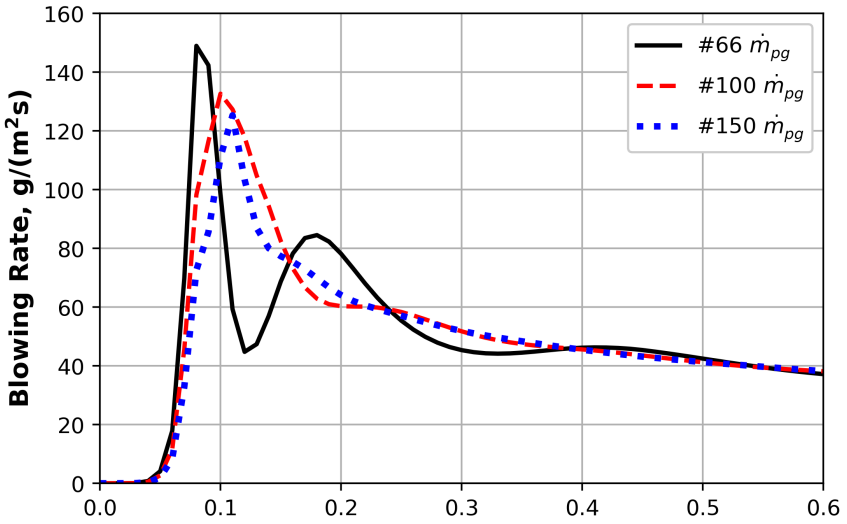


Figure C.5: Effects of cell size on abrupt change in pyrolysis gas blowing rates

CURRICULUM VITAE

PERSONAL INFORMATION

Surname, Name: Coşkun, Volkan
Nationality: Turkish (TC)
Date and Place of Birth:
Marital Status:
Phone:
email:

EDUCATION

Degree	Institution	Year of Graduation
M.S.	ETH Zurich Mechanical Engineering	2011
B.S.	ITU Mechanical Engineering	2008
High School	Ankara Atatürk Anatolian High School	2004

PROFESSIONAL EXPERIENCE

Year	Place	Enrollment
2013-Present	Roketsan Missiles Industries	Lead Engineer

FOREIGN LANGUAGES

Advanced English

PUBLICATIONS

Journal Publications

1. Ozaslan E., Yetgin A., Coskun V., Acar B. and Olgar T. "The Effects of Layer-by-Layer Thickness and Fiber Volume Fraction Variation on the Mechanical Performance of a Pressure Vessel ", Journal of Pressure Vessel Technology, 142(4): 041303 (2020)

2. Roesle M., Good P., Coskun V. and Steinfeld A. "Analysis of Conduction Heat Loss from a Parabolic Trough Solar Receiver with Active Vacuum by Direct Simulation Monte Carlo", Numerical Heat Transfer Applications, 62(5), 432-444 (2012)

3. Roesle M., Coskun V. and Steinfeld A. "Numerical Analysis of Heat Loss from a Parabolic Trough Absorber Tube with Active Vacuum System", Journal of Solar Energy Engineering, 133(3): 031015 (2011)

International Conference Publications

1. Coskun V., Sert C. and Acar B. "Development of a Material Response Solver for Charring Ablative Materials", 9th International Conference on Recent Advances in Space Technologies, 639-644 (2019)

2. Coskun V. and Ozkokdemir E. "Numerical Optimization of Thermo-chemical Curing Process of Epoxy Matrix Composites", Ankara International Aerospace Conference (2019)

3. Ozkokdemir E. and Coskun V. "Accuracy of Empirical Correlations for the Prediction of Aerodynamic Heating Rates at Supersonic Speeds", Ankara International Aerospace Conference (2019)

4. Ozaslan E., Yetgin A., Coskun V., Acar B. and Olgar T. "The Effects of Layer-by-Layer Thickness and Fiber Volume Fraction Variation on the Mechanical Performance of a Pressure Vessel ", ASME International Mechanical Engineering Congress and Exposition (IMECE2018), (2018)

5. Coskun V., Kutukceken E., Ozcatalbas M. and Acar B. "A Novel Methodology to Estimate Solid Propellant Temperature Before Ignition", 9th International Conference on Mechanical and Aerospace Engineering, 325-329 (2018)

6. Coskun V., Ozkokdemir E. and Acar B. "Modeling of Heat Transfer across Bolted Joints in Abaqus/CAE", SIMULIA Community Conference, 325-329 (2015)